Nanofluidics for Single Molecule DNA Sequencing

by

Padmini Krishnakumar

A Dissertation Presented in Partial Fulfillment
of the Requirements for the Degree
Doctor of Philosophy

Approved June 2013 by the
Graduate Supervisory Committee:

Stuart Lindsay, Chair
Sara Vaiana
Jin He
Kevin Schmidt

ARIZONA STATE UNIVERSITY

August 2013

ABSTRACT

After a decade of efforts, accurate and affordable DNA sequencing continues to remain an important goal in current research landscape. This thesis starts with a brief overview of the recent updates in the field of DNA sequencing technologies followed by description of the nanofluidics route to single molecule DNA detection. Chapter 2 presents discusses carbon nanotube(CNT) based nanofluidics. The fabrication and DNA sensing measurements of CNT forest membrane devices are presented. Chapter 3 gives the background for functionalization and recognition aspects of reader molecules. Chapter 4 marks the transition to solid state nanopore nanofluidics. The fabrication of Imidazole functionalized nanopores is discussed. The Single Molecule detection results of DNA from Palladium nanopore devices are presented next. Combining chemical recognition to nanopore technology, it has been possible to prolong the duration of single molecule events from the order of a few micro seconds to upto a few milliseconds. Overall, the work presented in this thesis promises longer single molecule detection time in a nanofludic set up and paves way for novel nanopore- tunnel junction devices that combine recognition chemistry, tunneling device and nanopore approach.

For my family and friends

ACKNOWLEDGMENTS

TABLE OF CONTENTS

iv

LIST OF TABLES

LIST OF FIGURES

1.   INTRODUCTION

1.1 INTODUCTION TO DNA SEQUENCING

Deoxyribonucleic acid (DNA) is a molecule that forms the basis for life on Earth. It contains the genetic blue print that is vital for the development and function of almost every living organism on earth, with the exception of some viruses that use RNA(ribonucleic acid) for their genome. In 1869, DNA was discovered, when Swiss medical researcher Friedrich Miescher isolated *nuclein*[1] (or what we know as nucleic acids today) for the first time in history.[2] Ever since then, numerous studies have revolved around this molecule and over the course of time, it has been experimentally established that genetic coding is universal – i.e. it is common to all living organisms. DNA sequencing thus, could be defined as the process that extracts the corresponding genetic information from DNA of the respective organism.

1.1.1 DNA Structure

The structure of DNA consists of phosphate backbone that forms the connecting link between chains of 2'-deoxy-D-ribose (5 member sugar rings) (see **Figure 1.1**). To each sugar ring is attached one of four heterocyclic nitrogen compounds (known as bases)- Adenine, guanine, thymine and cytosine. The first two bases belong to the family of substituted purines, while the other two are substituted pyrimidines. Adenine binds with thymine forming two hydrogen bonds while guanine binds to cytosine forming three hydrogen bonds. Due to this reliable Hydrogen bonding, two complimentary strands of single stranded DNA (ssDNA) when brought together attach well to form stable double stranded DNA helix.
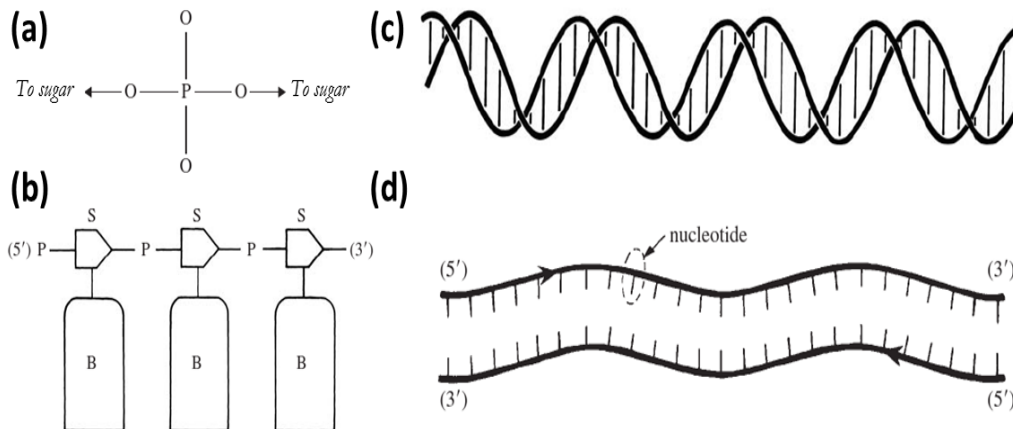
Figure 1.1 *Simple block schematic explaining the DNA structure. (a) The phosphate group linking sugars to form the sugar-phosphate backbone. (b) three nucleotides, with their sugar(S), phosphate(P) and base (B) components. (c) DNA double helix with each vertical line representing each base pair. The diameter of the double helix is 20Å. (d)Complementary strands when separated – showing a nucleotide. The width of each nucleotide is 6 Å.[3]*

The detailed chemical structures and bonding are shown in **Figure 1.2**. The Hydrogen bonding pairs are referred to as Watson Crick pairs, named after Watson and Crick who first suggested the double helix model for DNA in 1953.[4,5]

Figure 1.2a shows the carbons on the sugar ring labeled with a prime symbol, to distinguish them from the carbons in the bases. From the structure, it is evident that

single stranded DNA has two different ends, the 5' end and the 3' end. In double stranded

DNA, the complementary DNA strands are bound together with opposing ends. The

orientation of the strand plays an important factor in the processes that lead to protein

assembly, as DNA is only read from the 5' end to the 3' end.

  A base when attached to 2'-deoxy-D-ribose (the sugar ring in DNA) is referred to as a

nucleoside. The nucleosides are adenosine, guanosine, cytidine and thymidine

respectively. When a nucleoside is bound to a phosphoric acid, either at the 5' or 3'

position, it is called a nucleotide.
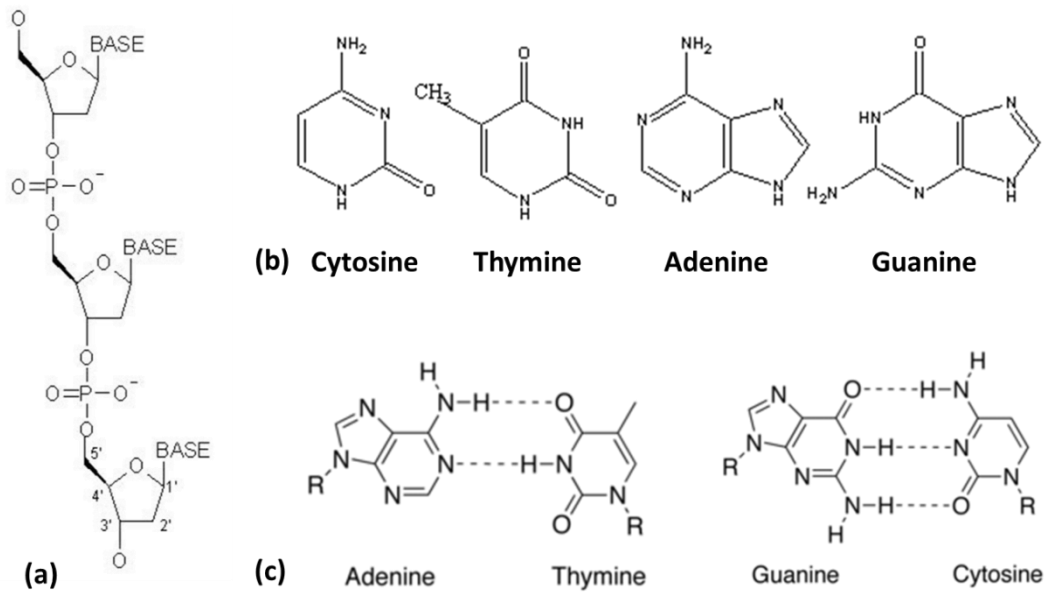
Figure 1.2 *Chemical bonding in DNA. (a) Molecular orientation of ssDNA strand. (b)*

Individual Bases of DNA (c) Hydrogen bonding between base pairs.[6]

Depending on the position of the phosphate group (5' or 3'), the form of phosphate (mono, di or tri-phosphate) and type of nucleoside, the nucleotide is named accordingly. For instance, adenosine bonded at the 5' position to a triphosphate is referred to as adenosine 5'-triphosphate (ATP). ATP plays key role as energy carrier for cellular processes.

1.1.2 Significance of DNA Sequencing

In the cell, DNA codes the information for proteins. Just as the four bases form the alphabets for language of nucleic acids, 20 amino acids form the alphabets for the language of proteins. DNA is translated into another biopolymer called ribonucleic acid (RNA). For translation to occur, the double strand of DNA has to be unwound. Once the DNA has been unwound, one of the strands, referred to as the template or antisense-strand, is read from the 3' end and complementary bases of RNA bind to the DNA and are linked together. The resulting strand of RNA contains the exact same information as is contained in the DNA since the strand is complementary. This RNA strand is then able to move outside of the cell nucleus and play one of several vital roles in protein synthesis. Proteins serve many vital functions in living systems, and thus, the DNA that codes for them is an important part of the cell. They are involved in virtually all cell functions. Each protein within the body has a specific function. Some proteins are involved in structural support, while others are involved in bodily movement, or in defense against germs. Furthermore, protein generation and regulation is necessary for maintaining

optimal health. For this reason, sequencing of DNA has, and continues, to play an important role in biological sciences.

Clinically, there are thousands of rare genetic diseases, ranging from the widely-known (such as *Huntington's disease*, an adult-onset brain disorder) to the obscure (such as *fibrodysplacia ossificans progressiva* , where the patient's muscles slowly get replaced by bones). While each of these diseases may be rare, collectively they cause a lot of suffering. Single-gene disorders affect four out of every thousand live births and account for more than 10% of paediatric hospital admissions.[7] Genome sequencing, especially when coupled with the need to unravel mutations for rare genetic diseases, assumes a goal far more significant than just academic interest. Thus the ability to sequence the human genome at a fraction of the current cost and time could potentially lead to detection and prevention of future diseases as well as improve the implementation of individualized medical treatment.

1.2   PROGRESS IN SEQUENCING TECHNOLOGIES

The first leap of advance in sequencing occurred in 1975 when Sanger and Coulson discovered the chain termination method.[8] This marked the beginning of First – generation sequencing. Other technologies included in this time period are chemical method proposed by Maxam and Gilbert in 1976-77. [9]

The Sanger technique achieved sequencing of the first genome, bacteriophage ΦX 174, which is 5375 bases in length. Decades later, four-color fluorescent[10] Sanger sequencing (each color corresponds to each base) was still a part of the first human genome sequence effort– a project that involved great cost and decade long human effort. Sanger method

was, and continues to be in use in some form. Hence, sequencing history without a brief description of this method would be incomplete.

1.2.1   Sanger Method

First, a reaction mix is prepared by putting together template DNA, free nucleotides, an enzyme and a DNA 'primer' – a small piece of single stranded DNA which is about 20-30 nucleotides long and can hybridize to one strand of the template DNA. The enzyme is usually a variant of Taq polymerse. The free nucleotides are labeled either radioactively or by attaching fluorescent tags.

First, the double stranded DNA is heated so as to break the Hydrogen bonds that bind the strands together, and this causes them to separate into single strands. The primer attaches to the strand at some spot after which the polymerase begins to elongate the primer. This process, if allowed to go complete will result in a DNA strand that's identical to the template DNA we began with. So, if we begin with hundred strands of template DNA, on completion, we would have hundred new copies of one of the strands of the template.

 In the reaction mixture are also present a small amount of chain terminators or Dideoxynucleotides. These nucleotides are very similar to regular DNA nucleotides except that on their sugar ring, the third Carbon from base has just Hydrogen instead of the usual Hydroxyl (-OH) group. So, if instead of a regular nucleotide, a Dideoxynucleotide happens to attach to the growing primer strand, then, nucleotides cannot be added after it as there is no -OH group for bonding. Thus adding a Dideoxynucleotide leads to chain termination.

6

(a)

5' 3' 5' 3' 5' 5' 3' 5' 3' 5' 5'
3' 5' 3' 5' 3' 5' 3' 5' 3'

(b)

Normal Nucleotides

Didoxy Chain Terminators

(c)

DNA Polymerase reads the template strand and synthesizes a new second strand to match

5' – TACGCGGTAACGGTATGTTCGACCGTTTAGCTACCGAT
3' – ATGCGCCATTGCCATACAAGCTGGCAAATCGATGGCTAGAGATCCAA – 5'

If 5% of the T nucleotides are actually dideoxy T, then each strand will terminate when it gets a ddT at its end.

5' – TACGCGGTAACGGTATGTTCGACCGTTTAGCTACCGAT•
5' – TACGCGGTAACGGTATGTTCGACCGTTTAGCT•
5' – TACGCGGTAACGGTATGTTCGACCGTTT•
5' – TACGCGGTAACGGTATGTTCGACCGTT•
5' – TACGCGGTAACGGTATGTTCGACCGT•
5' – TACGCGGTAACGGTATGTT•
5' – TACGCGGTAACGGTATGT•
5' – TACGCGGTAACGGTAT•
5' – TACGCGGTAACGGT•
5' – TACGCGGT•

(d)

Gel:

G GCGAATGCGTCCACAACGCTACAGGTG
T GCGAATGCGTCCACAACGCTACAGGT
G GCGAATGCGTCCACAACGCTACAGG
G GCGAATGCGTCCACAACGCTACAG
A GCGAATGCGTCCACAACGCTACA
C GCGAATGCGTCCACAACGCTAC
A GCGAATGCGTCCACAACGCTA
T GCGAATGCGTCCACAACGCT
C GCGAATGCGTCCACAACGC
G GCGAATGCGTCCACAACG
C GCGAATGCGTCCACAAC
A GCGAATGCGTCCACAA
A GCGAATGCGTCCACA
C GCGAATGCGTCCAC
A GCGAATGCGTCCA
C GCGAATGCGTCC
C GCGAATGCGTC
T GCGAATGCGT
G GCGAATGCG
C GCGAATGC
G GCGAATG
T GCGAAT

Figure 1.3 *(a) The first step shows the separation of double stranded DNA into single strands. The second step shows the attaching of primer to the template and the elongation of template in the presence of DNA polymerase. (b) The Dideoxynucleotide has a Hydrogen instead of a Hydroxyl group on the third Carbon atom in the sugar ring. This causes it to be a chain terminator. (c) Replication performed in the presence of Dideoxy-T (d) Electrophoresis on gel – showing an illustration of the colored bands representing the positions of the four bases.*

For the case of replication in the presence of chain terminator, the amount of Dideoxynucleotide is controlled to 5% of the total amount of the regular nucleotides. Thus, every time a nucleotide is required to build the primer, the polymerase will ensure to procure a 'good' regular nucleotide, where as there is a meager 5% chance that this might happen to be a Dideoxynucleotide. Thus, sooner or later, all the strands get terminated, although, they would have got terminated at different lengths. If there were a large number of template strands to begin with, it would result in primers terminated at all possible lengths.

So, if we used dideoxy -T as the chain terminator, it would mean that every strand would have ended with a T base. So, now, although, the products of our reaction happen to be strands of different lengths, they all end in T. In other words, if we only know the length of each of these strands, we have the knowledge of all the positions where T occurs on the Template strand. Further, if four sets of the same template strands undergo the same reaction-except with 4 different chain terminators, i.e. dideoxy-A, dideoxy-T, dideoxy-C and dideoxy-G, and analyse the lengths of the resulting strands in each case, we will, ineffect, know the all the positions of occuence of A, T, C and G respectively. Thus, the DNA sequence can be known.

In order to find the lengths of the resulting strands, the Dideoxynucleotides are chemically modified to fluoresce under exposure to ultraviolet radiation. And each of them fluoresce at different wavelengths unique to their chemical structure. Thus, the reaction products are separated lengthwise under a resolution of one base, by gel electrophoresis on a denaturing polyacrylamide-urea gel. Each of the four chain

termination reactions is run on 4 different lanes of the gel, and the gel is then visualized in UV light. The result is seen as bands of four colors occurring at different distances.

In an industrial, high-throughput configuration, Sanger technology was used in the sequencing of the first human genome, which was completed in 2003 through the Human Genome Project, a 13-year effort with an estimated cost of $2.7 billion.[11] There are however, limitations to Sanger-sequencing have stimulated the development of new techniques. Most importantly, the expense involved in Sanger sequence prohibits its use in view of future goals that include sequencing thousands of human genomes.[12]

1.2.2   Next (Second) Generation Sequencing

The successful completion of first generation sequencing demonstrated the feasibility of the technical sequencing part of the Human Genome project, and triggered the development of a series of techniques that could allow higher sequencing throughput. Five years later, in 2008, a human genome was sequenced over a 5 month period for approximately $1.5 million.[11]
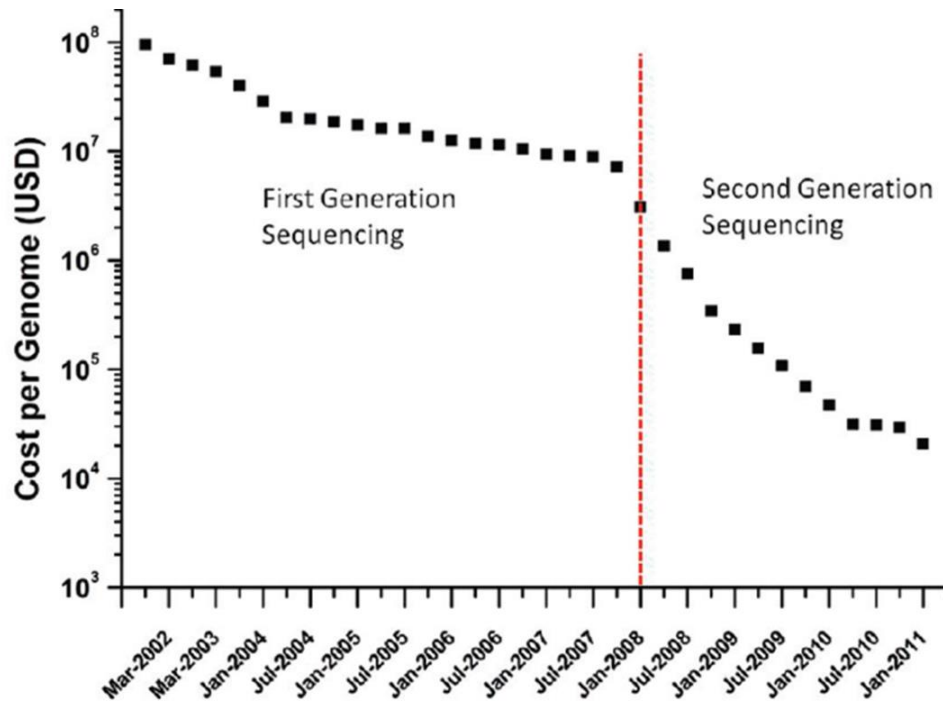
Figure 1.4 *Graph from Review by Niedringhaus et al shows the estimated cost required to sequence a complete human genome based on expense data from NHGRI-funded-large-scale DNA sequencing centers.* [13]

This accomplishment was directly the result of the rapidly evolving Next Generation Sequencing (NGS) technologies such as pyrosequencing and sequencing by litigation chemistry.[13] Commercially available NGS platforms include Roche's 454 Genome Sequencer FLX, [14] Illumina's Genome Analyzer,[15–17] helicos Heliscope[18] and Life Technologies SOLiD system. A detailed review including the comparison, advantages and shortcomings of the various NGS platforms is provided in review by Voelkerding et al.

Although, with the advent of NGS, the sequencing cost per base has gone down several orders of magnitude when compared to the cost involved in Sanger sequencing, yet the

10

main limiting factor for these emerging technologies remains the over-all high cost of generating sequence with high throughput. Also, when compared to Sanger sequencing, it must be admitted that the several of the newer technologies are challenged by higher error factors, non-uniform confidence in base calling, short read lengths etc. [19]

The second generation sequencing technologies are progressing to achieve even better throughput at reduced cost via constant innovation in their chemical, engineering and informatics aspects. The momentum of progress is such that by the time some of the techniques are translated to instruments for general access, there are further innovations that outdate the very technique to begin with.

Also, some of the advances are made on such rapid time scales that they do not easily fit into a generational time bracket – The effect of this being a difficulty in categorizing certain techniques in second or third generation sequencing.

Despite this technological gusto, there is still an underlying need for the revolutionary advances that will ultimately land the sequencing tool into the physician's office as a cost-effective component of standard medical care.

1.2.3   Third Generation Sequencing

Thus with the vision of bringing the cost of a human genome to under $1000, National Institutes of Health/ National Human Genome Research Institute (NIH/NHGRI) funded various groups to improve the existing techniques as well as develop alternative approaches to sequencing. In most of the major SGS sequencing, the process flow depends on Polymerase Chain Rection (PCR) to amplify a DNA template so that resulting DNA cluster can be tethered to a solid substrate and imaged as the clusters get

sequenced. The new generation of Sequencing by synthesis (SBS) technologies

interrogate single molecules of DNA, such that no synchronization is required (a

limitation of SGS), thereby overcoming issues related to the biases introduced by PCR

amplification and dephasing. More importantly, this new generation of sequencing

technologies has the potential to exploit more fully the high catalytic rates and high

processivity of DNA polymerase. There is scope to avoid any biology or chemistry

altogether. There is also a possibility of increasing the read length radically (from tens of

bases to tens of thousands of bases per read) and shorter time to acquire results (from

days to hours or minutes). The promises then of this new, third generation of sequencing

technologies in offering advantages over current sequencing technologies are (i) higher

throughput; (ii) faster turnaround time (e.g. sequencing metazoan genomes at high fold

coverage in minutes); (iii) longer read lengths to enhance *de novo* assembly and enable

direct detection of haplotypes and even whole chromosome phasing; (iv) higher

consensus accuracy to enable rare variant detection; (v) small amounts of starting

material (theoretically only a single molecule may be required for sequencing); and (vi)

low cost, where sequencing the human genome at high fold coverage for less than $100.[20]

SBS technologies can roughly be binned into three different categories: (i) SBS

technologies in which single molecules of DNA polymerase are observed as they

synthesize a single molecule of DNA; (ii) Nanofluidic based nanopore-sequencing

technologies in which single molecules of DNA are threaded through a nanopore or

positioned in the vicinity of a nanopore, and individual bases are detected as they pass

through the nanopore; and (iii) direct imaging of individual DNA molecules using

advanced microscopy techniques. Each of these technologies provides novel approaches

to sequencing DNA and has advantages and disadvantages with respect to specific applications.

These technologies are at varying stages of development, making the writing of a review on Third generation Sequencing (TGS) difficult given there is still much to prove regarding the utility of many of the TGS technologies. However, if the full potential of these technologies is realized, in a span of several years, whole genome sequencing will likely be fast enough and inexpensive enough to re-sequence genomes as needed for any application. Thus the emerging TGS technologies have the potential to make such stunning advances possible. [20] Here we discuss nanofluidics subset of this technology, which is relevant to the work presented in the later chapters of this dissertation.

1.3   NANOFLUIDICS AS A ROUTE TO DNA SEQUENCING

Most nanopore sequencing technologies rely on transit of a DNA molecule or its component bases through a hole and detecting the bases by their effect on an electric current or optical signal. Because this type of technology uses single molecules of unmodified DNA, they have the potential to work quickly on extremely small amounts of input material. Both biological nanopores constructed from engineered proteins and entirely synthetic nanopores are under development. In particular, there is potential to use atomically thin sheets of grapheme as a matrix supporting nanopores and also carbon nanotubes for these applications.

1.3.1 Introduction to Nanopores

A nanopore is a nanometer sized aperture present in a membrane that separates two chambers filled with conductive electrolyte. When an electric potential is applied across

the nanopore, by means of electrodes immersed in the chambers, ionic flow through the nanopore results in the creation of ionic current. When an analyte molecule of interest is introduced into the input chamber; driven by the applied potential, the molecule flows towards the output chamber via the nanopore. While passing through the aperture, the temporary partial blockade of the aperture results in a transient decrease in the ionic current. The electric signal in turn reveals useful information about the analyte particle. This is the essence of the nanopore–scheme of single molecule detection. The underlying principle of such orifice-based resistive-sensing of particles in solutions was pioneered by Wallace H. Coulter in 1953.[21] The Coulter counter applies the principle at the micrometer scale to count and size blood cells. Invented 6 decades ago, it has evolved into an accurate, effective and ubiquitous hematological tool in clinical labs today. Nanopores are sort of miniaturized coulter-counters in that they analyze biomolecules (of cross-sectional diameter of a few nm) using the same principle at the nanometer scale. The use of nanopores as tools for molecular analysis constitutes a much younger branch of biophysics that began in the early 90s. Prior to the emergence of the first nanopore studies, ion channels found in lipid bilayers and membranes were already being investigated as part of electrophysiological studies.[22,23]

1.3.2 Biological and Synthetic Nanopores

The first nanopores were biological – they were based on trans-membrane protein α-hemolysin.[24,25] By demonstrating the electrical detection of individual ssDNA and ssRNA molecules using α-hemolysin these studies marked the milestone that initiated a plethora of efforts in biological pore based single molecule work. DNA translocation

dynamics[26] in these pores have been examined in context of molecular orientation[27], polymer length, applied electric potential[28,29], temperature[30] and direction of approach with respect to the nanopore.

Homopolymer and Hairpin DNA translocation studies show that it is possible to tap single base resolution and sequence-specific information using α-hemolysin pores.[31] In perspective of nucleic acid analysis, a majority of the nanopore based experimental findings come from α-hemolysin based studies. However, biological pores also have limitations in terms of size, stability, resolution and variability.[32] In response to these limitations, biological pores are increasingly being combined with enzyme motors and this route has recently demonstrated proof-of-principle DNA sequencing.[33,34] Based on single-molecule mass spectroscopy,[35,36] proof-of-principle DNA sequencing-by-synthesis in biological nanopores has also been demonstrated.[37]

With the advances in modern microfabrication facilities, a different class of nanopores known as synthetic nanopores have become increasingly popular.[38] Made of solid-state materials, these pores exhibit superior stability over their biological counterparts. The conventional semiconductor processes involved in fabrication of solid-state nanopores provide scope for tunability in size, mass fabrication and seamless device integration. In 2003, Li et al demonstrated dsDNA translocation in solid state nanopore for the first time.[39]

Controlling the DNA translocation speed was soon identified as the key step toward single molecule identification. By changing bias and electrolyte properties Li et al

achieved 30 base/µs translocation speed for 3 kilo base pair (kbp) dsDNA in silicon nitride pores.[40] Chen et al achieved similar translocation speeds(~ 27 base/µs) by fine-tuning surface properties of the solid-state nanopores via atomic layer deposition of alumina.[41,42] Despite these advances, the translocations in solid state nanopores occur too fast compared to the speeds desirable for sequencing, and the need for improving temporal resolution in solid state nanopore continues to exist.[43–46]

Attempts to control biomolecular transport in solid state nanopores include altering the electrolyte viscosity,[40] temperature, electro-osmotic screening, [47,48] alternating electric field,[49] optical[50] and magnetic tweezers[51]. Theoretical investigations suggest that reducing the fluid temperature from ambient conditions to 0℃ could cut translocation speed by 49.7%.[52] The effect of counter ion binding has been applied to reduce the charge on DNA and thus prolong its translocation time.[53] In this study Kowalczyk et al report a 10 fold increase in ssDNA translocation by changing the electrolyte from KCl to LiCl. Biological modification of pores include targeted scaffolding of solid state nanopores with DNA origami[54] and enzymes such as phi29 DNA polymerase.[34,55] Keyser and others have shown that the entire surface of a nanopore can be functionalized to slow DNA.[56] Other pore modifications involve manipulating the charge distribution on the walls of nanopore, via gate modulation[57] and electrostatic screening.[58]
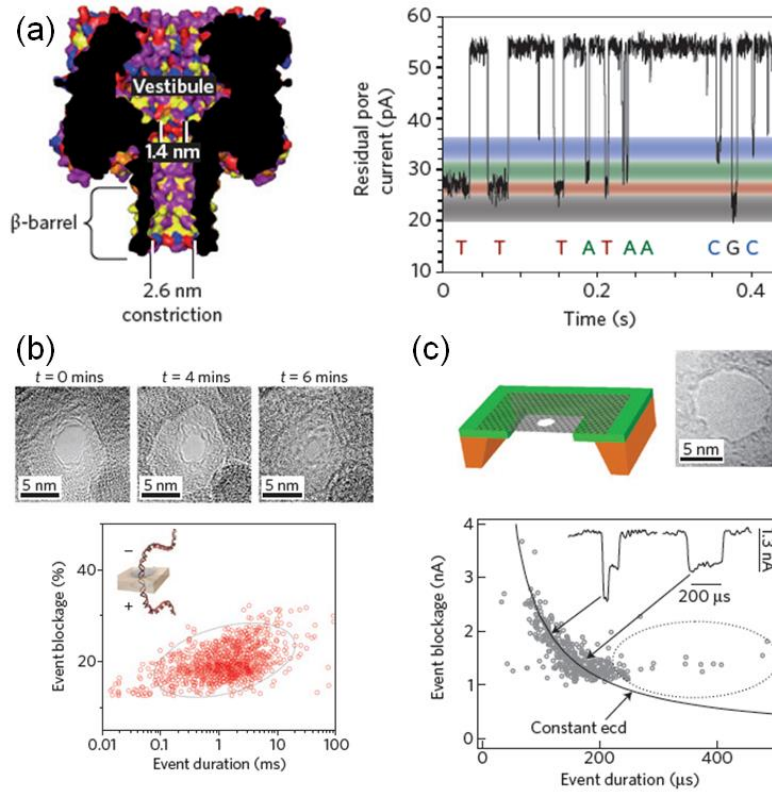
Figure 1.5 *Protein nanopores and solid state nanopores for DNA analysis.[59] (a) Left: structural cross-section of α-haemolysin. Right: typical plot of residual ionic current through an aminocyclodextrin-modified α-haemolysin nanopore versus t for individual mononucleotides (dAMP, dCMP, dGMP, dTMP).[60](b) Top: TEM images of nanopores in Al_2O_3 membranes. Bottom: scatter plot of event blockage (the percentage of open pore ionic current that is blocked as a molecule passes through the pore) vs. event duration for the translocation 5kbp dsDNA through a 5-nm Al_2O_3 pore showing a single blockage level corresponding to linear, unfolded dsDNA transport. (c) Top: schematic (left) and TEM image (right) of a nanopore in a suspended graphene film. Bottom: scatter plot of event blockage versus event duration showing that folded DNA (left of inset, deep blockade level) and unfolded DNA (right of inset, shallow blockade level) can be distinguished. The solid line represents a constant electronic charge deficit.*

17

1.3.3. Carbon Nanotubes

Carbon nanotubes (CNTs) have recently emerged as a new type of synthetic nanopore. CNTs are grown or formed from bottom- up rather than top- down approach. Hence the absence of the need to manipulate or control at the nanoscale fabrication is advantageous. Also, with hydrophobic walls and nanochannel structure, CNTs can be treated as synthetic analogs of biological ion channels, and explored in order to understand flow at nanometer scale. The interior surface of good quality CNTs is pristine with well-defined structure providing for an atomically smooth, frictionless pathway of transport. The excellent electrical properties of CNTs provide new routes to electrical detection, trapping and manipulation of charged biomolecules and nanoparticles. Well-defined sites are available for chemical functionalization at the ends of the tubes. Such modifications will be extremely useful for ion and molecule selection, gating or separation. Smooth surface and perfect uniformity over large distances also.

 Molecular dynamics (MD) simulations by Hummer et al led to observations of spontaneous wetting and filling of water molecules.[61] Despite the hydrophobicity of the walls, the nanoscale confinement and the interactions between water and the CNT surface caused alignment of water molecules inside the CNT. This increased the stability of the CNT confined molecules .The lower free energy of confined water predicted ready wetting of CNTs and the frictionless walls meant very fast water transport through CNTs. Following the pioneering work on water molecule transport, the translocations of more complicated molecules, such as long chain polymer molecules,[62] DNA[63] and RNA,[64] were simulated as well. Van der Waals and hydrophobic interaction forces

assisted in translocation of these molecules when driven by an electric field. In support

of these facts, in-situ experimental studies of wetted CNTs using nuclear magnetic

resonance (NMR), [65]IR spectroscopy,[66] transmission electron microscope (TEM)[67]

and scanning electron microscope (SEM)[68] confirmed the presence of water molecules

aided by ordered structuring within CNT .

In 2010, Liu et al reported experimental verification of translocations of DNA in

nanotube system for the first time.[69] ssDNA (60-nt and 120-nt) with sequences that were

predicted to be relatively free of secondary structure were translocated through a single

walled carbon nanotube (SWCNT) based device. When DNA molecules were introduced

to the input reservoir of the device, large transient increases in current were observed.

These "spikes" were accompanied by large fluctuations in the background current

(**Figure 4.6**). The spikes disappeared when the polarity of the bias across the tube was

reversed and reappeared when the original bias (positive on the output side) was restored.
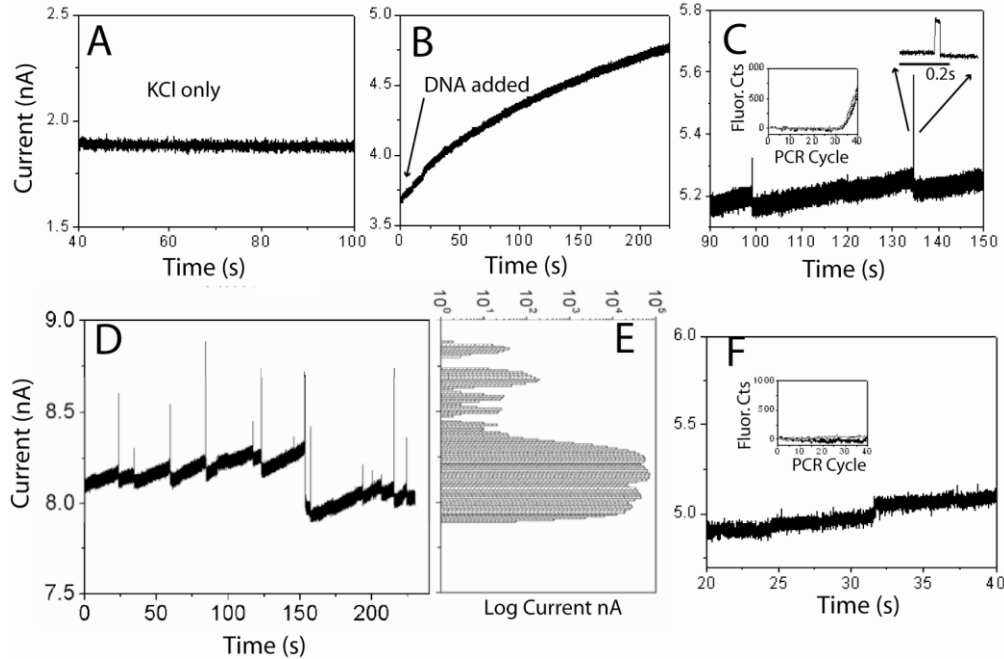
Figure 1.6 *Ion current signals of DNA translocation.[65] (A) Current (2 M KCl, 1 mM PBS, pH 7) before DNA addition. (B) After DNA addition, current slowly increases. (C) 5 min after addition of 0.1nM 60-nt DNA, large positive current spikes appear. These spikes are followed by a drop in baseline over a periodof a second or so and then by a gradual rise leading to the next spike. (D) Representative data from another tube (also 60-nt DNA), with the distribution of currents shown in (E). The DNA causes large changes in baseline in addition to the spikes. (F) Data from a tube that showed both a current increase on DNA addition and baseline fluctuations but no spikes. No translocation was detected by PCR. The insets in (C) and (F) show the fluorescence signal from double-stranded DNA dye labels as a function of the PCR cycle number for samples collected from these particular runs.*

Quantitative polymerase chain reaction (QPCR), for detecting and counting small numbers of molecules, showed that DNA was translocated in devices manifesting these large spikes. Thus, the spikes signal translocation of DNA through the SWCNTs.

1.4   THESIS SUMMARY

Having introduced the field of DNA sequencing, examined the background of nanofluidics in third generation sequencing (single molecule DNA sequencing) , we now move onto examine the nanofluidic systems of this study. Chapter 2 presents the work related to CNT membrane devices. Fabrication, characterization and experimental results from these devices are discussed. A section of this chapter also covers the synthesis of graphene which has been subsequently used for graphene based translocation devices. Chapter 3 discusses the background of functionalization of metal electrodes within the context of recognition tunneling. A good understanding of role of reader molecules in STM experiments is necessary and the evolution of these molecules in pace with demands of DNA sequencing goals, sets the stage for Chapter4.

Chapter 4 is sort of a confluence of chapters 2 and 3.On one hand, there are the inherent disadvantages common to any CNT based device (such as the lack of control of chirality and uniformity). On the other hand, even a setup (like the functionalized STM experiment) that has repeatedly and successfully demonstrated great molecular sensitivity and base differentiating capabilities ultimately requires a more dedicated method of orienting DNA molecules to the tunnel junction, if long DNA molecules are to be sequenced. These disadvantages motivate the switch over to solid state technology. Silicon Nitride nanopores are the object of interest in Chapter 4. When coated with Pd

and functionalized, these nanopores form a nanochannel with reader molecule sensitivity. Voltage driven ionic flow and biomolecular transport of DNA through these pores give some interesting results that promise a way to control translocations in nanopore systems. Finally, chapter 5 summarizes all the experimental results in perspective of the grand goals of DNA sequencing. The significance of the progress thus far as well as the plan for future work is described briefly

1.5 REFERENCES

1.   Dahm, R. Friedrich Miescher and the discovery of DNA. *Developmental Biology* **278,** 274–288 (2005).

2.   Maderspacher, F. Rags before the riches: Friedrich Miescher and the discovery of DNA. *Curr. Biol.* **14,** R608 (2004).

3.   Mulhardt, C. *Molecular Biology and Genomics*. (Academic Press, 2006).

4.   Watson, J. D. & Crick, F. H. C. Molecular Structure of Nucleic Acids: A Structure for Deoxyribose Nucleic Acid. *Nature* **171,** 737–738 (1953).

5.   Watson, J. D. & Crick, F. H. C. Genetical Implications of the Structure of Deoxyribonucleic Acid. *Nature* **171,** 964–967 (1953).

6.   Base pair. *Wikipedia, the free encyclopedia* (2013). at <http://en.wikipedia.org/w/index.php?title=Base_pair&oldid=555542584>

7.   How new DNA sequencing technologies are unravelling rare genetic diseases. *Wellcome Trust Blog* at <http://blog.wellcome.ac.uk/2011/04/13/how-new-dna-sequencing-technologies-are-unravelling-rare-genetic-diseases/>

8.   Sanger, F., Nicklen, S. & Coulson, A. R. DNA sequencing with chain-terminating inhibitors. *PNAS* **74,** 5463–5467 (1977).

9.   Maxam, A. M. & Gilbert, W. A new method for sequencing DNA. *PNAS* **74,** 560–564 (1977).

10.   Ju, J. *et al.* Four-color DNA sequencing by synthesis using cleavable fluorescent nucleotide reversible terminators. *PNAS* **103,** 19635–19640 (2006).

11.   Voelkerding, K. V., Dames, S. A. & Durtschi, J. D. Next-Generation Sequencing: From Basic Research to Diagnostics. *Clinical Chemistry* **55,** 641–658 (2009).

12.   Strausberg, R. L., Levy, S. & Rogers, Y.-H. Emerging DNA sequencing technologies for human genomic medicine. *Drug Discovery Today* **13,** 569–577 (2008).

13.   Niedringhaus, T. P., Milanova, D., Kerby, M. B., Snyder, M. P. & Barron, A. E. Landscape of Next-Generation Sequencing Technologies. *Anal Chem* **83,** 4327–4341 (2011).

14.   Wheeler, D. A. *et al.* The complete genome of an individual by massively parallel DNA sequencing. *Nature* **452,** 872–876 (2008).

15.   Bentley, D. R. *et al.* Accurate whole human genome sequencing using reversible terminator chemistry. *Nature* **456,** 53–59 (2008).

16.   Ley, T. J. *et al.* DNA sequencing of a cytogenetically normal acute myeloid leukaemia genome. *Nature* **456,** 66–72 (2008).

17.   Wang, J. *et al.* The diploid genome sequence of an Asian individual. *Nature* **456,** 60–65 (2008).

18.   Pushkarev, D., Neff, N. F. & Quake, S. R. Single-molecule sequencing of an individual human genome. *Nat Biotech* **27,** 847–850 (2009).

19.   Ansorge, W. J. Next-generation DNA sequencing techniques. *New Biotechnology* **25,** 195–203 (2009).

20.   Schadt, E. E., Turner, S. & Kasarskis, A. A window into third-generation sequencing. *Hum. Mol. Genet.* **19,** R227–R240 (2010).

21.   Coulter, W.H. Means for Counting Particles suspended in a fluid. US 2656508A
22.   Hille, B. Ionic channels in excitable membranes. Current problems and biophysical approaches. *Biophys J* **22,** 283–294 (1978).

23.   Sakmann, B. & Neher, E. Patch Clamp Techniques for Studying Ionic Channels in Excitable Membranes. *Annual Review of Physiology* **46,** 455–472 (1984).

24.   Kasianowicz, J. J., Brandin, E., Branton, D. & Deamer, D. W. Characterization of individual polynucleotide molecules using a membrane channel. *PNAS* **93,** 13770–13773 (1996).

25.   Akeson, M., Branton, D., Kasianowicz, J. J., Brandin, E. & Deamer, D. W. Microsecond Time-Scale Discrimination Among Polycytidylic Acid, Polyadenylic

Acid, and Polyuridylic Acid as Homopolymers or as Segments Within Single RNA Molecules. *Biophysical Journal* **77,** 3227–3233 (1999).

26.   Meller, A. Dynamics of polynucleotide transport through nanometre-scale pores. *J. Phys.: Condens. Matter* **15,** R581 (2003).

27.   Wanunu, M., Chakrabarti, B., Mathé, J., Nelson, D. R. & Meller, A. Orientation-dependent interactions of DNA with an α-hemolysin channel. *Phys. Rev. E* **77,** 031904 (2008).

28.   Meller, A. & Branton, D. Single molecule measurements of DNA transport through a nanopore. *Electrophoresis* **23,** 2583–2591 (2002).

29.   Meller, A., Nivon, L. & Branton, D. Voltage-Driven DNA Translocations through a Nanopore. *Phys. Rev. Lett.* **86,** 3435–3438 (2001).

30.   Meller, A., Nivon, L., Brandin, E., Golovchenko, J. & Branton, D. Rapid nanopore discrimination between single polynucleotide molecules. *PNAS* **97,** 1079–1084 (2000).

31.   Vercoutere, W. *et al.* Rapid discrimination among individual DNA hairpin molecules at single-nucleotide resolution using an ion channel. *Nat Biotech* **19,** 248–252 (2001)
.
32.   Deamer, D. W. & Branton, D. Characterization of Nucleic Acids by Nanopore Analysis. *Acc. Chem. Res.* **35**, 817-825 (2002)

33.   Manrao, E. A. *et al.* Reading DNA at single-nucleotide resolution with a mutant MspA nanopore and phi29 DNA polymerase. *Nat Biotech* **30,** 349–353 (2012).

34.   Cherf, G. M. *et al.* Automated forward and reverse ratcheting of DNA in a nanopore at 5-A precision. *Nat Biotech* **30,** 344–348 (2012).

35.   Robertson, J. W. F. *et al.* Single-molecule mass spectrometry in solution using a solitary nanopore. *PNAS* **104,** 8207–8211 (2007).

36.   Reiner, J. E., Kasianowicz, J. J., Nablo, B. J. & Robertson, J. W. F. Theory for polymer analysis using nanopore-based single-molecule mass spectrometry. *PNAS* **107,** 12080–12085 (2010).

37.   Kumar, S. *et al.* PEG-Labeled Nucleotides and Nanopore Detection for Single Molecule DNA Sequencing by Synthesis. *Sci. Rep.* **2,** (2012).

38.   Iqbal, S. M. & Bashir, R. *Nanopores: Sensing and Fundamental Biological Interactions*. (Springer, 2011).

39. Li, J., Greshow, M., Stein, D., Brandin, E & Golovchenko, J.A. DNA molecules and configurations in a solid-state nanopore microscope. *Nat. Mater.* **2**, 611-615 (2003)

40. Fologea, D., Uplinger, J., Thomas, B., McNabb, D. S. & Li, J. Slowing DNA Translocation in a Solid State Nanopore. *Nano Lett* **5,** 1734–1737 (2005).

41. Chen, P. *et al.* Probing Single DNA Molecule Transport Using Fabricated Nanopores. *Nano Lett.* **4,** 2293–2298 (2004).

42. Chen, P. *et al.* Atomic Layer Deposition to Fine-Tune the Surface Properties and Diameters of Fabricated Nanopores. *Nano Lett.* **4,** 1333–1337 (2004).

43. Dekker, C. Solid-state nanopores. *Nat Nano* **2,** 209–215 (2007).

44. Branton, D. *et al.* The potential and challenges of nanopore sequencing. *Nat Biotech* **26,** 1146–1153 (2008).

45. Venkatesan, B. M. & Bashir, R. Nanopore sensors for nucleic acid analysis. *Nat Nanotechnol* **6,** 615–624 (2011).

46. Venta, K., Shlmer, G., Puster, M., Rodriguez-Manzo, J. A., Balan, A.,Rosenstein, J. K., Shepard, K. & Drndic, M. *ACS Nano* (2013)

47. *Ghosal, S*. Electrokinetic-flow-induced viscous drag on a tethered DNA inside a nanopore. *Phys. Rev. E* **76,** 061916 (2007).

48. Van Dorp, S., Keyser, U. F., Dekker, N. H., Dekker, C. & Lemay, S. G. Origin of the electrophoretic force on DNA in solid-state nanopores. *Nat Phys* **5,** 347–351 (2009).

49. Sigalov, G., Comer, J., Timp, G. & Aksimentiev, A. Detection of DNA Sequences Using an Alternating Electric Field in a Nanopore Capacitor. *Nano Lett.* **8,** 56–63 (2008).

50. Keyser, U. F. *et al.* Direct force measurements on DNA in a solid-state nanopore. *Nat Phys* **2,** 473–477 (2006).

51. Peng, H. & Ling, X. S. Reverse DNA translocation through a solid-state nanopore by magnetic tweezers. *Nanotechnology* **20,** 185101 (2009).

52. Yeh, L.-H., Zhang, M., Joo, S. W. & Qian, S. Slowing down DNA translocation through a nanopore by lowering fluid temperature. *ELECTROPHORESIS* **33,** 3458–3465 (2012).

53.   Kowalczyk, S. W., Wells, D. B., Aksimentiev, A. & Dekker, C. Slowing down DNA Translocation through a Nanopore in Lithium Chloride. *Nano Letters* **12,** 1038–1044 (2012).

54. Wei, R., Martin, T.G., Rant, U. &Dietz, H.DNA_origami_gatekeepers for solid state nanopores. Angew. Chem. 51, 4864-4867 (2012)

55.   Lieberman, K. R. *et al.* Processive replication of single DNA molecules in a nanopore catalyzed by phi29 DNA polymerase. *J. Am. Chem. Soc.* **132,** 17961–17972 (2010).

56.   Keyser, U. F. Controlling molecular transport through nanopores. *J. R. Soc. Interface* **8,** 1369–1378 (2011).

57.   He, Y., Tsutsui, M., Fan, C., Taniguchi, M. & Kawai, T. Controlling DNA Translocation through Gate Modulation of Nanopore Wall Surface Charges. *ACS Nano* **5,** 5509–5518 (2011).

58.   Luan, B. *et al.* Base-by-base Ratcheting of Single Stranded DNA through a Solid-State Nanopore. *Phys Rev Lett* **104,** 238103 (2010).

59.   Venkatesan, B. M. *et al.* Stacked Graphene-Al2O3 Nanopore Sensors for Sensitive Detection of DNA and DNA–Protein Complexes. *ACS Nano* **6,** 441–450 (2012).

60.   Deamer, D. Nanopore Analysis of Nucleic Acids Bound to Exonucleases and Polymerases. *Annual Review of Biophysics* **39,** 79–90 (2010).

61.   Hummer, G., Rasaiah, J. C. & Noworyta, J. P. Water conduction through the hydrophobic channel of a carbon nanotube. *Nature* **414,** 188–190 (2001).

62.   Wei, C. & Srivastava, D. Theory of Transport of Long Polymer Molecules through Carbon Nanotube Channels. *Phys. Rev. Lett.* **91,** 235901 (2003).

63.   Xie, Y., Kong, Y., Soh, A. K. & Gao, H. Electric field-induced translocation of single-stranded DNA through a polarized carbon nanotube membrane. *The Journal of Chemical Physics* **127,** 225101–225101–7 (2007).

64.   Yeh, I.-C. & Hummer, G. Nucleic acid transport through carbon nanotube membranes. *PNAS* **101,** 12177–12182 (2004).

65.   Chen, M., Khalid, S., Sansom, M. S. P. & Bayley, H. Outer membrane protein G: Engineering a quiet pore for biosensing. *Proc Natl Acad Sci U S A* **105,** 6272–6277 (2008).

66.   Byl, O. *et al.* Unusual Hydrogen Bonding in Water-Filled Carbon Nanotubes. *J. Am. Chem. Soc.* **128,** 12090–12097 (2006).

67.   Naguib, N. *et al.* Observation of Water Confined in Nanometer Channels of Closed Carbon Nanotubes. *Nano Lett.* **4,** 2237–2243 (2004).

68.   Rossi, M. P. *et al.* Environmental Scanning Electron Microscopy Study of Water in Carbon Nanopipes. *Nano Lett.* **4,** 989–993 (2004).

69.   Liu, H. *et al.* Translocation of Single-Stranded DNA Through Single-Walled Carbon Nanotubes. *Science* **327,** 64–67 (2010).

CHAPTER 2 CARBON NANOTUBE BASED NANOFLUIDICS FOR DNA
ANALYSIS

In this chapter, successful integration of vertically aligned carbon nanotube
(CNT) and microfluidic systems for CNT mass transportation experiments is shown. .
The demonstration of DNA sensing using a single CNT based nanofluidic device
motivates the study of DNA transport in CNT membrane devices. My work focuses on
CNT forest synthesis, PDMS microfluidic device fabrication, ionic current measurement
and absorbance measurements of translocated DNA molecules.

This chapter begins with discussion of structure and properties of a single CNT.
This is followed by description of the CVD growth of vertically aligned CNT forest.
Characterization and further fabrication techniques of the CNT forest to synthesize CNT
membrane device chips are described. Results of DNA and nanoparticle transport from
CNT membrane device measurements are presented. The chapter concludes with
implications of the results and the need to move onto solid state nanopores.

2.1 CARBON NANOTUBES – STRUCTURE AND PROPERTIES

2.1.1 Physical Structure of Carbon Nanotubes

Elemental carbon can form a variety of structures based on its ability to exist in different
hybridization states. Two popular allotropes of Carbon are diamond and graphite, where
in carbon resumes sp^2 and sp^3 hybridization states respectively. Apart from graphite, sp^2
hybridized carbon can form open and closed cages of honey comb atomic arrangement.
The first structure of this type was discovered in 1985, when researchers from Rice

University reported the discovery of C_{60} spheres also referred to as Buckminster fullerenes[1]. Following the flood of research activity directed towards understanding the nature and properties of fullerenes and their applications, the first tubular carbon structures were reported by Iijima in 1991[2]. Popularly referred to as carbon nanotubes (CNTs), these hollow cylindrical tubes typically have diameter of the order of a few nanometers, and very high aspect ratio. Based on the number of concentric shells, CNTs can be categorized as single-walled carbon nanotubes (SWCNTs) and multi-walled carbon nanotubes (MWCNTs). A SWCNT forms the fundamental unit of a CNT. The SWCNT can be thought of as a grapheme sheet rolled up to form a hollow seamless cylinder. The diameter and helicity of the resulting CNT depend on the direction of rolling, which is represented by the chiral vector $\vec{C}_h = n\,\vec{a}_1 + m\,\vec{a}_2$. The integers n and m represent the number of unit vectors ($\vec{a}_1$ and $\vec{a}_2$) along the 2 dimensional graphene lattice. Thus, $\vec{C}_h$ can be defined as the vector that connects two crystallographically equivalent sites on the 2D grapheme plane (**Figure 2.1**). Depending on their chirality, CNTs can be classified as "zig-zag" (for m = 0), "arm-chair" (for n = m) or simply chiral. From the magnitude of the chiral vector, the diameter of the resulting CNT can be calculated using the formula:

$$d = \frac{|\bar{C}_h|}{\pi} = \frac{\sqrt{3}}{\pi}\, a_{C-C}\, \sqrt{n^2 + m^2 + nm} \qquad (1.1)$$

Where a_{C-C} is the C-C bond length (~ 1.42 Å)
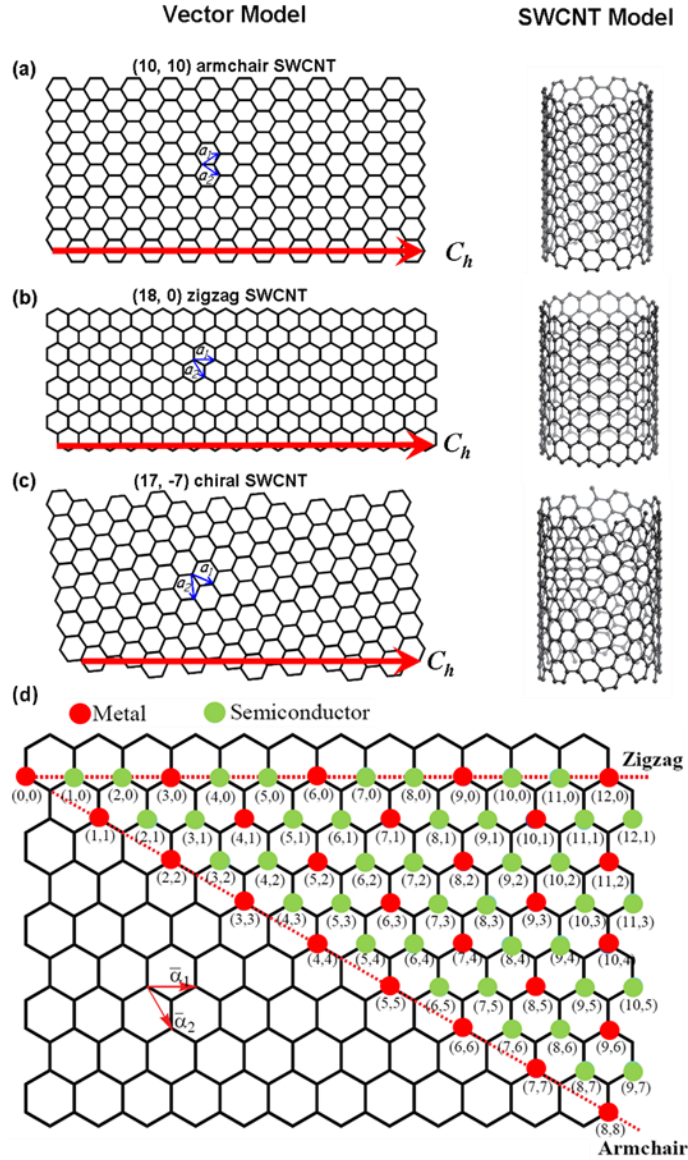
Figure 2.1 *(a)–(c) Schematic illustration of the SWCNT chirality: armchair (10,10), zigzag (18,0) and chiral (17,-7). The left column shows the rolling of graphene sheets to a carbon nanotube, illustrating the chiral vector $\bar{C}_h$ with respect to the unit vectors $\bar{a}_1$ and $\bar{a}_2$ in the honeycomb crystal lattice of the graphene. The right column displays the corresponding SWCNT models. (d) Chiral structures for possible SWCNT structures.*[3]

2.1.2 Electronic Structure of Carbon Nanotubes

The electronic structure of carbon nanotubes is very sensitive to their geometric structure.[4,5] While grapheme is a zero-gap semiconductor, CNTs can be metallic or semiconducting with different energy gaps based on the diameter and helicity of the CNTs.[3] SWCNT will be semiconducting if (m.n) values are such that [6]

$$\frac{(m-n)}{3} \neq \text{ integer} \tag{1.2}$$

And metallic if m, n are such that

$$\frac{(m-n)}{3} = \text{ integer} \tag{1.3}$$

As of current production technological standards, the helicity of grown SWCNTs is random during the growth process. Thus statistically, 2/3 of the randomly produced SWCNTs are semiconducting and 1/3 are metallic. The bandgap of a semiconducting SWCNT is given by

$$E_g = 2d_{CC}\gamma/\ D \tag{1.4}$$

where $dcc = 0.142$ nm is the C- C bond length of the graphene,; $\gamma = 2.5\text{-}3.2$ eV is the nearest-neighbor hopping parameter, and D is the diameter of the SWCNT.

2.2 WHY CNT MEMBRANE MICROFLUIDICS?

In recent years, there has been enormous interest in utilizing carbon nanotube as a nanochannels or nanopores.[7–14] CNTs emerge as a natural choice for nanofluidic applications primarily due to their structure – hollow inner volume accompanied by diameter that is uniform across the entire length and very high aspect ratio. Secondly, due to growing interest in understanding the motion of highly confined fluids, CNT nanofluidics has gained considerable attention from theoretical standpoint. Synthesis of sub 10nm channels is easy without the need for expensive fabrication set up as in the case of solid state nanopores. They have an atomically smooth surface and perfect uniformity over large distances, resulting in frictionless motion of fluid and particles. Recent studies show significantly faster transport in CNT comparing with nanochannels made from conventional materials.[15–17] For high quality CNTs, the chemistry and structures of the interior surface are well-defined, which simplifies theoretical simulations. Well-defined sites are available for chemical functionalization at the ends obtained from oxidation of the nanotube caps. Chemical modifications at these sites could affect and modulate ion and molecule flow through the tubes, giving scope for a wide variety of applications. To develop a fundamental understanding of mass transport inside CNT, transport measurement based on single SWCNT (diameter <2nm) has been developed in recent years.

Apart from the general advantages mentioned above, one of the important advances in CNT field that is of direct relevance to the sequencing community is the work done by my lab colleagues with respect to DNA translocation in single CNT devices.[15] As

already mentioned in the chapter 1, this study shows that the SWCNTs could be a clever

choice of nanopores that involve inexpensive fabrication of highly sensitive and robust

nanochannels, capable of single molecule DNA detection. While there are so many

advantages to the above mentioned devices, there is however one problem - the

individual CNT based nanofluidic device is difficult to fabricate and the diameter of the

CNT cannot be exactly controlled.

In order to overcome this problem, it was proposed that we fabricate large scale growth

of aligned CNTs, such that when a membrane device is created out of this array, DNA

threading through the CNTs could be sensed in-tandem using a functionalized STM tip.

(see **Figure 2.2**)
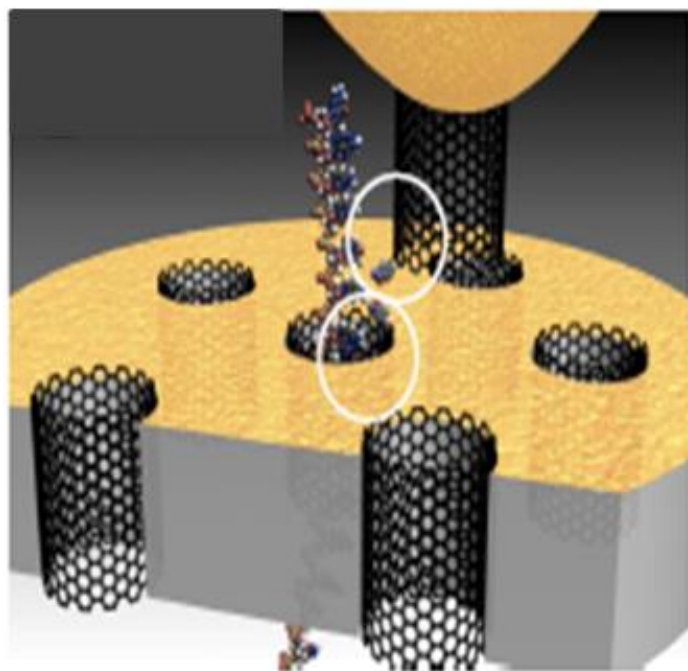
Figure 2.2 *Schematic of integrating array of CNTs within the STM set up for sequencing*

purpose.

Currently, measurements of mass and charge transport in the CNT are made mainly with membranes containing a large quantity ($\sim 10^{9\text{-}11}$tubes/cm^2) of CNTs, the orientation of which is either aligned or not aligned.[14,18–20] The membranes with aligned CNTs generally show better performance. However, it is difficult to grow high quality aligned CNT with diameters below 2nm. Various polymers have been cast onto the CNT film to fill the gaps between CNTs and form an impenetrable membrane. Subsequently, both ends of the CNT were opened by oxygen plasma. Recent research on CNT based nanofluidic devices has yield exciting applications in efficient gas filtration, chemical and biological separation, water desalination and programmable transdermal drug delivery.[21–23]

2.3 SYNTHESIS OF CNT MEMBRANES

2.3.1 Vertically Aligned CNT Forest Growth

A 1nm thick Fe layer and a 30 nm thick Al layer were deposited sequentially on a silicon chip containing a silicon nitride membrane using ion-beam sputtering or electron-beam deposition. The vertically aligned MWCNT forest was grown from this catalyst by chemical vapor deposition (CVD) using Ethylene as the carbon source at 850$^\text{o}$C for 70 seconds.[14] More supporting information related to the synthesis of vertically aligned forest growth protocol is given in Appendix B.

2.3.2 SEM, TEM Characterization

A scanning electron microscope (SEM) image of the as-grown vertically aligned MWCNT forest is shown in **Figure 2.3a**. The height of the CNT forest is about 42±5 μm under our growth condition. The inset in Figure 2b shows a transmission electron microscope (TEM) image of individual CNTs, confirming that these CNTs are multi-walled (~5-10 layers) and the inner and outer diameters are about 7 nm and 11 nm respectively. Bamboo structure is not observed in these MWCNTs. By analyzing more than 100 CNTs in TEM images, we obtained a histogram (**Figure 2.3 b**) of the CNT inner diameter distribution, with the peak around 7 nm. These carbon nanotubes were also characterized by Raman spectroscopy, confirming MWCNT structures due to the absence of radial breathing mode (**Figure 2.4**).
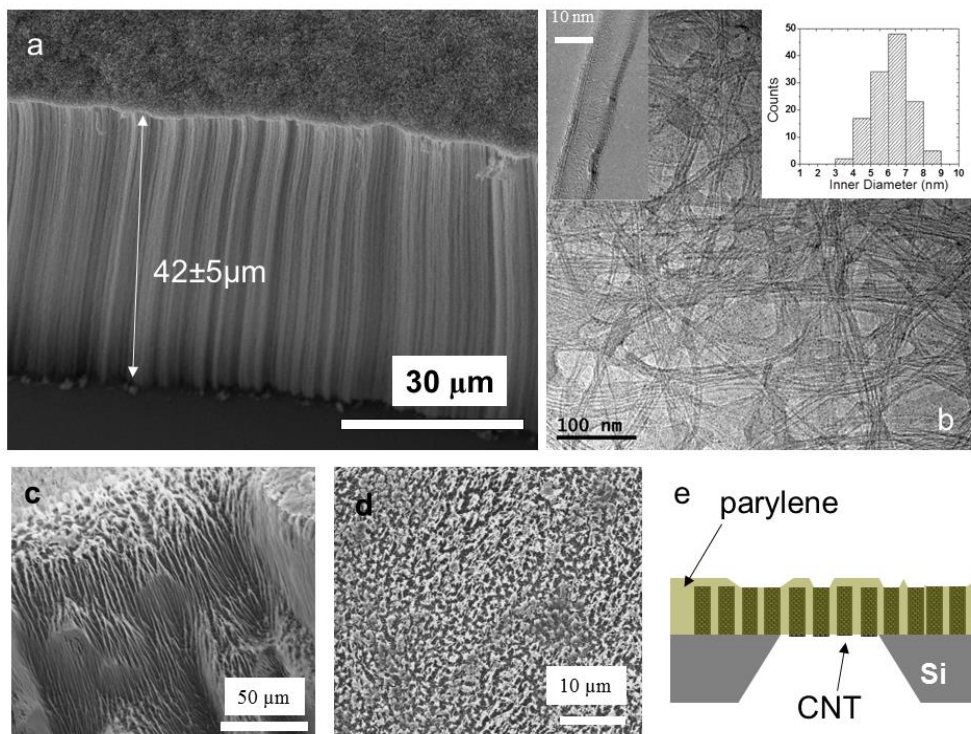
Figure 2.3. *SEM and TEM characterization(a) SEM image of the cross-section of the as-grown vertically aligned MWCNT forest. The average height of the CNT forest is about 42μm. (b) Low resolution TEM image of a large number of MWCNTs. The inset at the top left corner is a high resolution TEM image of one MWCNT. The inset at the top right corner shows the histogram of inner diameters of these MWCNTs. (c) A SEM image shows the cross-section of the parylene coated MWCNT membrane. (d) A SEM image shows the membrane surface after oxygen plasma treatment. (e) The schematic of the parylene encapsulated MWCNT forest membrane on a silicon support with a square window with size 35-100μm.*

2.3.3   Parylene Depostion and Membrane Fabrication

The fabrication of vertically aligned MWCNT forest membrane is based on the procedure

developed by Holt *et al.* [14]In brief, a 5mm square silicon chip with a square shaped free

standing silicon nitride membrane (35-100μm in width, 300nm in thickness) in the center

is first fabricated by KOH anisotropic wet etching. After the MWCNT forest is grown

uniformly on the whole surface, parylene is vapor deposited onto the MWCNT forest at

room temperature using a PDS 2010 LABCOTER (Specialty coating systems,

Indianapolis, IN). Immediately after deposition, the parylene film is planarized by

thermal annealing at $350^{o}C$ for two hour in argon atmosphere. SEM images in Figure 1c

suggest that the CNT forests are fully embedded in parylene. A two-step reactive ion

etching (RIE) process is used to sequentially remove the excess parylene film and the

300nm SiN layer from the backside of the chip. Then the chip is sequentially immersed in

$45^{o}C$ PAN etch solution (H_3PO_4:H_2O: HNO_3:CH_3COOH (16:2:1:1, volume ratio) for 5

minutes and in HCl (50% of concentrated HCl) for 30 minutes, to remove the exposed Al

and Fe layers from the backside. Then oxygen plasma (5-10 minutes, 7.2W, 550-600

mTorr) is used to remove the excess parylene, and to expose and open the CNT ends. The

surface of the membrane after oxygen plasma is shown in Figure 1d. The as-grown

parylene surface is hydrophobic. However, the parylene surface becomes hydrophilic

after oxygen plasma treatment. The hydrophilic parylene surface is stable and facilitates

the transport of particles. The schematic of the final device is shown in **Figure 2.5**
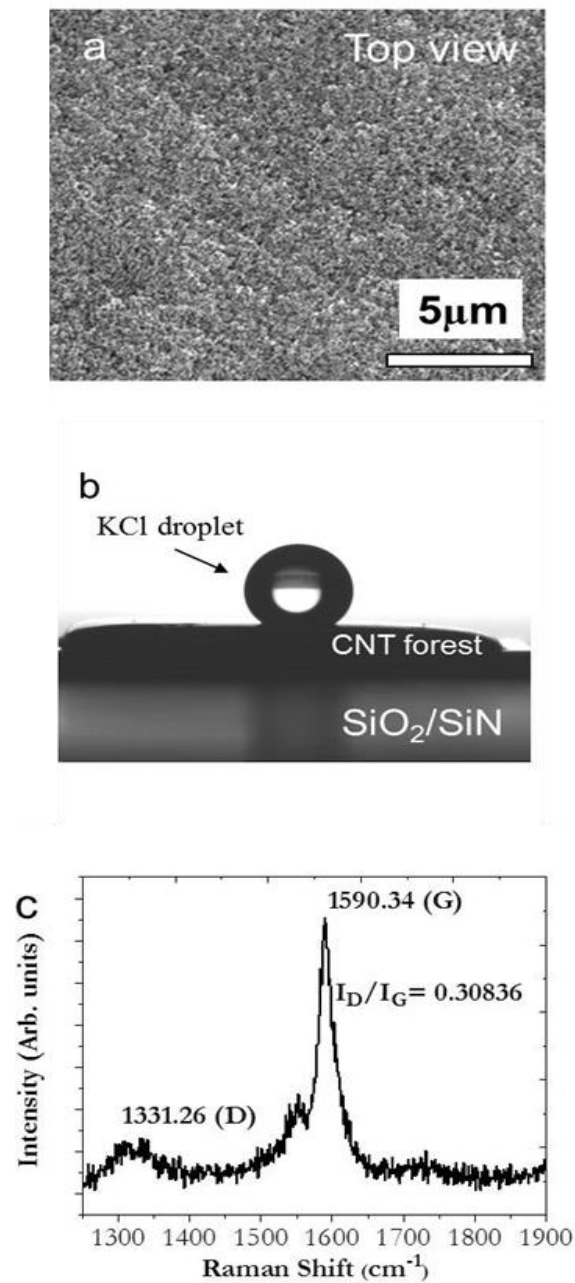
Figure 2.4 *CNT Forest characterization(a) SEM image of the top view of the as-grown vertically aligned MWCNT forest. (b) Optical image of an aqueous droplet (100mM KCl) on the as-grown MWCNT forest. The measured contact angle is 128°. (c) Raman spectroscopy of the MWCNT forest.*

2.4 CNT Membrane measurements

To start with, control experiments have been carried out to prove that within the applied bias and pressure range, the transport is through the inside of the CNT and not through any cracks or voids in the parylene film. The ionic current through the membrane is measured using the setup as shown in **Figure 2.5**
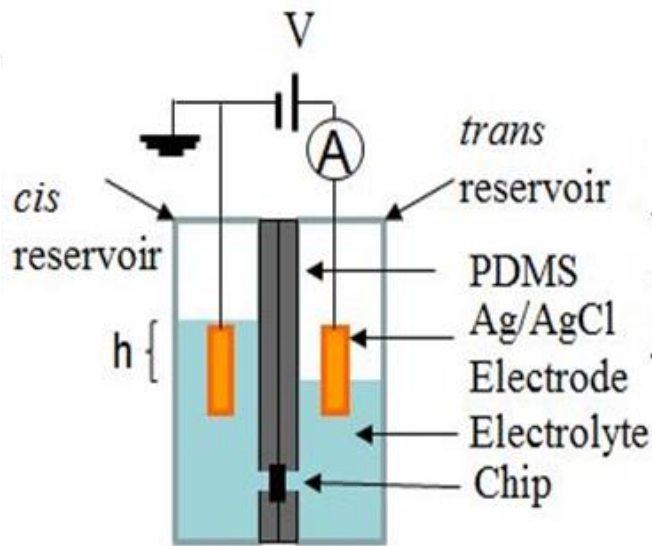
Figure 2.5 *Diagram of the ionic current measurement set up.*

When the control device with pure parylene thin film is fabricated and treated by the same process, no ionic current is observed . Similarly, when the CNT membrane is not treated by oxygen plasma, there is no measurable ionic current. With the increase of the oxygen plasma time, the measured ionic current initially increases and then flattens out (see supplementary information). The dependence of ionic current on oxygen plasma

39

time implies the ionic current is proportional to the number of opened CNTs in the membrane.

2.4.1 DNA AND NANOPARTICLE TRANSPORT

We also studied the translocation of gold nanoparticles with well-defined size under pressure and electric field. The 5nm Au NP is smaller than the average CNT inner diameter and the 10 nm Au NP is bigger than the average CNT inner diameter. We have measured more than 10 membranes and about 80% of the membranes only allow 5nm AuNPs to pass with only electric field applied (see one example in **Figure 2.6a**). However, the ratio reduced to about 40% when a pressure (294 Pa, about 3cm height difference) is applied. We discard the 60% membranes that also allow the passage of 10nm NPs. This fact also suggests that these parylene encapsulated CNT membranes are not suitable for high pressure applications. Therefore, we mainly study the transport driven by electrical field. If a pressure gradient is needed, the pressure was always below 294 Pa, a level at which no leaks were detected in the parylene membranes.

To understand the ion transport mechanisms in these large diameter MWCNTs, we measured the ionic conductance in KCl solution as a function of KCl concentration and solution pH. We first measured the ionic current through CNT forest membrane at different bias. The current-voltage (IV) curves are symmetric in the applied bias range (<2V) and a typical curve taken in 100mM KCl solution is shown in the inset of Figure 2b. The ionic conductance can be derived from the slope of the IV curve. We then plot the ionic conductance data as a function of KCl concentration in logarithmic scale. As shown in **Figure 2.6 (a)**, the ionic conductance is proportional to the KCl concentration when the concentration is above 0.1mM.
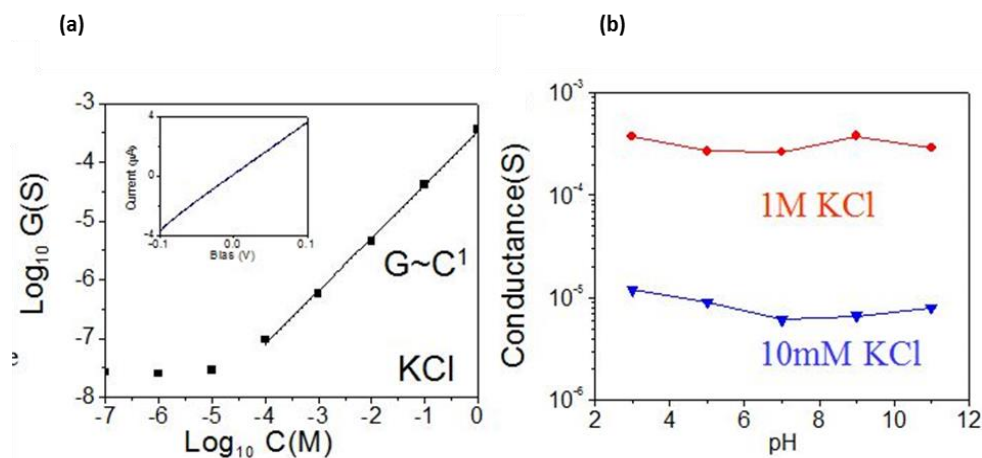
Figure 2.6 *Ionic conductance measurements(a) The ionic conductance vs. KCl concentration on a log-log scale. The solid line is a linear fit to the experimental data. The inset shows the I-V curve of the membrane in 100mM KCl solution. (b) The ionic conductance through the membrane as a function of pH in 1M KCl (red circle) and 10mM KCl (blue triangle) solutions. The solid lines are guides for the eye.*

The deviation at low salt concentration is previously explained by surface charge on the nanochannel/nanopore.[26] The proportionality at high salt concentration suggests the transport mechanism under electric field is electrophoresis. This is very different from the transport mechanism in individual SWCNTs with inner diameter below 2nm.[12,24] A unique power law relationship with exponent smaller than 1 is always observed in those single SWCNT fluidic devices. The origin of such behavior is attributed to the strong electroosmotic flow inside smaller diameter SWCNT. We further studied the ionic conductance as a function of pH and the result is shown in **Figure 2.6(b)**. We didn't

observe obvious change in ionic conductance when changing the pH of the KCl solution from 3 to 9. This is also different from the results of small diameter SWCNT, confirming that the electroosmosis is not an important transport mechanism in these MWCNTs of average 7nm diameter. This conclusion is also consistent with previous experiments and theoretical calculations.[10,25]

We then studied the transport of small molecules through these membranes. Anions $Fe(CN)_6^{3-}$ (hydrated diameter ~0.95 nm)[26] and cations $Ru(bipy)_3^{2+}$ (hydrated diameter ~1.18 nm)[16] were used in this study. The molecular structures of both ions are shown in **Figure 2.7(a)**. We first measured the IV curves and the results are shown in **Figure 2.7** (b). The solutions in the *cis/trans* reservoirs are $K_3Fe(CN)_6$ / KCl, $Ru(bipy)_3Cl_2$ / KCl and $Ru(bipy)_3Cl_2$ /$K_3Fe(CN)_6$. The KCl solution concentration is always100mM and the $K_3Fe(CN)_6$ and $Ru(bipy)_3Cl_2$ solutions are always 25mM. At the same bias, the current of $K_3Fe(CN)_6$ / KCl (green curve) is slightly smaller than the current of KCl / KCl (black curve). However, the current of $Ru(bipy)_3Cl_2$ / KCl (red curve) is almost half the value of KCl / KCl. This suggests that cation $Ru(bipy)_3^{2+}$ passes the MWCNT membrane less easily. Meanwhile, there is a slight asymmetry in the IV curve and the current is smaller at negative bias, which also reflecting the smaller mobility of cation $Ru(bipy)_3^{2+}$. We also measured the IV curve of $Ru(bipy)_3Cl_2$ /$K_3Fe(CN)_6$. The current is further reduced compared with $Ru(bipy)_3Cl_2$ / KCl. The decrease in current also confirms that the ions are transport through the inside of the MWCNT.[7] Because the ionic current is contributed by all the ion species in the solution, we then directly measure the concentration of translocated ions at *trans* reservoir after applying a bias between two reservoirs for 90

minutes. In this experiment, the *cis* reservoir is filled with 25mM $K_3Fe(CN)_6$ or

$Ru(bipy)_3Cl_2$ in 100mM KCl (pH 7) solution. The *trans* reservoir is filled with 100mM

KCl solution. The concentration of $Fe(CN)_6^{3-}$ ions is determined by the pronounced redox

peak at 0.18 V *versus* Ag/AgCl in square wave voltammetry. The concentration of

$Ru(bipy)_3^{2+}$ ion is determined by the two adsorption peaks at 285nm and 450nm in UV-

vis spectra. As shown in **Figure 2.7(c)**, the anion $Fe(CN)_6^{3-}$ can only be driven across

the membrane by positive bias and the cation $Ru(bipy)_3^{2+}$ can only be driven across the

membrane by negative bias. In addition, the concentration of transported ion increases

with the applied bias. At zero bias, the concentration of transported ion is not detectable,

confirming diffusive transport is inefficient for these membranes. These results are

consistent with the electric field induced electrophoretic transport. Between the two ions,

the anion $Fe(CN)_6^{3-}$ is apparently much easier to transport through the MWCNTs and the

concentration is about 25 times higher at the *trans* reservoir when the bias magnitude of

1.5V is applied for 90 minutes between the two reservoirs. This observation is consistent

with the IV curves in **Figure 2.7b**.
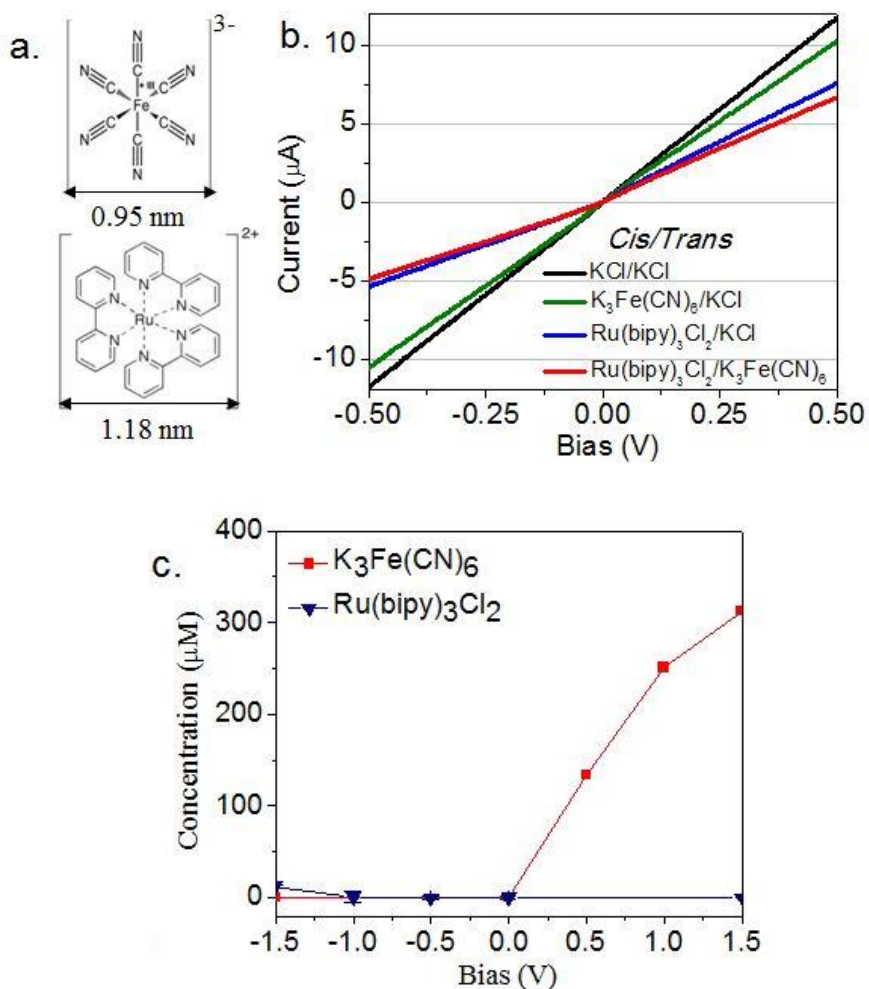
Figure 2.7. *Transport of small molecules (a) Schemes of the molecular structure of anion Fe(CN)$_6^{3-}$ and cation Ru(bipy)$_3^{2+}$ and their hydrated diameters. (b) The measured I-V curves when the cis and trans reservoirs are filled with K$_3$Fe(CN)$_6$/KCl(green line), Ru(bipy)$_3$Cl$_2$/KCl and Ru(bipy)$_3$Cl$_2$/ K$_3$Fe(CN)$_6$, respectively. The black curve is a control experiment in which both reservoirs are filled with KCl. The concentration of KCl solution is 100mM and the concentration of anion Fe(CN)$_6^{3-}$ or cation Ru(bipy)$_3^{2+}$ is 25mM. (c) The concentration of anion Fe(CN)$_6^{3-}$(red square) and cation Ru(bipy)$_3^{2+}$ (blue triangle) at the trans reservoir as a function of the applied bias. The time is always 90 minutes. The solid lines are guides for the eye.*

What is the reason for the big difference in transport between anion $Fe(CN)_6^{3-}$ and cation $Ru(bipy)_3^{2+}$? Interestingly, the much higher rejection of cation $Ru(bipy)_3^{2+}$ than anion $Fe(CN)_6^{3-}$ is opposite to the observation in small diameter DWCNTs,[26] in which the anion is rejected by the negative charged carboxyl groups at the CNT ends. Because of the much bigger diameter of MWCNT in these membranes, the charges carried by the ions and at the CNT ends are likely fully screened by the electric double layer (EDL) at 100mM KCl concentration. Therefore, the electrostatic interactions between ions and CNT ends are not important. In addition, the hydrated diameter of anion $Fe(CN)_6^{3-}$ is only slightly smaller than cation $Ru(bipy)_3^{2+}$. So size induced steric hindrance will not contribute significantly to such obvious ion selectivity. The reason may be attributed to the stronger molecular interaction between the cation $Ru(bipy)_3^{2+}$ and the curved CNT inner surface. We also compared the transport between anion $Fe(CN)_6^{3-}$ and cation $Ru(bipy)_3^{2+}$ through nominal 20 nm pore diameter AAO membrane and the difference is still obvious but much smaller **(see Figure 2.8)**. This experimental result supports that the ion selectivity in CNT membrane is mainly due to surface interactions.
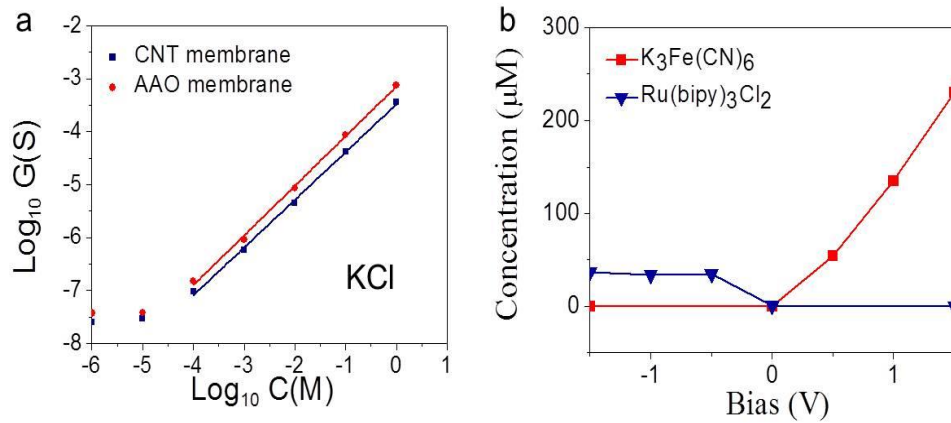
Figure 2.8 *(a) The log-log plot of ionic conductance as a function of KCl concentration for both CNT membrane (red curve) and AAO membrane (blue curve). The experimental data (dot) are fitted by linear functions. (b) The concentration of anion $Fe(CN)_6^{3-}$ (red square) and cation $Ru(bipy)_3^{2+}$ (blue triangle) at the trans reservoir as a function of the applied bias. The time is always 90 minutes. The solid lines are guides for the eye.*

We also studied the transport of DNA through this membrane. Theoretical simulations have made predictions that single-stranded DNA can pass through a CNT under external electric field.[27,28] The translocation of short single-stranded DNAs through SWCNT has also been reported.[27,29] TEM revealed clear images of ssDNAs inside SWCNT, which were injected by electrical field.[30] Interestingly, the ionic current signatures during DNA translocation in individual SWCNT are quite different from those in silicon based nanopore/nanochannel.[20,31] There are still no studies on the transport of DNA though big diameter MWCNT membranes. Here, we investigated the translocation of a 12mer ssDNA (GTCGTCGTCGTC) through the MWCNT membrane. As shown in Figure 4a,

46

no DNA is detected in UV-vis spectrometer at the *trans* reservoir when a bias of 3V is applied across the membrane for 60 minutes. The same magnitude of bias is also applied for a longer time (> 120 minutes) and still no DNA is detected by UV-vis spectrometer. The difficulty of transporting ssDNA through these MWCNT membranes is probably due to (1) the strong interactions between CNT inner surface and ssDNA, and (2) the lack of electroosmosis in these big diameter MWCNTs. It has been well-studied that ssDNA will adsorb strongly to CNT outer surface due to pi-pi stacking.[34] Therefore, without the efficient electroosmotic pumping, the applied electric field is likely not enough to overcome the interaction force between ssDNA and CNT inner surface and cannot drive ssDNA through the large diameter MWCNT. To test this hypothesis, we increase the driving force by adding a small pressure difference (98 Pa) between two reservoirs. As the green curve shown in **Figure 2.9a,** ssDNA is detected at the *trans* reservoir. We also studied the electrophoretic transport of negatively charged 5nm gold nanoparticles. As shown in **Figure 2.7b**, 5nm gold nanoparticles can be detected at the *trans* reservoir by UV-vis spectrometer after applying a 2V bias across the membrane for 6 hours. Although the 5nm gold nanoparticle has bigger size than 12mer ssDNA, the interaction between gold NPs and CNT surface is presumably weaker than ssDNA due to the citrate coating on the surface of gold NPs. Therefore, 5nm gold NPs are easier to transport through the MWCNT membrane. These results suggest the interactions between particles and the hydrophobic CNT inner surface strongly affect their electrophoretic transport through these large diameter MWCNT membranes.
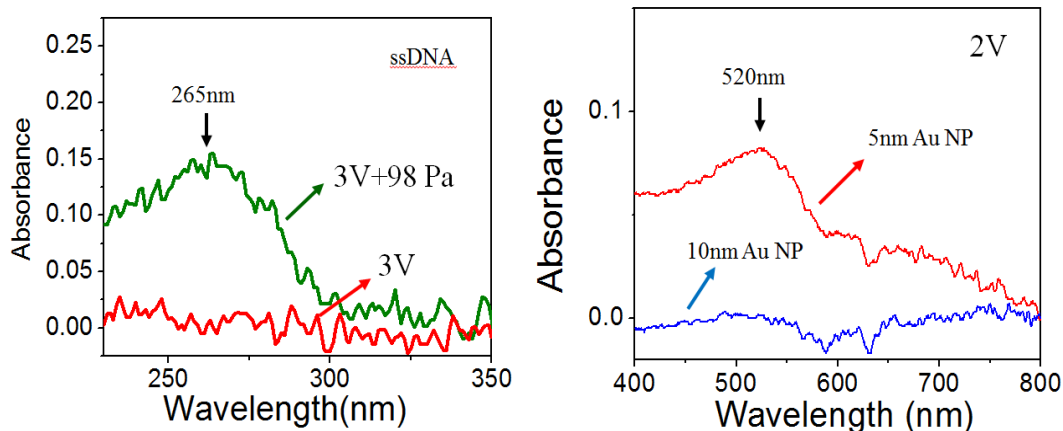
Figure 2.9. *(a) UV-vis spectra of 12mer ssDNA at the trans reservoir after applying 3V bias (red) and after applying 3V bias and 98 Pa pressure simultaneously for 60 minutes (green). The solution in the cis reservoir is 5μM ssDNA in 100mM KCl solution. (b) UV-vis spectra of 5nm (red) and 10nm (blue) Au nanoparticles at the trans reservoir after applying a 2V bias for 6 hours. No pressure is applied.The concentration of Au NPs at the cis reservoir is 60 μM in 1mM KCl solution.*

2.4.2 Chemical Modification Effects on Transport

Finally, we studied how chemical modification of CNT membrane affects particle transport. The chemical modification at the CNT ends may affect the particle transport by steric hindrance, electrostatic interactions and chemical bonding. During the fabrication, the CNT ends acquire carboxylate groups due to the oxygen plasma process. A variety of

chemical modifications on the CNT ends can be easily accomplished by using well-established carbodiimide chemistry to couple carboxylic acid group with amine group. Similar to previous reports,[8,32] a very simple molecule, ethanolamine is used to modify the membrane, which will neutralize the negatively charged carboxyl groups (when pH>4) and may hinder the particle transport at the pore entrance. The schematics of the unmodified and modified CNT ends are shown in the inset of **Figure 5a.** We first measured ionic current through these MWCNT membranes before and after the chemical modification in KCl solution. No difference in the ionic current was observed **(see Figure S4)**. This suggests that the modification does not affect the transport of small ions, such as K^+ and Cl^-. We then measured the transport of bigger particles, including 12mer ssDNA (GTCGTCGTCGTC) and 5nm gold NPs under a small pressure (~147 Pa). The results are shown in Figure 5. The transport of ssDNA and 5nm diameter gold NPs across the membrane is obviously suppressed by the modification (blue curves in **Figure 5 a and b).** The observed effect is most likely due to steric hindrance because there is no charge on the CNT ends after modification. To further confirm the chemical modification effect, we use oxygen plasma to remove the modified molecules and then redo the modification. As shown in Figure 5a, the CNT membranes can be repeatedly modified and hinder the transport of ssDNA. Here we just use a simple molecule to demonstrate the capability of reversible chemical modification on these parylene embedded MWCNT membranes. By using rational designed molecules, we expect to enhance selectivity and electroosmotic flow in these MWCNT membranes.[15]
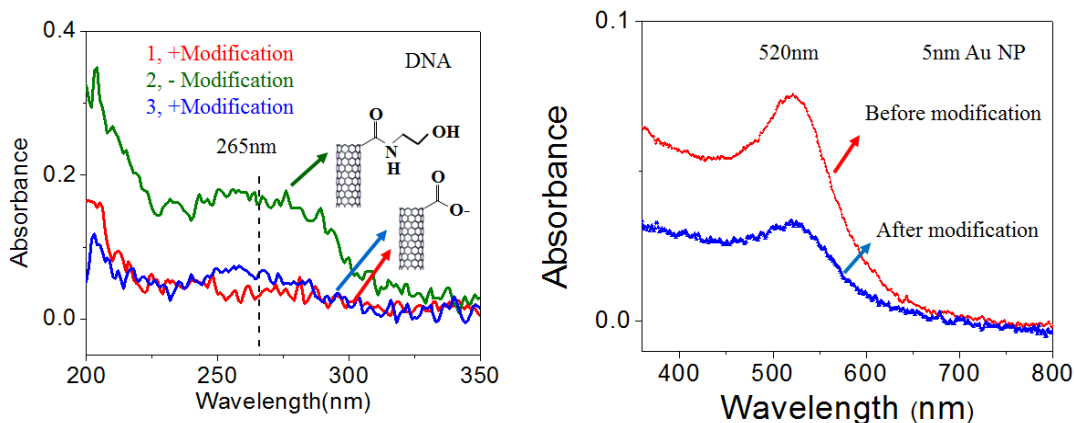
Figure 2.10 *Effect of modification on transport (a) UV-vis spectra of 12mer ssDNA at the trans reservoir after applying 147 Pa (1.5cm water height difference) for 120 minutes for membrane after ethanolamine modification(red), after removing the modification by oxygen plasma (green) and after ethanolamine modification again(blue). The initial concentration of ssDNA at the cis reservoir is 5μM. (b) The UV-vis spectra of 5nm Au NPs in 1mM KCl at the trans reservoir before (green) and after (blue) ethanolamine modification. The concentration of Au NPs at the cis reservoir is 10 μM in 1mM KCl solution. A pressure of 147 Pa is applied for 36 minutes.*

2.5 CONCLUSIONS

In summary, we have successfully fabricated parylene encapsulated vertically aligned large diameter MWCNT membranes. In contrast to small diameter DWCNTs and SWCNTs, electroosmosis in these large diameter MWCNTs is weak. Therefore an electric field can only provide a weak force to drive ions and small molecules. The transport is also significantly affected by the interactions with the hydrophobic CNT

inner surface, leading to enhanced selectivity for small molecules. Chemical modification on these MWCNT membranes also shows obvious effect on the translocation of particles.

From the measurements of the forest membranes, it is however obvious that single molecule information is hard to obtain via this route. Thus, while single CNT based devices pose the disadvantage of lack of fabrication control and array model CNT forest membrane based devices lack single molecule precision, we focus on the next possible route to nanofluidic DNA sensing – solid state nanopores. Chapter 4 discusses functionalized nanopore fabricaton and results. Before we move on to chapter 4, we discuss the concept of functionalization in chapter 3. This is useful to understand the implications of functionalization in other kinds of sequencing approach (such as recognition by tunneling). Before moving to chapter 3, it is important to mention that the possibilities of incorporating CNT properties in nanopore platform have also been explored through the synthesis and use of graphene nanopores in a collaborative effort with Dr. Smirnov (New Mexico State University) and Dr. He (Florida International University). The details of this work are presented in Appendix B.

2.6 REFERNCES

1.   Kroto, H. W., Heath, J. R., O'Brien, S. C., Curl, R. F. & Smalley, R. E. C60: Buckminsterfullerene. *Nature* **318,** 162–163 (1985).

2.   Helical microtubules of graphitic carbon. at <http://www.nature.com/nature/journal/v354/n6348/pdf/354056a0.pdf>

3.   Dresselhaus, M. S., Dresselhaus, G. & Avouris, P. *Carbon Nanotubes: Synthesis, Structure, Properties and Applications*. (Springer, 2001).

4.   Odom, T. W., Huang, J.-L., Kim, P. & Lieber, C. M. Structure and Electronic Properties of Carbon Nanotubes. *J. Phys. Chem. B* **104,** 2794–2809 (2000).

5.   Meyyappan, M. *Carbon Nanotubes: Science and Applications*. (CRC Press, 2004).

6.   *Micro- and Opto-Electronic Materials and Structures: Physics, Mechanics, Design, Reliability, Packaging: Volume 1 Materials Physics / Materials ... Physical Design / Reliability and Packaging*. (Springer, 2007).

7.   Hummer, G., Rasaiah, J. C. & Noworyta, J. P. Water conduction through the hydrophobic channel of a carbon nanotube. *Nature* **414,** 188–190 (2001).

8.   Whitby, M. & Quirke, N. Fluid flow in carbon nanotubes and nanopipes. *Nat Nano* **2,** 87–94 (2007).

9.   Noy, A. *et al.* Nanofluidics in carbon nanotubes. *Nano Today* **2,** 22–29 (2007).

10.   Schoch, R. B., Han, J. & Renaud, P. Transport phenomena in nanofluidics. *Rev. Mod. Phys.* **80,** 839–883 (2008).

11.   Mattia, D. & Gogotsi, Y. Review: static and dynamic behavior of liquids inside carbon nanotubes. *Microfluid Nanofluid* **5,** 289–305 (2008).

12.   Lee, C. Y., Choi, W., Han, J.-H. & Strano, M. S. Coherence Resonance in a Single-Walled Carbon Nanotube Ion Channel. *Science* **329,** 1320–1324 (2010).
13.   Hinds, B. J. *et al.* Aligned Multiwalled Carbon Nanotube Membranes. *Science* **303,** 62–65 (2004).

14.   Holt, J. K. *et al.* Fast Mass Transport Through Sub-2-Nanometer Carbon Nanotubes. *Science* **312,** 1034–1037 (2006).

15.   Liu, H. *et al.* Translocation of Single-Stranded DNA Through Single-Walled Carbon Nanotubes. *Science* **327,** 64–67 (2010).

16.   Strano, M. S. *et al.* Electronic Structure Control of Single-Walled Carbon Nanotube Functionalization. *Science* **301,** 1519–1522 (2003).

17.   Qin, X., Yuan, Q., Zhao, Y., Xie, S. & Liu, Z. Measurement of the Rate of Water Translocation through Carbon Nanotubes. *Nano Lett.* **11,** 2173–2177 (2011).

18.   Wu, J., Gerstandt, K., Zhang, H., Liu, J. & Hinds, B. J. Electrophoretically induced aqueous flow through single-walled carbon nanotube membranes. *Nat Nano* **7,** 133–139 (2012).

19.   Majumder, M., Chopra, N. & Hinds, B. J. Mass Transport through Carbon Nanotube Membranes in Three Different Regimes: Ionic Diffusion and Gas and Liquid Flow. *ACS Nano* **5,** 3867–3877 (2011).

20.   Sun, X., Su, X., Wu, J. & Hinds, B. J. Electrophoretic Transport of Biomolecules through Carbon Nanotube Membranes. *Langmuir* **27,** 3150–3156 (2011).

21.   Fornasiero, F. *et al.* Ion exclusion by sub-2-nm carbon nanotube pores. *PNAS* **105,** 17250–17255 (2008).

22.   Corry, B. Designing Carbon Nanotube Membranes for Efficient Water Desalination. *J. Phys. Chem. B* **112,** 1427–1434 (2008).

23.   Wu, J. *et al.* Programmable transdermal drug delivery of nicotine using carbon nanotube membranes. *PNAS* **107,** 11698–11702 (2010).

24.   Okada, T., Kaneko, T., Hatakeyama, R. & Tohji, K. Electrically triggered insertion of single-stranded DNA into single-walled carbon nanotubes. *Chemical Physics Letters* **417,** 288–292 (2006).

25.   Liang, X. & Chou, S. Y. Nanogap Detector Inside Nanofluidic Channel for Fast Real-Time Label-Free DNA Analysis. *Nano Lett.* **8,** 1472–1476 (2008).

26.   Lulevich, V., Kim, S., Grigoropoulos, C. P. & Noy, A. Frictionless Sliding of Single-Stranded DNA in a Carbon Nanotube Pore Observed by Single Molecule Force Spectroscopy. *Nano Lett.* **11,** 1171–1176 (2011).

27.   Miserendino, S., Yoo, J., Cassell, A. & Tai, Y.-C. Electrochemical characterization of parylene-embedded carbon nanotube nanoelectrode arrays. *Nanotechnology* **17,** S23 (2006).

28.   Shoda, M., Bandow, S., Maruyama, Y. & Iijima, S. Probing Interaction between ssDNA and Carbon Nanotubes by Raman Scattering and Electron Microscopy. *J. Phys. Chem. C* **113,** 6033–6036 (2009).

29.   Karnik, R. *et al.* Electrostatic Control of Ions and Molecules in Nanofluidic Transistors. *Nano Lett.* **5,** 943–948 (2005).

30.   Stein, D., Kruithof, M. & Dekker, C. Surface-Charge-Governed Ion Transport in Nanofluidic Channels. *Phys. Rev. Lett.* **93,** 035901 (2004).

31.   Strano, M. S. *et al.* Electronic Structure Control of Single-Walled Carbon Nanotube Functionalization. *Science* **301,** 1519–1522 (2003).

32.   Lee, C. Y., Choi, W., Han, J.-H. & Strano, M. S. Coherence Resonance in a Single-Walled Carbon Nanotube Ion Channel. *Science* **329,** 1320–1324 (2010).

3. DNA BASE RECOGNITION

3.1 SELF-ASSEMBLED MONOLAYER TECHNIQUE

Self-assembly (SA) involves spontaneous organization of interacting components to form ordered supramolecular architectures without external manipulation. Self-assembly occurs in many naturally occurring biological processes- such as spontaneous formation of double stranded DNA helix, formation of lipid bi-layers etc.[1–4] Molecular self-assembly can generate ordered structures in 2D (monolayer) as well as 3D(crystal). The simplicity of SAM formation process makes it inherently manufacturable and thus technologically attractive for surface modification. Hence, this technique has gained significance in many areas of technology such as macromolecular science,[5,6] crystal engineering,[7,8] molecular devices[7,9,10] etc.

Self-assembled monolayers (SAMs) can be formed as a result of spontaneous chemisorption or physisorption. Alkanes adsorbed on highly oriented pyrolytic graphite (HOPG) are physisorbed SAMs[11–17], while alkanethiolate SAMs on metals constitute a case of chemisorbed SAMs.[18–21]

Three components constitute a SAM – a head group, a chain structure and a tail group. (see **Figure 3.1**) When the metal or metal oxide substrate is left in a solution of the SAM molecules, the head group gets chemisorped onto the metal surface.

In this dissertation, we use Alkanethiol SAM, where the thiol group is the head group (point of attachment to the surface). Ethanol is a common solvent for Alkane thiol SAMS, as it is not easily incorporated into the SAM.
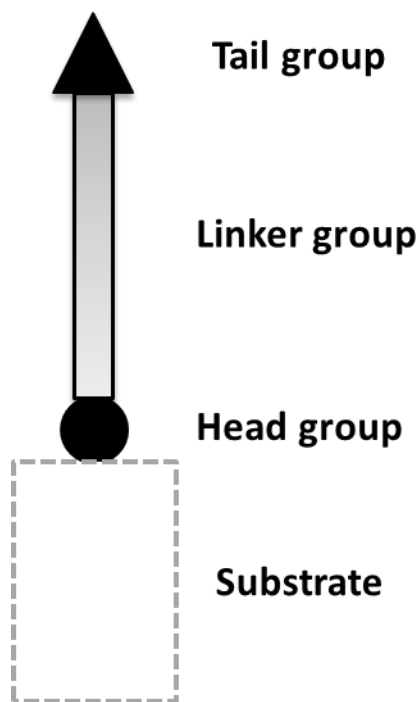
Figure 3.1 *A SAM Molecule.*

SAM Formation in Ethanolic solutions have been extensively studies and time-resolved characterizations establish the mechanism of SAM formation.[18,19] The formation of SAMs occurs through two distinct steps (see **Figure 3.2**): first, a rapid adsorption process occurs followed by a slower consolidation process that can take hours during which the chains stack together to form ordered arrays. It is during this later phase that lateral diffusion occurs causing a reduction of defects and an enhanced packing of the chains. It has been established that contaminants present on metal surface get displaced by the thiol linkers during SAM formation, and this is one of the advantages of functionalizing nanoscale surfaces with SAMs.
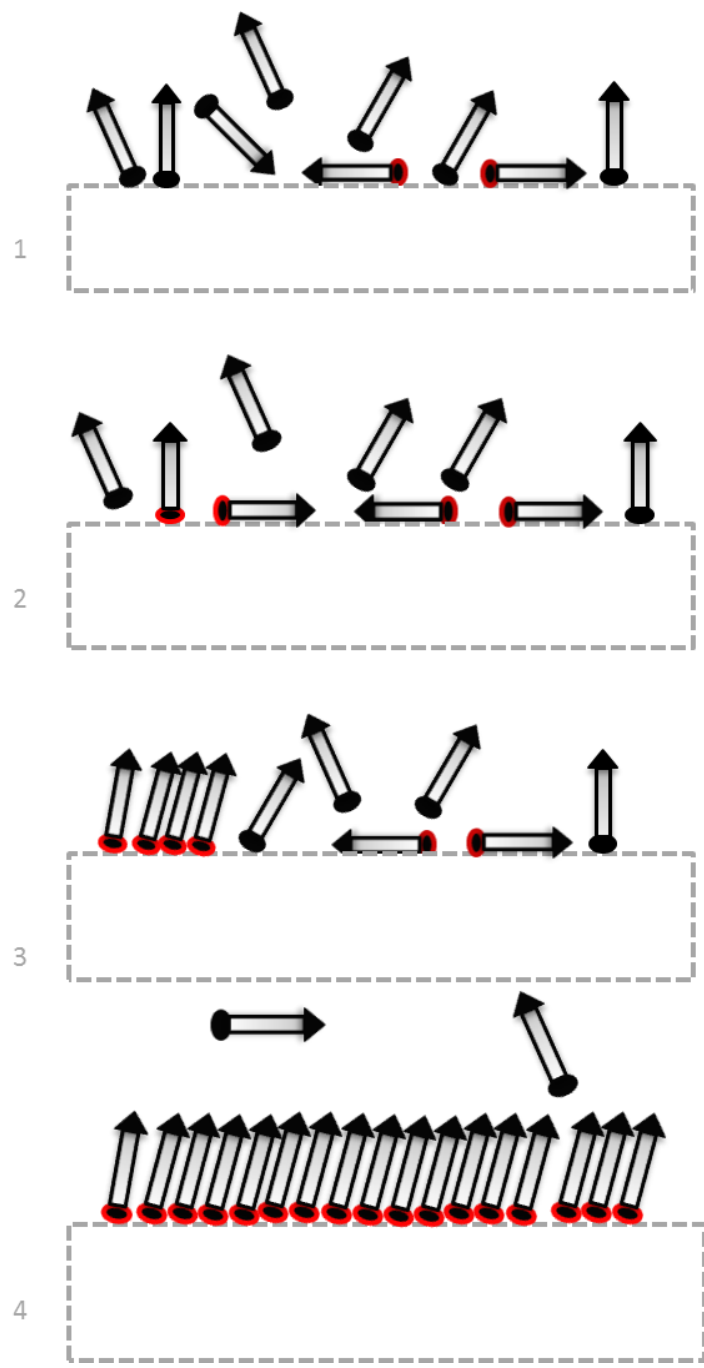
Figure 3.2 *Schematic of Self-assembled Monolayer Growth Mechanism (adapted from.*

Vericat et al[20]) The final self assembly of SAM molecules bonded to the substrate

uniformly without any defects, is usually possible after a timeframe of 24 hours.

3.2 BASE DIFFERENTIATION MECHANISM

3.2.1 Recognition tunneling

Sequencing by recognition is a scheme of sequencing DNA where a binding molecule recognizes each base of the DNA and produces a measurable and distinct electrical signal. Theoretical calculations have demonstrated that electron tunneling could be used to differentiate between bases of the DNA when the molecule is trapped between two closely held electrodes. [21]An ideal system to experimentally verify this hypothesis is the scanning tunneling microscope(STM). In the STM, a very sharp metallic probe is approached to a conductive surface until a predetermined tunneling current is achieved. From quantum mechanics, the wavefunction for a particle to tunnel through a one dimensional potential barrier is given by $\Psi(x) = A\, e^{\left(-\sqrt{\frac{2m(V-E)}{h^2}}\, x\ \right)}$ where E is the energy of the particle and V is the potential barrier. By squaring this, we get the probability density of finding a particle at any given location in the one dimensional space as $\Psi^2(x) = A^2\, e^{\left(-2\sqrt{\frac{2m(V-E)}{h^2}}\, x\ \right)}$. The expression indicates that the probability of finding the particle distance x away through a potential barrier falls off exponentially with x. Thus, as the tip is moved farther away from the surface, the current will drop off exponentially.[22] This extreme electronic sensitivity could therefore be tapped to distinguish the the bases of DNA molecule trapped in the STM junction. However, it is almost impossible to use bare STM tips to align individual DNA base with subangstrom precision and the gap distance in the calculation is too small to pass single-strand DNA through easily. It is here that, the use of self-assembled monolayers becomes invaluable.

My colleagues attempted a series of STM experiments in pursuit of differentiating

DNA bases. At the very outset it was found that functionalizing the STM tip and

substrate with a SAM capable of specific hydrogen bon structures (with DNA

nucleosides) sharpened the current signal distribution by an order of magnitude. 4-

mercaptobenzoic acid was selected as the recognition or reader molecule. In nonpolar

environment, the OH group of the benzoic acid molecule behaves as hydrogen bond

donor and the carbonyl bond, as hydrogen bond acceptor. Density functional calculation

predicted that functionalizing the tip and substrate with recognition molecule SAM could

reduce the contact resistance to the nucleosides thus allowing electronic signatures of all

four DNA nucleosides to be resolved in a tunneling gap.[23] The calculations indicated that

when individually trapped in a 2.5nm gap with the recognition molecule, each of the four

nucleosides formed four distinct hydrogen bonding complexes (see **Figure 3.3**).[24] The

experiments agreed with the predicted results and established that functionalized

electrodes could lower contact resistance as well as enable selective orientations at the

tunnel junction.
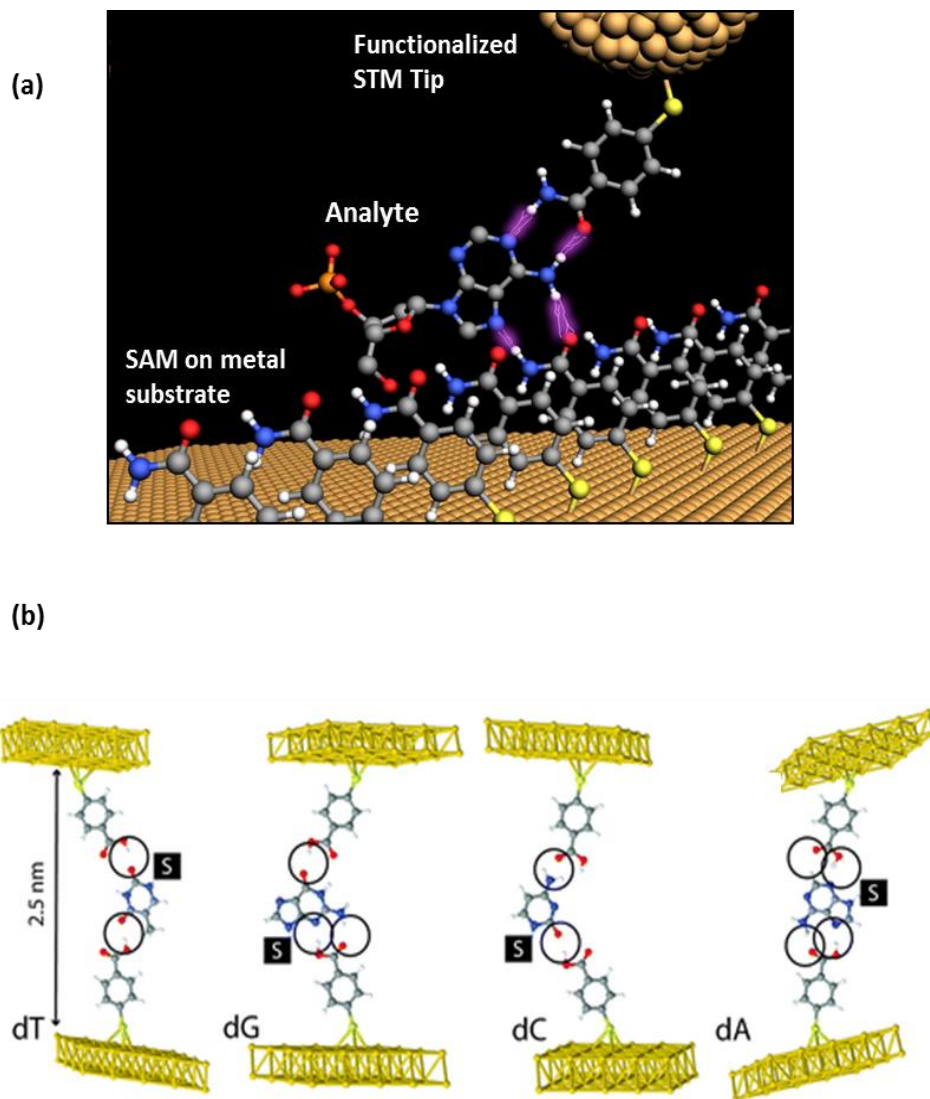
Figure 3.3 *(a) Schematic of recognition via tunneling in STM with SAM functionalized tip and substrate. (b) The different Hydrogen bonding structures that are predicted to form by 4-Mercaptobenzoic acid with different nucleosides when the tip and substrate are separated by 2.5nm tunnel gap.* [24]

3.2.2 Imidazole – Universal Reader Molecule

4-Mercapto Benzoic acid formed the first generation of a series of reader molecules that were synthesized subsequently. While 4-Mercapto benzoic acid functionalization demonstrated nucleotiode differentiation, its use is restricted to nonpolar solvents. Since aqueous medium is the preferred medium when it comes to ambient dna sequencing, a water-friendly variant of the original reader; 4-mercaptobenzamide was synthesized and tested. While this reader molecule could distinguish between bases from short oligomers[25], one problem with 4-mercaptobenzamide functionalization was the lack of tunneling signals from Thymine nucleoside.
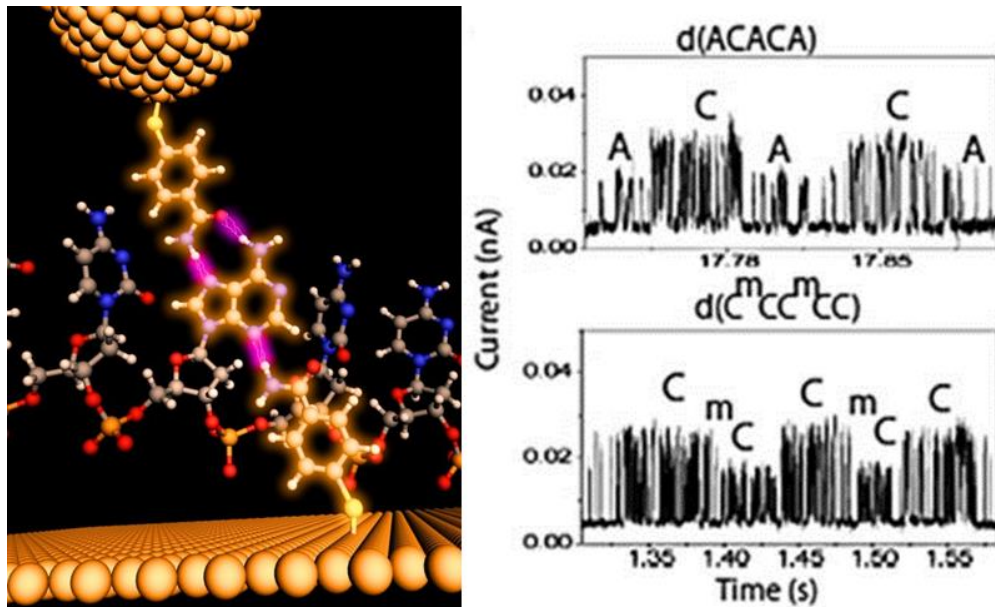
Figure 3.4 *Schematic of Tunneling .Nucleotide differentiation in short oligomers with Benzamide functionalized tip and substrate.[25]*

Hence, the need for a reader molecule that could give tunneling signals with all the bases in aqueous medium persisted and organic chemists from our lab proposed a new reader molecule, 4(5)-(2-mercaptoethyl)-1*H*-imidazole-2-carboxamide (see **figure 3.4**). Also referred to as Imidazole reader, this chemical reagent can recognize all naturally occurring DNA bases due to its ability to form non-covalent complexes(through Hydrogen bonding) with individual DNA bases and thus generate recognizable electronic signatures under an electrical bias. Hence it is referred to as 'universal reader'.

The complete description and details of synthesis and characterization of this molecule are provided by Liang et al.[26] . The data presented therein show that the 1-*H*-imidazole-2-carboxamide exists in a neutral form between pH 6–10. NMR studies indicate that naturally occurring nucleosides interacted with 1-*H*-imidazole-2-carboxamide through hydrogen bonding in a tendency of dG>dC≫dT>dA..
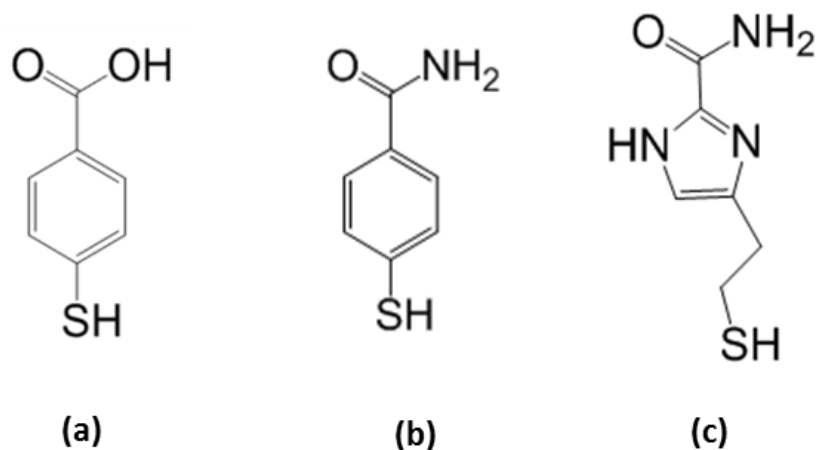
Figure 3.5 *Chemical Structures of a series of 'reader' molecules synthesized for recognition by tunneling. (a) The first generation reader molecule 4-mercaptobenzoic acid. (b) A water-friendly variant of the original structure, 4-mercaptobenzamide (c) The universal reader or Imidazole reader : 4(5)-(2-mercaptoethyl)-1H-imidazole-2-carboxamide. This molecule is identified capable of forming distinct Hydrogen bonding complexes with all the 4 nucleosides in aqueous medium.*

The STM experiments that followed later, using Imidazole reader functionalization demonstrated the ability to differentiate nucleosides.[27] Thus far, all the STM measurements mentioned in this work were done on gold surface, whereas for this particular study, data from STM experiments with functionalized gold and palladium metal surfaces (tip and substrate) were compared. **Figure 3.6** explains the difference in base differentiation for both the cases. Functionalized Palladium tips and substrate form a more sensitive tunnel junction, leading to more distinguishable signals from individual nucleosides.
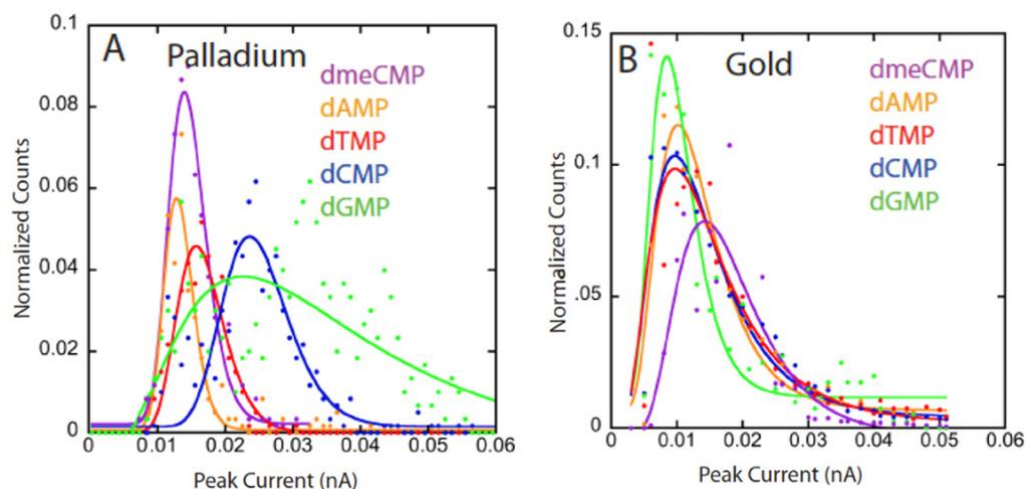
Figure 3.6 *When compared to gold electrodes, data from palladium electrodes appear to be better separated with larger peak currents.*[27]

3.3 IMIDAZOLE FUNCTINONALIZATION ON Pd

It is clear from the previous sections that Palladium substrates functionalized with Imidazole have ultimately proved to be ideal choice for recognition by tunneling. This section provides the experimental protocol for functionalization and characterization. Palladium surface is cleaned either via Hydrogen flame annealing or piranha (Highly oxidizing 3:1 mixture of Sulfuric Acid and Hydrogen Peroxide) cleaning for 30-40s. The solvent for Imidazole dissolution and SAM formation is Ehanol, as is the case of most thilated SAMs. HPLC grade ethanol is used for superior quality of SAM. The Ethanol solution is degassed with Argon in order to eliminate any dissolved oxygen from the solution. Imidazole is then dissolved into this to form 0.1 mM ethanolic solution of Imidazole. The clean Palladium substrate is then left to soak in Imidazole solution for 24

64

hours. The substrate is then rinsed gently with ethanol and and dried under nitrogen prior to its use in experiments.

Ellipsometry, XPS and Wetting Data

Ellipsometric measurements of SAM thicknesses were performed on a Rudolph Research AutoEL ellipsometer with a He-Ne laser light source, λ= 632.8 nm and an incidence angle of 70°. To calculate SAM thickness, a three phase model (ambient – organic film – Palladium) was used. The ellipsometric parameters of the bare Palladium substrate (obtained previously) were entered as set values and the refractive index of the organic film was assumed to be 1.5. This is a common assumption, pre-programmed in the instrument's automatic measurement file. Each sample surface was measured at five detection spots and the average SAM thickness was calculated by the instrument, using in-built algorithm.

Measured length of trapping molecule (Å)	*Experimental thickness of monolayer (Å)*
9.2	*7.5 ± 1.6*

Table 3.1 *Ellipsometry result for Imidazole functionalized Palladium surface*

XPS measurements were performed to examine the chemical state of thiol group sulfur. Measurements were performed on a VG ESCALAB 200i-XL photoelectron

spectrometer. 15keV Al-Kα radiation at 6×10^{-10} mbar base pressure was the source.

First, a wide scan spectra was performed for all the peaks. This is followed by a scan for

S2p, CasaXPS software package was used for the curve fitting of S2p spectra and atomic

concentration calculation. XPS measurements indicated that the sulfur is bound to

palladium .The binding energy of the S2p core level electrons is ~162eV, referenced to

C1s at ~284.80eV.

Element	Atomic Percentage	Found Elemental Ratio	Calculated elemental ratio
S 2p	5.17	1	1
C 1s	16.77	5.2	6
N 1s	12.22	2.4	3

Table 3.2 *XPS data for Imidazole functionalized Palladium surface*

Contact angle goniometry was used to determine the hydrophilicity of the different

Imidazole SAM. Measurements were performed at room temperature with a CAM200

Optical Contact Angle Meter from KSV Instruments Ltd. Prior to measurement, the

syringe needle was rinsed and filled with distilled water. Static contact angle values were

recorded on three sites of each sample surface.   Pictures of the droplet profile were taken

during the process by a horizontally mounted CCD camera. The program software was

used to perform a numerical curve fit of the obtained droplet profile and this determined

the contact angle.

Figure 3.7 *The optical image of a water droplet on Imidazole functionalized palladium surface.*

Water contact angle of functionalized Pd substrate (deg)	*Water contact angle of non-functionalized Pd substrate (deg)*
34 ± 3	*6 ± 2*

Table 3.*3* *Wettability data for Imidazole functionalized Palladium surface*

3.4 REFERENCES

1.   Whitesides, G. M. & Grzybowski, B. Self-Assembly at All Scales. *Science* **295,** 2418–2421 (2002).

2.   Rechtsman, M. C., Stillinger, F. H. & Torquato, S. Optimized Interactions for Targeted Self-Assembly: Application to a Honeycomb Lattice. *Phys. Rev. Lett.* **95,** 228301 (2005).

3.   De Feyter, S. & De Schryver, F. C. Self-Assembly at the Liquid/Solid Interface: STM Reveals. *J. Phys. Chem. B* **109,** 4290–4302 (2005).

4.   Hemsley, A. R., Collinson, M. E., Kovach, W. L., Vincent, B. & Williams, T. The Role of Self-Assembly in Biological Systems: Evidence from Iridescent Colloidal Sporopollenin in Selaginella Megaspore Walls. *Phil. Trans. R. Soc. Lond. B* **345,** 163–173 (1994).

5.   MacGillivray, L. R., Subramanian, S. & Zaworotko, M. J. Interwoven two-and three-dimensional coordination polymers through self-assembly of CuI cations with linear bidentate ligands. *J. Chem. Soc., Chem. Commun.* 1325–1326 (1994).

6.   Jenekhe, S. A. & Chen, X. L. Self-Assembly of Ordered Microporous Materials from Rod-Coil Block Copolymers. *Science* **283,** 372–375 (1999).

7.   Aoyama, Y. *et al.* Crystal Engineering of Stacked Aromatic Columns. Three-Dimensional Control of the Alignment of Orthogonal Aromatic Triads and Guest Quinones via Self-Assembly of Hydrogen-Bonded Networks. *J. Am. Chem. Soc.* **118,** 5562–5571 (1996).

8.   Kato, T. Self-Assembly of Phase-Segregated Liquid Crystal Structures. *Science* **295,** 2414–2418 (2002).

9.   Fendler, J. H. Chemical Self-assembly for Electronic Applications. *Chem. Mater.* **13,** 3196–3210 (2001).

10.   Chen, J., Reed, M. A., Rawlett, A. M. & Tour, J. M. Large On-Off Ratios and Negative Differential Resistance in a Molecular Electronic Device. *Science* **286,** 1550–1552 (1999).

11.   Kim, K. & Matzger, A. J. Inequivalent Molecules in a Two-Dimensional Crystal. *J. Am. Chem. Soc.* **124,** 8772–8773 (2002).

12.   Plass, K. E., Kim, K. & Matzger, A. J. Two-Dimensional Crystallization: Self-Assembly, Pseudopolymorphism, and Symmetry-Independent Molecules. *J. Am. Chem. Soc.* **126,** 9042–9053 (2004).

13.   Venkataraman, B., Flynn, G. W., Wilbur, J. L., Folkers, J. P. & Whitesides, G. M. Differentiating Functional Groups with the Scanning Tunneling Microscope. *J. Phys. Chem.* **99,** 8684–8689 (1995).

14.   Wintgens, D., Yablon, D. G. & Flynn, G. W. Packing of HO(CH2)14COOH and HO(CH2)15COOH on Graphite at the Liquid−Solid Interface Observed by Scanning Tunneling Microscopy: Methylene Unit Direction of Self-Assembly Structures. *J. Phys. Chem. B* **107,** 173–179 (2003).

15. Wei, Y., Kannappan, K., Flynn, G. W. & Zimmt, M. B. Scanning Tunneling Microscopy of Prochiral Anthracene Derivatives on Graphite: Chain Length Effects on Monolayer Morphology. *J. Am. Chem. Soc.* **126,** 5318–5322 (2004).

16. Kim, K., Plass, K. E. & Matzger, A. J. Conformational Pseudopolymorphism and Orientational Disorder in Two-Dimensional Alkyl Carbamate Crystals. *Langmuir* **21,** 647–655 (2005).

17. Rabe, J. P. & Buchholz, S. Direct observation of molecular structure and dynamics at the interface between a solid wall and an organic solution by scanning tunneling microscopy. *Phys. Rev. Lett.* **66,** 2096–2099 (1991).

18. Nuzzo, R. G., Zegarski, B. R. & Dubois, L. H. Fundamental studies of the chemisorption of organosulfur compounds on gold(111). Implications for molecular self-assembly on gold surfaces. *J. Am. Chem. Soc.* **109,** 733–740 (1987).

19. Bain, C. D. *et al.* Formation of monolayer films by the spontaneous assembly of organic thiols from solution onto gold. *J. Am. Chem. Soc.* **111,** 321–335 (1989).

20. Vericat, C., Vela, M. E., Benitez, G., Carro, P. & Salvarezza, R. C. Self-assembled monolayers of thiols and dithiols on gold: new challenges for a well-known system. *Chemical Society Reviews* **39,** 1805 (2010).

21. Zwolak, M. & Di Ventra, M. Colloquium: Physical approaches to DNA sequencing and detection. *Rev. Mod. Phys.* **80,** 141–165 (2008).

22. Lindsay, S. *Introduction to Nanoscience*. (Oxford University Press, USA, 2009).

23. Lindsay, S. *et al.* Recognition tunneling. *Nanotechnology* **21,** 262001 (2010).

24. Chang, S. *et al.* Electronic Signatures of all Four DNA Nucleosides in a Tunneling Gap. *Nano Lett.* **10,** 1070–1075 (2010).

25. Huang, S. *et al.* Identifying single bases in a DNA oligomer with electron tunnelling. *Nat Nano* **5,** 868–873 (2010).

26. Liang, F., Li, S., Lindsay, S. & Zhang, P. Synthesis, Physicochemical Properties, and Hydrogen Bonding of 4(5)-Substituted 1-H-Imidazole-2-carboxamide, a Potential Universal Reader for DNA Sequencing by Recognition Tunneling. *Chemistry – A European Journal* **18,** 5998–6007 (2012).

27. Chang, S. *et al.* Palladium electrodes for molecular tunnel junctions. *Nanotechnology* **23,** 425202 (2012).

4. FUNCTIONALIZED NANOPORES FOR DNA ANALYSIS

 Nanopores are unique not only because they facilitate the exploration of new physics at the nanometer scale, but also due to the expanding progress in fabrication techniques that make it possible to dictate precision in geometry, dimensions and chemistry on that scale. This chapter first elucidates the major techniques involved in fabricating functionalized pores. This is followed by a description of the single molecule translocation experiments and their implications.

 4.1 PALLADIUM ELECTRODE FABRICATION

 4.1.1 Electron Beam Lithography

Any sort of semiconductor device fabrication usually mandates patterning of selective areas of samples to accommodate for standard processing steps such as etching, deposition etc. The technique of creating patterns that distinguish or "mask off" selected regions for further processing is known as "lithography".   Electron Beam Lithography is a process that uses a finely focused electron beam to write patterns in thin films of electron sensitive material. When a finely focused beam of electrons is accelerated at a resist surface, very high resolution patterns can be produced due to the fact that the wavelength of electrons are smaller than that of Ultra violet photons (by 3 orders of magnitude).[1] The basic steps involved in any lithographic process are illustrated in **Figure 4.1.** First the semiconductor surface is cleaned to remove any contaminants that may result in poor adhesion of the e-beam resist film. The e-beam resist is mostly an organic polymer that is
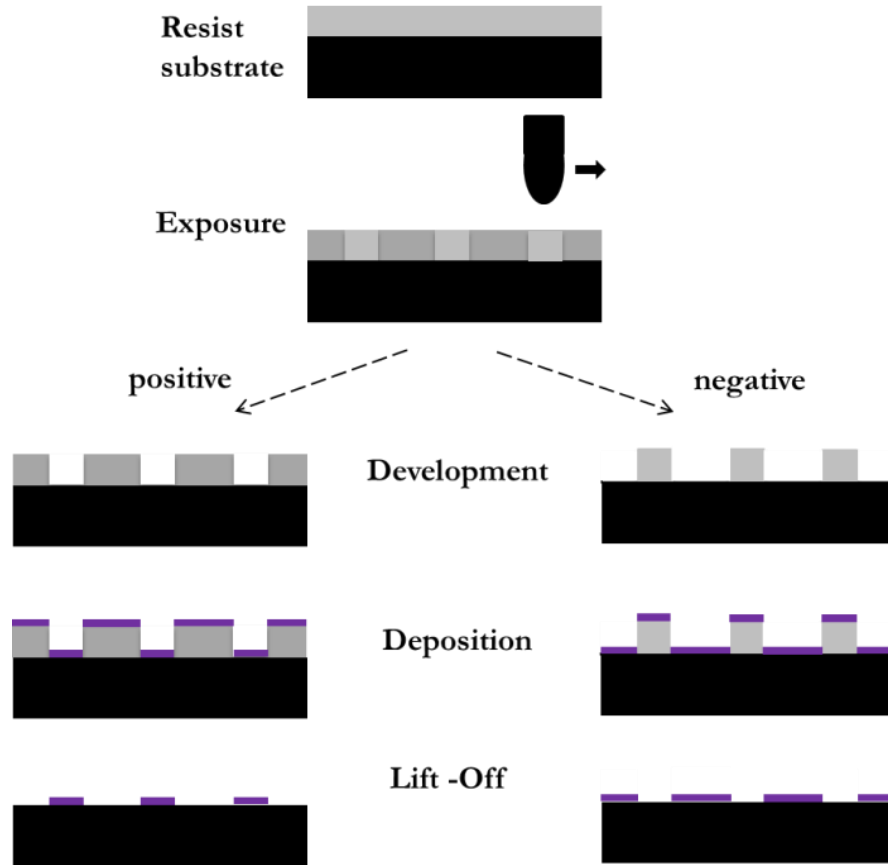
Figure 4.1 *Schematic of Lithography. A schematic illustrating sequence of steps required to pattern a substrate by e-beam exposure of positive and negative resist.*

'sensitive' to the incident e-beam and can 'resist' chemical attack of the underlying substrate. The resist is deposited via by spin-coating a solution of the polymer dissolved in an appropriate solvent. (This step is sometimes preceded by spin-coating an adhesion promoter to enhance the adhesion of the resist.) The substrate is then baked at a temperature above the boiling point of the solvent so as to evaporate excess solvent from the film and thermally anneal the stress built up in the film during spin coating.

71

During exposure, a computer generated pattern file directs a tightly focused electron beam to desired locations on the resist surface. The pattern is discretized into a series of pixels and the beam is deflected, scanned, turned off and on as per the pixilated pattern. Irradiated area of resist undergoes chain scission. Chain scission can cause fragmentation of high weight polymers into smaller chains or induce crosslinking by generating radicals within the resist. This causes lowering of molecular weight distribution in the former case and increasing in the latter. The substrate is then immersed in a developer solution. Depending on whether the exposed regions are rinsed away (former) or remain (the latter), the lithographic process is called 'positive' or 'negative' respectively.

Typically this step is followed by metal deposition after which the substrate is immersed in a solvent. Metal deposited on the substrate remains while the metal on the damaged resist is rinsed away along with the resist. The result is high resolution metal pattern on the substrate.

4.1.2 Fabrication Protocol

The starting substrates used for fabrication of nanopores are standard TEM nitride membrane windows purchased from Norcada inc. These are 3 x 3 mm^2 silicon chips comprising of 200 μm thickness Silicon frame with a central window where a thin Silicon Nitride membrane is suspended (see **Figure 4.2**).
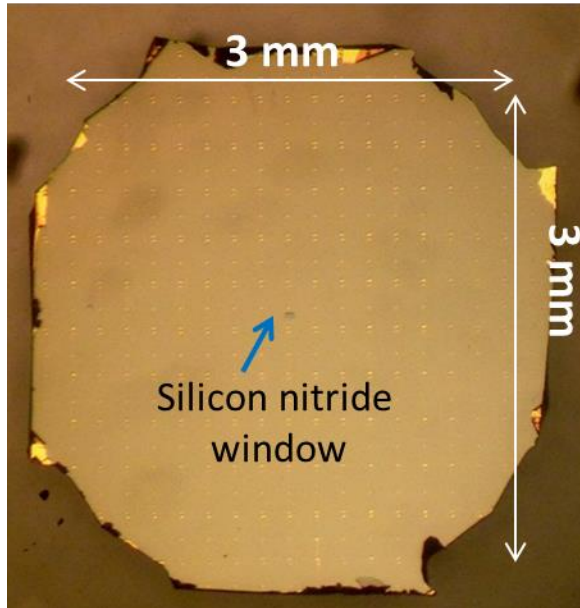
Figure 4.2 *The optical image of the SiN membrane chip with grid of markers*

The Silicon Nitride membranes are low stress and robust. On the central free standing region of SiliconNitride membranes, a restricted area pattern of Palladium needs to be deposited. In order to locate and lay down Palladium electrode, the electron beam lithography technique is used. First an alphanumerical grid of location reference Au/Cr (35nm/5nm) markers are laid onto the chip. This grid is used to locate the position of the central membrane area accurately. AUTOCAD is used to generate pattern of 10μm x10μm square on the membrane. The chip is then subjected to the fabrication steps illustrated in **Figure 4.3**.

Standard Silicon Nitride
membrane

Spin Coat PMMA Resist

Expose 10umx10um area
Using Ebeam Lithography

Etch Silicon Nitride using
Reactive ion Etching

Deposit Pd , Lift off the resist
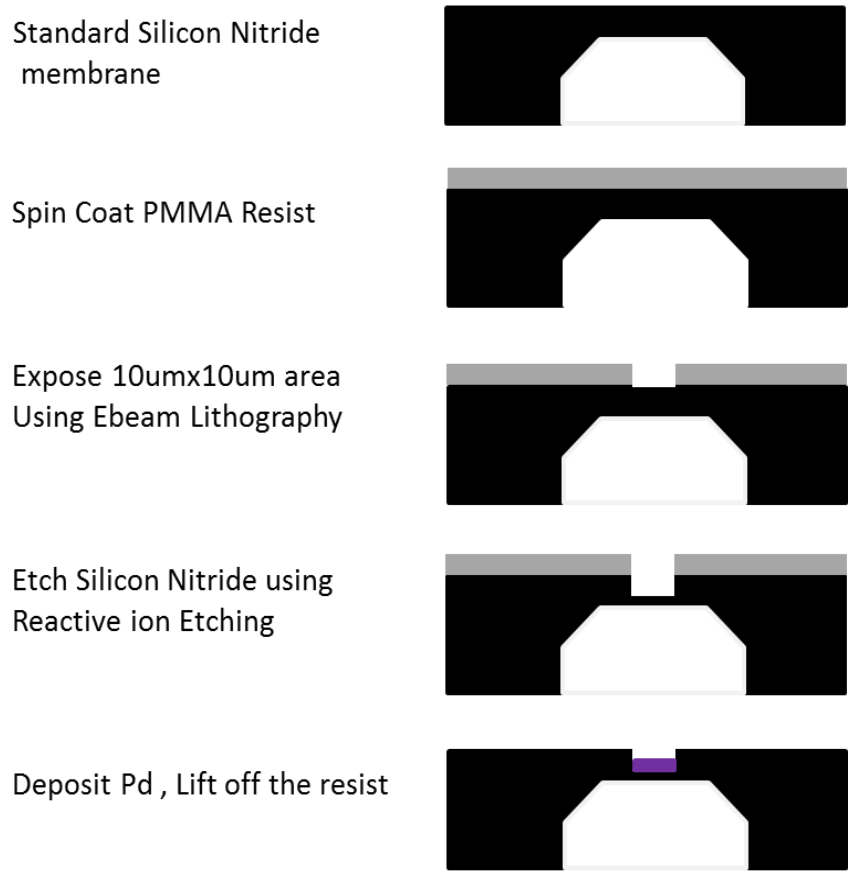
Figure 4.3 *The schematic illustrates the fabrication steps leading to the deposition of*

Palladium layer

 4.2 NANOPORE FABRICATION

4.2.1 Methods of Nanopore Synthesis

Single nanopores in synthetic membranes can be created using four basic methods: Oxide

reflow, ion beam sculpting, the track-etch method and electron beam based sputtering.[2]

Focused ion beam (FIB) milling and laser ablation are some other methods that can

produce sub100nm pore diameters.[3–5]

74

Electron Beam Induced Oxide Reflow

The oxide reflow technique is a two- step process of drilling nanopore. First, electron beam lithography is used to pattern 40-100nm holes in silicon membranes. Then, using TEM[6] high energy electron beam, the oxide surface surrounding the original pore is fluidized. In substrates where the diameter of the pore is lesser than thickness of the membrane, the fluidized oxide reflows causing the pore to shrink to less than 10nm range. The shrinking phenomenon could be due to the build-up of hydrocarbon layer in the nanopore during the electron beam irradiation.[7] The main limitation of silicon oxide pores formed by thermal oxidation is the high level of compressive stress and membrane –buckling observed in these membranes, causing them to rupture frequently during DNA translocation experiments.[8] This implies the need for mechanically stable, low stress membranes for nanopore formation.

Ion Beam Sculpting

The ion-beam sculpting process first developed by Li et al uses an energetic beam of Ar+ ions to form nanopores with dimensions as low as 1.5 nm in thin Si3N4 membranes.[9] When a 3 keV Ar+ ion beam is rastered continuously over a Si3N4 sample at room temperature, atoms get diffused into the pore region causing the nanopore to shrink. The flow of matter to the developing nanopore cite showed temperature dependence with a transition between pore opening and closing being consistently observed at ~5°C, under

75

the ion-beam conditions used. Pore expansion was attributed to ion 18 sputter erosion at the pore edge, the dominant mechanism at low temperature and high ion flux Pore closure was accredited to the formation of a stressed viscous surface layer at the lip of the nanopore. The reduced viscosity and/or enhanced stress owing to implantation or surface tension effects cause this layer to relax, thereby filling the nanopore. Feedback control was used to precisely sculpt nanopores of various sizes using this process.

Track-Etch Method

In this method, a high energy beam of ions or nuclear fission fragments from a MeV accelerator is made to bombard a thin sheet of polymer material.[10–12] The irradiated polymer sheet is then placed between two electrolyte chambers. One chamber is filled with a chemical etchant (such as NaOCl) while the other is filled with a stopping agent (KI). At high pH (pH=13) and elevated temperatures (~50℃), etching of the irradiated track begins from one side, and continues until the etching is through and a pore is formed. At this point the OCl- oxidize to Cl- ions thereby terminating the etch process automatically. The pores created by this process have diameter less than 10nm.

Electron Beam Induced Sputtering

In this method, a focused convergent electron beam with sufficiently high current density is used to sputter nanometer-sized pores in thin oxide or nitride membranes of thickness less than 60nm. Electron Beam induced sputtering is increasingly being adopted as the

drilling method of choice because it provides a reliable, fast and direct way to make nanopores.

High-resolution TEM has been used to explain nanopore formation kinetics in Si3N4 as a balance between two competing processes: (a) material sputtering and (b) surface-tension induced shrinking. In the same study, 4 to 8 nm in diameter nanopores were directly drilled using a JEOL 2010F field emission TEM with an accelerating voltage of 200 keV and a beam current density of $10^8 - 10^9$ e nm^{-2}. [13]It was also demonstrated that by slightly defocusing the e-beam, (corresponding to ~10^6 e nm^{-2} intensity), the drilled pores could be contracted. TEM tomography of these solid-state nanopores revealed that the sidewalls of the pores were angled (65° to the horizontal), attributed to the intensity distribution of the e-beam around its focal point. After drilling, these pores formed an 'hourglass' structure with pore width being represented by the width of the narrowest constriction.[13,14]

Reports from other structural studies of nanopores drilled using this indicate that the shape of TEM drilled nanopores is typically double-coned with cone angles varying from 10°[15] in ultrathin silicon nitride membranes up 45° in composite SiO2/SiN/SiO2 membranes.[16]

4.2.2 TEM drilling Protocol

In this work, all nanopores have been fabricated by electron beam sputtering in the JEOL 2010F Transmission electron microscope. The drilling procedure is described briefly. The

field emitting source is set at to 200kV accelerating voltage. A test sample is first loaded and the objective lens is stigmated and focused onto the surface. The condenser aperture is introduced and the eucentric height is established by adjusting the height of the sample until the diffraction spot is eliminated. The surface is imaged at this point to check for stability. If the sample is found to be drifting,, it is left to stabilize until there is minimal drift. At this point, the beam is focused to a tight spot under the highest magnification settings and a nanopore is drilled through the sample surface. The beam current and energy settings can be adjusted so as to drill pore gradually for a time of 30-45 s. The formation of the nanopore is indicated by the accompanying increase in electron flux crossing the sample. As soon as the pore is formed, the condenser is spread and an image of the fresh pore is captured via CCD camera. The beam is blanked immediately and the sample is taken out of the TEM. The actual Pd membrane is loaded on to the TEM and a nanopore is then drilled under the same
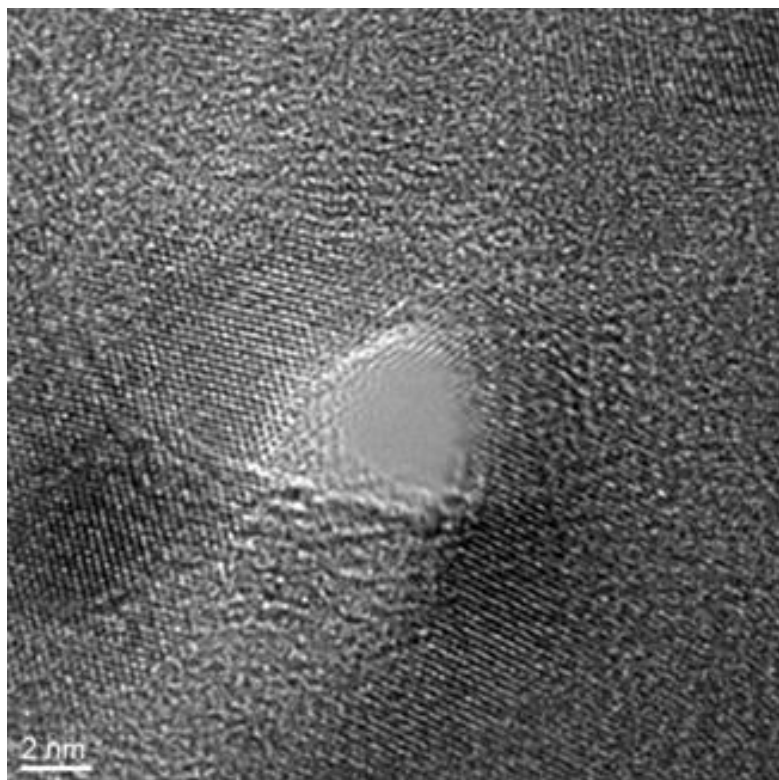
. **Figure 4.4** *TEM Image of sub 5nm nanopore.*

conditions. It has been observed that for membranes thinner than 20 nm successive

imaging can introduce defects of the order of less than 1nm.While these defects do not

interfere with DNA translocation through the device, they do contribute to a higher

background current that may be undesirable. In order to circumvent this problem,

imaging is mostly performed on the test sample to get an idea of the pore dimensions

upto a point when the alignment, drill time settings repeatedly yield same pores of

consistent diameter. The actual membranes are then loaded onto the TEM and drilled

without changing any settings.

The size estimation is confirmed by conductance measurements done before performing DNA translocation experiments.

The nanopores are stored in 50% IPA 50% water solution in order to avoid shrinkage and clogging.It has been our observation that piranha cleaning of the nanopores within 5-6 hours of drilling prolongs the shelf life of the pore.

4.3 EXPERIMENTAL SET-UP

4.3.1 Flow Cell Assembly

In order to perform the single molecule studies described here, the experimental set up necessitates that the nanopore be the bridge between two otherwise isolated reservoirs of electrolytes. Barring the access via nanopore, electrolytes need to be completely isolated from each other in order to mitigate all scope for leakage current. At the same time, minimal macroscopic pressure on the chip, intended originally to prevent leakage path, could by itself damage the suspended membrane of the chip that is just a few nm thin. To balance the pressure and maintain a leak-free channel, polydimethylsiloxane (PDMS) is used.

PDMS is an organo-silicon polymer with chemical formula $(H_3C)_3SiO[Si(CH_3)_2O]_nSi(CH_3)_3$. When subjected to crosslinking (**Figure 4.3**), the liquid PDMS can be modified into a solid with hydrophobic surface.[17]
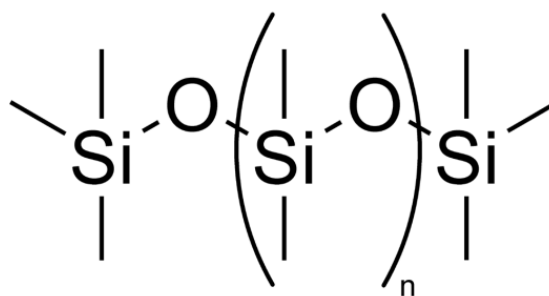
Figure 4.5 *Cross linking in polydimethylsiloxane (PDMS)*

Further, the amount of cross-linking reagent added can be varied to change the hardness and rigidity of the resulting solid. Fluid compatibility studies in PDMS microchannels show that water flow through the channels is non-destructive and causes no swelling.[18] Due to these attractive properties, PDMS has been widely used for making microfluidic devices.

PDMS is popular in microfluidic devices for its inertness, tunable rigidity, transparency and easy wettability. Thus, the nanopore chip encapsulated by PDMS on either sides is sandwiched between reservoirs of 1M KCl+PB salt buffer solutions. Microfluidic channels are drilled through the PDMS to provide access for the solutions to the nanopore area. Ag/AgCl electrodes, dipped in the solutions are connected to Axon Axopatch 200B patch clamp amplifier (**Figure 4.5**).
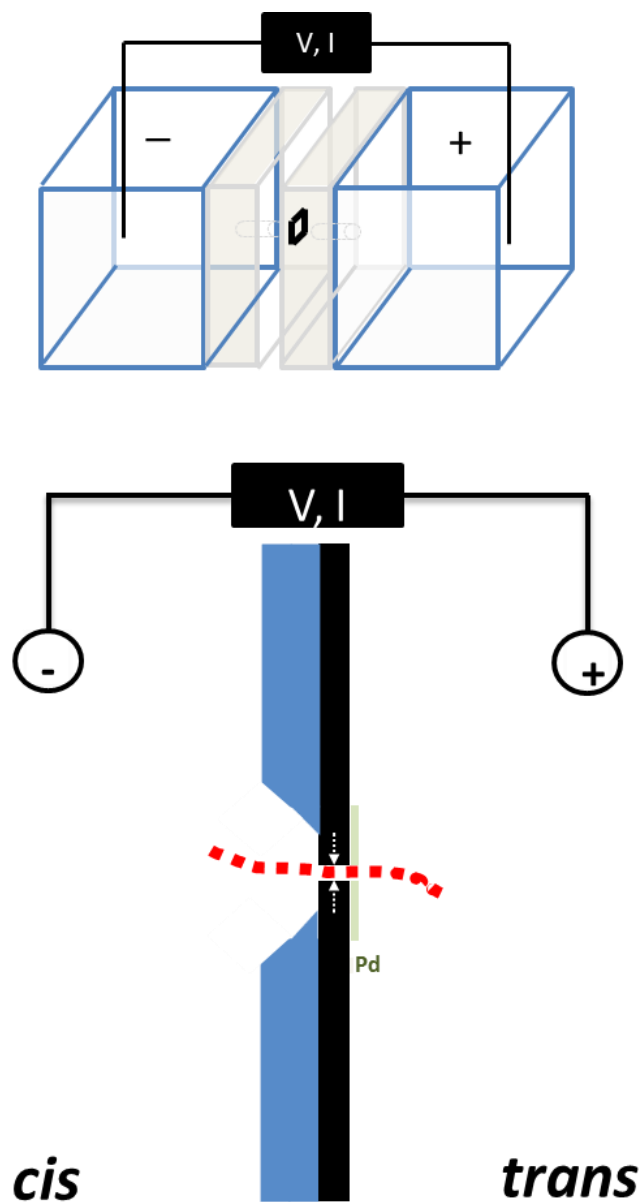
Figure 4.6 *The PDMS flow-cell assembly*

The PDMS based flow cell has advantages of optical visibility during assembly and experiment, convenient access to change analytes without applying pressure on the chip and low access resistance due to elimination of long flow conduits.

However, the lowest analyte volume that can be analyzed in this set up is limited to 500 uL. Reducing this volume further would accommodate for minimizing the volume of expensive analytes. In view of this need an alternative flow cell made of PEEK has been designed and is ready for use in future experiments. The design and extended purpose of this flowcell will be elucidated in the next chapter in the context of future work.

4.3.2 Wetting of Nanopore

One of the most common and perhaps tricky issues that experimentalists across the nanofluidics research community face is the problem of nanopore wetting or rather incomplete wetting. There are two basic reasons for this. Firstly, a nanopore chip undergoes multiple fabrication steps spanning days of sample preparation before it is mounted for the experiment. Hence it is natural to expect that the surface of the chip maybe contaminated with hydrocarbons. Secondly, the set up in these experiments involves interfacing nanometer scale channels with comparatively macroscopic channels, such that practical access and manipulation is possible only up to macroscopic limit. This could lead to trapped air bubbles and possibility of partial wetting.

In order circumvent these issues, cleaning by means of plasma or piranha is usually recommended. For the devices used in this work, piranha cleaning step has worked well in favor of establishing good pore wettability. In the case of functionalized

chips, the piranha cleaning is done before bringing the chip in contact with Imidazole reader molecules. In addition to improving wettability, piranha treatment removed surface contamination effecting in formation of more uniform SAM along the walls of the nanopore.

Apart from the nanopore surface, the PDMS and the solution reservoirs are ultra-sonicated for 20 minutes in Isopropanol Water mixture (1:1) in order to expel other surface contamination. Degassing the salt buffers also eliminates the chance of air bubbles in the fluidic channels.

4.4 NANOPORE I-V MEASUREMENTS

The successful drilling of a nanopore can be checked by perfomring an ionic flow measurement using the nanopore. When 1M KCl + PB buffer is introduced to the nanopore flow cell, standard IV curve is obtained by measuring current at different bias. The I-V curves for different salt concentrations is plotted in the figure and it is observed that linear behavior is maintained in high as well as low salt regime. The conductance vs concentration is plotted in **Figure 4.7.** Upon addition of DNA, a jump in conductance is typically observed. This is shown in **Figure 4.8**, for the case of a functionalized as well as unfunctionalized nanopore
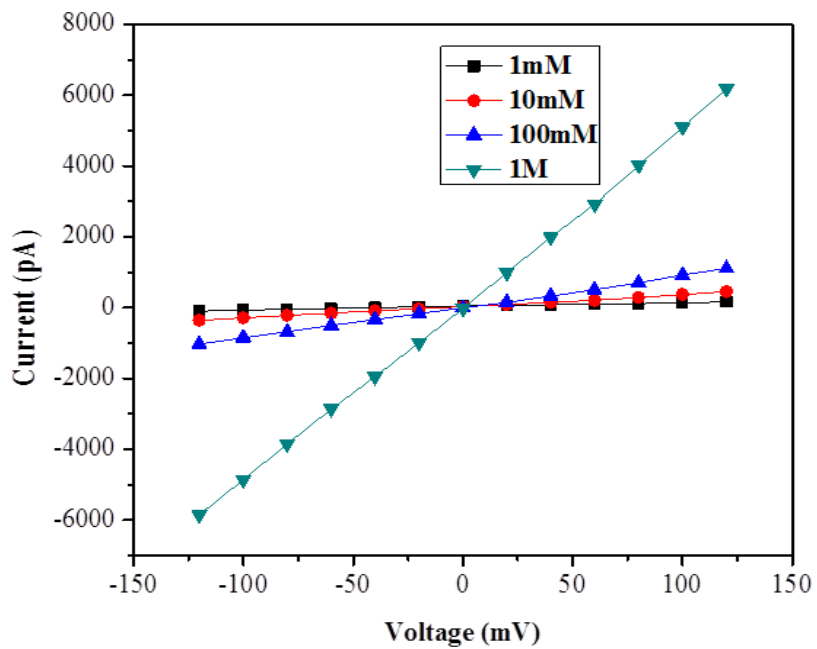
(a)
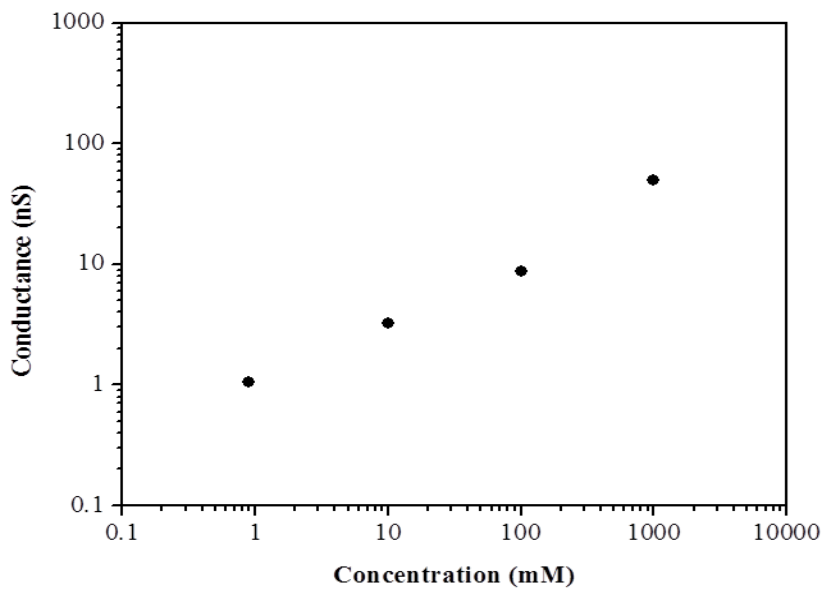
(b)

Figure 4.7 *(a) I-V curves showing linear behavior from 1mM upto 1M concentration. (b)*

Plot of conductance vs concentration
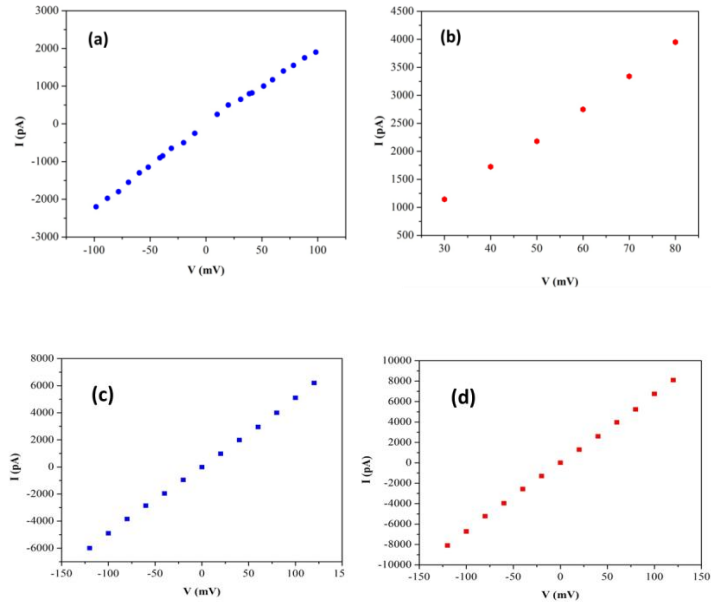
Figure 4.8 *(a) Current vs. Voltage characteristics for an Imidazole functionalized nanopore before adding ssDNA and (b) after adding ssDNA. On adding DNA, the conductance for this pore increases from 21.1 nS to 55.5 nS (c) Current vs. Voltage characteristics for an plain palladium nanopore before adding ssDNA and (b) after adding ssDNA. The increase in conductance for this case is from 49.9nS to 66.76 nS.*

4.4.1 Resistive Sensing Technique

Resistive Sensing technique is the fundamental principle behind nanopore detection, irrespective of whether the pores are naturally occurring, biological ion channels or synthetic nanopores. **Figure 4.9** obtained with permission from a recent review on nanopores[19] shows the variety of nanopores being explored to date. The principle can applied to sense a rage of particle size – from a few nm long DNA fragments upto micron size cells (as used in Coulter Counters).[20]
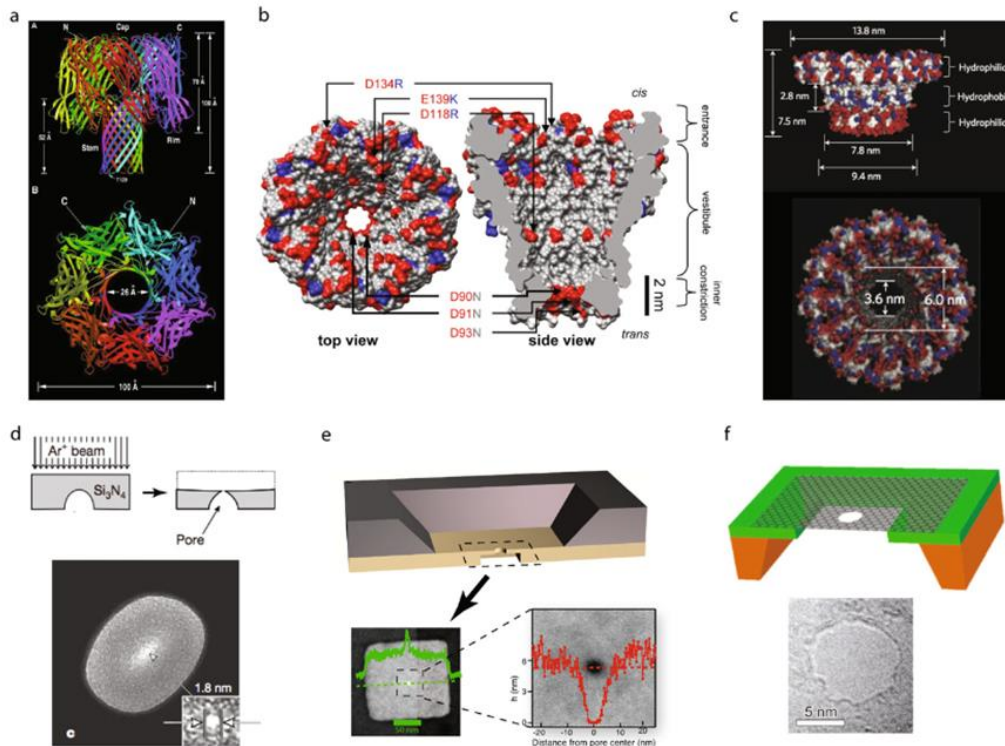
Figure 4.9 *Some examples of biological and synthetic nanopores. (a) The toxin α -
hemolysin secreted by Staphylococcus aureus [21] (b) MspA from Mycobacterium
smegmatis.[22] (c) Engineered phi29 viral packaging motor[23] . (d) Ion-sculpted pores in
silicon nitride membrane [9] (e) Sub-10 nm thick solid-state pores generated by dry etching
a selected area of a silicon nitride membrane and electron-beam pore drilling [24] .(f)
Pores in a suspended single-layer graphene membrane [25] . Images were obtained with
permission.*

To understand the phenomenon, the physical properties of the analytes need to be compared (See **Table 4.1**).[19]

Species	R_H(nm)	D ($\mu m^2 s^{-1}$)	Typical Concentration(M)
Red Blood Cell	3500	0.06	$\sim 10^{-14}$
20-bp DNA fragment	3	140	$10^{-9} - 10^{-6}$
K$^+$, Cl$^-$	0.14	1600	0.1-1

Table 4.1 Estimated hydrodynamic radii and Stokes diffusion coefficients of aqueous species used in Coulter counters and nanopore sensors. Typical experimental concentrations are also listed.[19]

From the list of hydrodynamic radii and diffusion constants in Table 4.1, it is clear that the ions involved in pore-based sensing are *smaller, faster and more concentrated* than the analytes they are used for detecting. This observation leads to three important implications. Firstly, for every analyte passing the pore, greater number of ions should be able to pass through the pore. Secondly, In order to sense the analyte, the pore needs to have a diameter greater than the hydrodynamic radius of the analyte. Thirdly, due to the fact that the ion happens to be the smallest hydrodynamic particle (radius 0.1nm), ionic flow should be sufficient to differentiate two analytes that differ in cross section by the ion's hydrodynamic radius. Most importantly this implies that the detection of every single analyte involves the passage of many ions through the nanopore.

4.4.2 Ionic and Biomolecular transport

When Voltage V is applied across a cylindrical nanopore, the ionic current through the pore is approximated in high ionic strength solutions (>100mM) by

$$I_0 = V([n_+ \mu_+ + n_- \mu_-]e)\left(\frac{4h}{\pi d^2} + \frac{1}{d}\right)^{-1} + \frac{V \mu_\otimes \pi d \sigma}{h}$$

$$\underbrace{}_{\substack{Solution \\ Conductivity}} \quad \underbrace{}_{\substack{Geometric \\ term}}\underbrace{}_{\substack{Access \\ resistance}} \quad \underbrace{}_{\substack{Electroosmotic \\ term}}$$

Where I_0 is the ionic current, n is the number density of the species, μ is the electrophoretic mobility of the species and e is the elementary charge. The last term is required to explain ion transport through highly charged pore surfaces, where μ is the solution mobility of the counterion adsorbed on the charged pore and σ is the surface charge density of the pore(opposite to the charge of the counterion)[16] This equation combines the effect of access resistance to the earlier transport studies.[14,16,25] Contribution of access resistance becomes more significant as the membrane thickness approaches zero limit ($h \rightarrow 0$).

When biomolecules such as DNA are introduced in a nanopore experiment, it is interesting to understand the mechanism behind how long polymers find their way through a very narrow pore. When the DNA concentration is very low, the interactions between the DNA molecules are very low. In this regime, the process of capture is governed by classic arrival time Poisson process. Thus the normalized probability of arrival time-delay is given by:

89

$$P_{\delta t=t}(t) = e^{-R_c t}$$

Where δt is the measured time-delay between successive events and R_c is the mean capture rate. This is mostly true, except for situations where the mean wait time $1/R_c$ is comparable to the transport time, the concentration of the analyte is high enough that analyte molecules interact with each other or that the analyte solution is not mixed uniformly.

In solid state nanopores, capture rate of the molecule is another important parameter. The dependence of capture rate on applied bias for the case of ssDNA in solid state nanopores has been studied The voltage profile outside the pore mouth is known to decay with radial distance r from the pore as follows.[26,27]

$$V(r) = \frac{d^2}{8\,h\,r}\Delta V$$

Where d is the diameter of the pore, h the pore height, and ΔV is the applied voltage. When the negatively charged DNA approaches the vicinity of the pore via diffusion, the diffusion is biased by electric field. Thus, the biased diffusion is a function of the electric field as well as the diffusion, causing the radial distance r to be dependent on the DNA length, and will be dependent on the total charge as well as the diffusion coefficient of the DNA. So, in case of a diffusion –limited process, the radius of capture is linearly dependent on the voltage.

Biological pores are known to have an exponential dependence of capture rate on the voltage. This clearly indicates that the capture is not diffusion limited – meaning, every

molecule that diffuses towards the pore may not be captured.[19] Or, that a fraction of molecules that approach the vicinity of the pore, are rejected. Such a behavior may be attributed to the entropic barrier inherent in a polymer threading into the confines of the pore. The entropic barrier can however be reduced by increasing the applied voltage. Hence beyond some threshold voltage, the entropic barrier could be overcome, and the capture may become diffusion-limited. At that critical voltage, the capture rate switches from exponential dependence onto a linear dependence on V.

4.5 DNA TRANSLOCATION EXPERIMENTS

4.5.1 Effect of Functionalization

After the flow cell is assembled under optical microscope and wetted, the entire set up is placed inside a faraday cage. Current Voltage measurements are made using an Axon Axopatch 200B patch clamp amplifier. The amplifier applies a constant potential across the pore and measures the current necessary to maintain the potential drop. The current signal is captured in real time using LABVIEW software. At the outset of the experiment, the baseline current values are noted for various voltages so as to establish the open pore conductance. Once this is established, the analyte molecules are introduced in the *cis* side of device. Since the analytes here are mainly negatively charged DNA, they translocate through the nanopore towards the positively charged electrode on the *trans* side. Each single molecule crossing is detected by an accompanying transient decrease in the ionic current. The width of the pulse represents the duration of the translocation event.

We first study the effect of Imidazole functionalization on DNA translocation. First, 63 nt ssDNA is introduced into Pd nanopore that does not have any Imidazole on its surface. In the presence of electric field, the ssDNA molecules translocate through the nanopore yielding current spike signals. The data is collected, and the same chip is cleaned and functionalized with Imidazole. Now, upon introducing the 63nt ssDNA (5'- CCT CGC ATG ACT CAA CTG CCT GGT GAT ACG AGG ATG GGC ATG CTC TTC CCG ACG GTA TTG GAC-3' from IDT) it is observed that the current spikes are of relatively longer duration. After collecting data, the chip is cleaned and Pd is etched away. The resulting silicon nitride nanopore is once again set up to analyze the translocations of 63mer. **Figure 4.10** represents sample spike from three sets of data gathered during the experiment. From examining the spike duration, it is evident that the presence of Imidazole reader causes the translocation to slow down. The same analyte molecule now takes a longer time causing a longer blockade in the ionic current and thus a longer event. A statistical analysis of the events shows that the median event-duration t_M <0.6 ms for the Pd pore, 12 ms for the functionalized pore and <0.2 ms for the stripped pore.
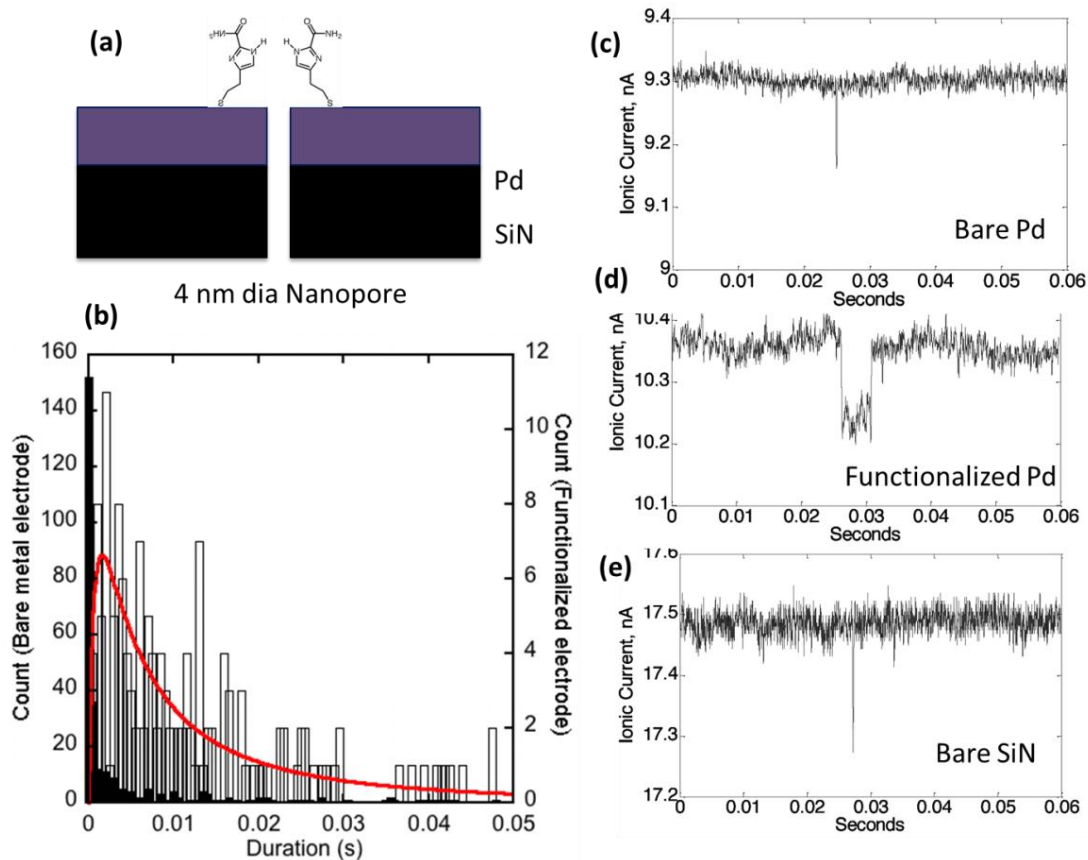
Figure 4.10 *(a) Illustration of 4nm diameter Palladium coated silicon nitride nanopore with functionalization. (b) Histogram comparing duration of events with and without functionalization. (c), (d) and (e) show sample spikes for Palladium, Imidazole functionalized Palladium and Bare Silicon nitride nanopores respectively.*

4.5.2 Positive control with 1-Octanethiol

Imidazole functionalized substrates and tips have already established base resolution capabilities, as indicated from previous chapter disucssions. Also, from 4.5.2 experimental results indicate that Imidazole functionalization slows the translocation of DNA molecules through Palladium nanopores. Hence, the question that arises is – whether the the slowing down of translocations is because of the Hydrogen bond mediated interactions of the DNA with the Imidazole reader or whether it is due to the steric hindrance due to the mere presence of the reader molecules.

In order to investigate this underlying mechanism of slowing down, the following experiment was conducted. 1-Octanethiol is chosen as a positive control. From the structure of the molecule (**Figure 4.11**), it is known that 1Octanethiol is a thiol terminated alkane chain which lacks any H bonding capacity, when tethered to metal.
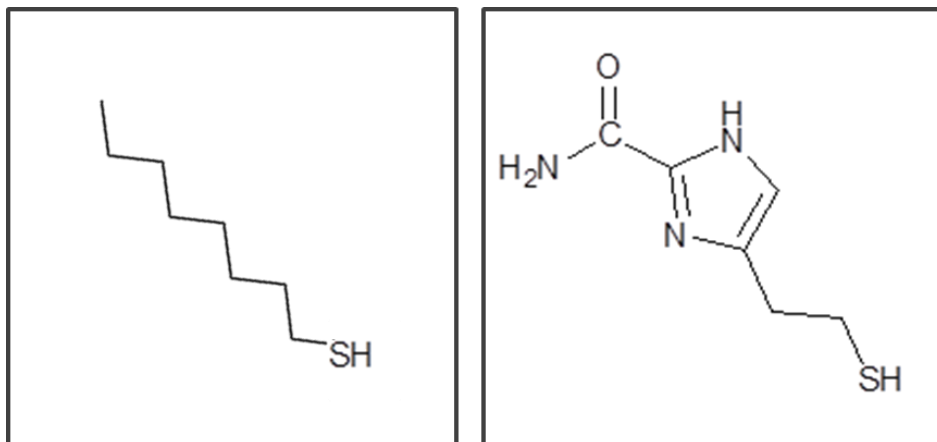
Figure 4.11 *Molecular structure of 1-Octanethiol (left) and Imidazole (right).*

Hence, two identical Palladium nanopores were fabricated. One of them was functionalized with 1-Octane thiol and the other, with Imidazole reader. After a 24 hour gap, both nanopores were set up to translocate 120nt ss DNA (5'- CCT CGC ATG ACT CAA CTG CCT GGT GAT ACG AGG ATG GGC ATG CTC TTC CCG ACG GTA TTG GAC CCT CGC ATG ACT CAA CTG CCT GGT GAT ACG AGG ATG GGC ATG CTC TTC CCG ACG GTA -3' from IBA Lifesciences). From the data collected, it is seen that the translocation events are more prolonged (median translocation time 13.9 ms) in the case of Imidazole functionalized pore, whereas in the Octanethiol functionalized pore, they translocate very quickly (median translocation time 0.5 ms).

Figure 4.12 displays a sample trace from both the experiments and the spike shape is indicative of the difference in translocation time. When plotted in amplitude vs distance graph, the events from the two pores are very well separated. From this, it is evident that H bonding moieties of Imidazole that cause the molecule to translocate significantly than they would in a non H-bond forming functionalized pore.
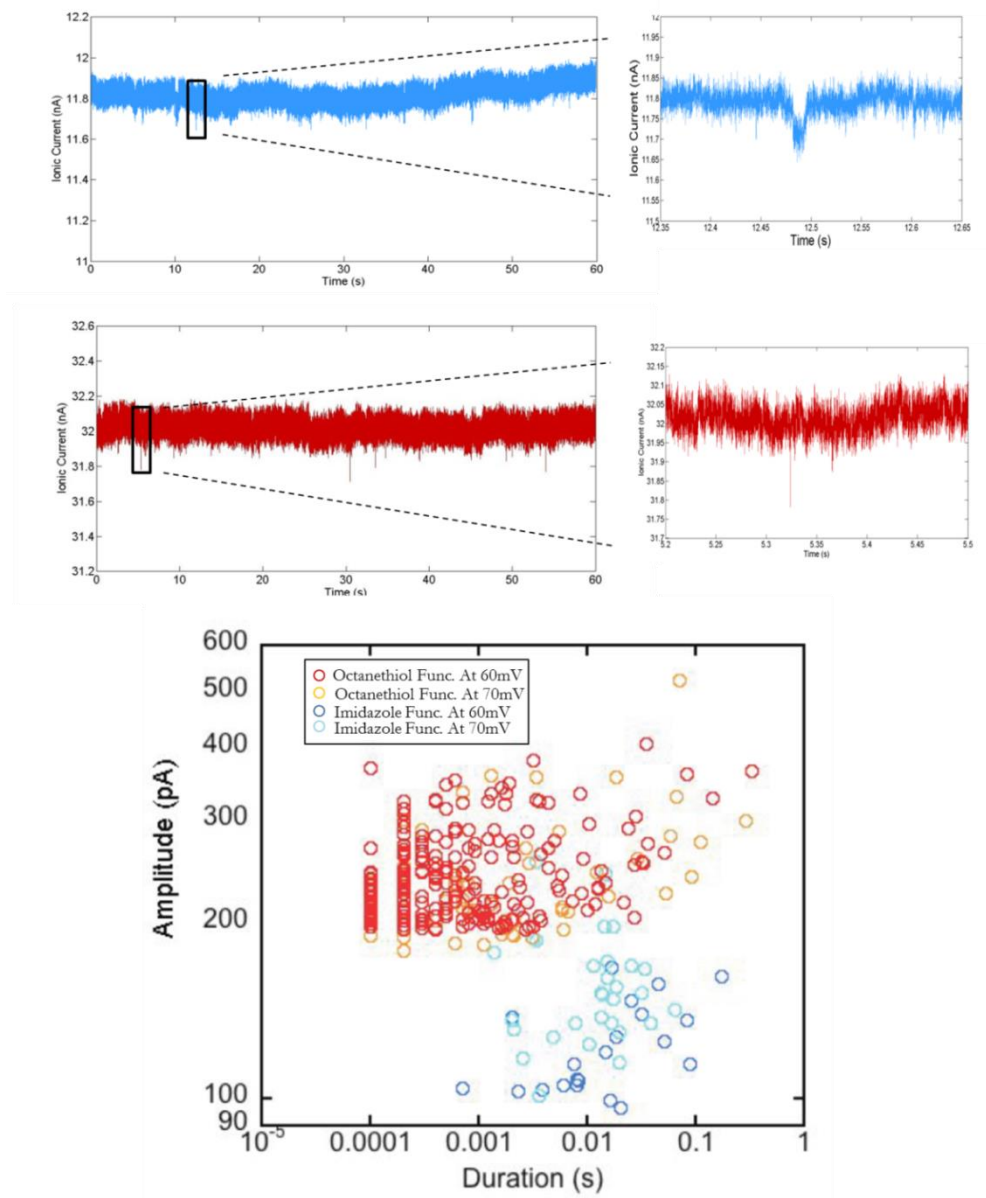
Figure 4.12 *(top) Blue current trace from Imidazole functionalized nanopore and red current trace from Octanethiol functionalized nanopore.(below) Log-log scatter plot of blockade amplitude vs. translocation time for octane-thiol functionalization (red, orange) and imidazole functionalization (cyan-blue).*

4.5.3 Models for slowing Translocation

When DNA molecule translocates through a functionalized nanopore, the molecule seems to be under the competing effects of electrophoretic force pushing towards the positive electrode versus hydrodynamic drag generated by the electro osmotic ion current (which is directed opposite to DNA motion). In addition to this the functionalization causes hydrogen bond interactions that effect a frictional drag on the molecule. If such is the case, then it becomes very interesting to compare the translocation behavior with studies that describe the dissociation of hydrogen bonded complexes.

One of the routes to getting information about the lifetime of hydrogen bonded complexes, is to study the dynamics of dissociation of these using dynamic force spectroscopy (DFS) technique. DFS experiments involve pulling of bonded molecular complexes apart with an atomic force microscope (AFM) and extrapolating data to zero applied force to discover the intrinsic dissociation rate. The binding partners of interest are attached to the AFM tip and a surface via well-characterized linkers (such as PEG tethers) and the probe displacement can be controlled with nanometer precision. The force acting on the tip is measured as a function of the distance while the tip is cycled up and down relative to the surface. Retracting the probe with constant speed increases the force acting on the chemical bond between the two binding partners until the molecules dissociate. The distribution of the rupture forces is measured for various speeds of retraction and quantitative information about the energy-landscape parameters and kinetic constants of the interaction can be obtained from these experiments.

The theoretical modeling of single-bond rupture in DFS is well established In brief, the rupture of a bond that is subjected to a time-dependent force, F(t) or F(s(t)), is a one-step rate process with the force-dependent dissociation rate k(f). The exact functional dependence of k(f) on force f is determined by the underlying reaction potential, U(x), where x denotes the reaction coordinate. Many models describing this dependence have been developed. The Kramer's theory of transition states gives a basic description of the response of molecular systems to the application of force [S. M. Lindsay, Introduction to Nanoscience, Oxford University Press, 2009] The energy landscape for binding and unbinding of a complex is shown in the figure below.
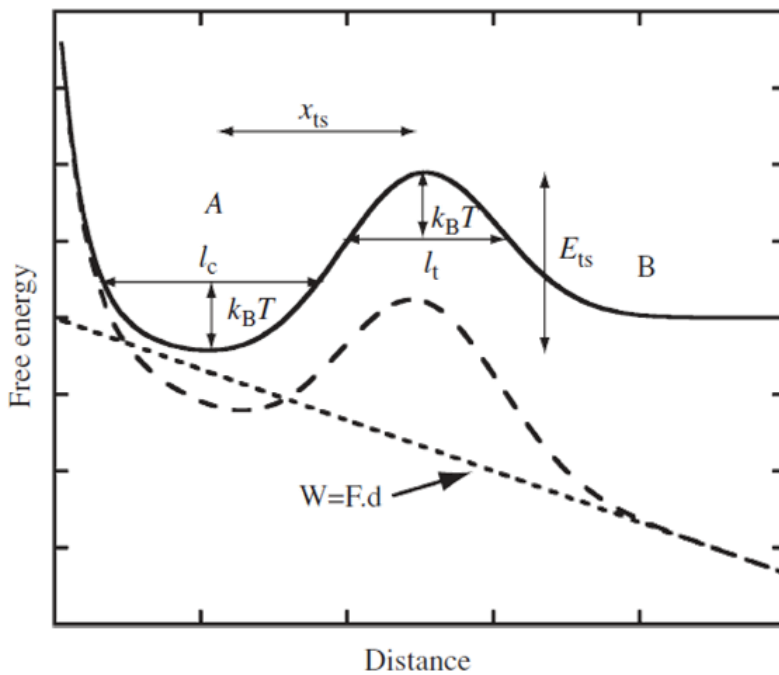
Figure 4.13 *The energy landscape for a transition from bound to unbound state. Work done on the system lowers the energy barrier increasing the dissociation rate.*

The solid line curve represents the energy landscape for a transition from bound state A to unbound state B separated by an energy barrier E_{TS}. The reaction proceeds along the reaction coordinate where the transition state is the maximum in potential at a distance x_{TS} from the minimum of the bound state. When a force F is applied to this system, the system moves a distance d under this effect and the work done on the system equals F.d. The sum of the work done and the original potential results in a new tilted potential landscape, represented by the dashed line. In the process, the energy of the barrier at the transition state is lowered and the rate of dissociation of bonded species increases. Evan's modification of the Kramer's theory calculates the dissociation constant in terms of the curvature parameters l_C and l_T given by the formula $k = \frac{l_C l_T}{D} e^{\frac{E_B}{T k_B}}$ or $k = k_0 e^{\frac{E_B}{T k_B}}$.

E_B represents the energy barrier, and $k_B T$ at room temperature is 4.1pN nm. D represents the diffusion constant for the Brownian motion of the species in the potential well (can be obtained from Einstein-Smoluchowski equation). The dissociation constant at zero force is represented by k_0.

To gain better insight into the barriers that control the dissociation kinetics of dna base pairs, Fuhrmann et al [Biophysical Journal (102)10, 2381-2390 (2012)] conducted a study of the dissociation kinetics of A-T basepair and its triply hydrogen-bonded analog, 2AA-T using DFS. Similar experiments with 2benzamide-A pair was reported by Huang et al [Nature Nanotechnology 5, 868-873 (2010)]. The values of k_0 and x_{TS} from above mentioned literature are tabulated below.

Combination	$k_0(s^{-1})$	x_{ts} (nm)
2 benzamide+ dA	0.28	0.78
dAA+dT (3 HB)	0.23	0.6
dA+dT (2HB)	0.52	0.7

Table 4.2 *Dissociation parameters from DFS data in literature. k_0 and x_{TS} for*

2benzamide + dA (from Huang et al), dAA +dT and dA + dT (from Fuhrmann et al)

In the context of DNA translocating through functionalized nanopores, if the slowing is
activated, the lifetime of the bonded complex can be predicted from the values obtained
from DFS AFM experiments. The lifetime T of a complex in solution is inversely
proportional to the dissociation constant k. Hence from the equation for $k = k_0 e^{\frac{E_B}{Tk_B}}$ the
equation for T can be obtained as $T = T_0 e^{\frac{-E_B}{Tk_B}}$. Since $E_B = F\, x_{TS}$, equation for T becomes
$T = T_0 e^{\frac{-Fx_{TS}}{Tk_B}}$. From **Table 4.2**, taking mean value of x_{TS} to be 0.7 nm and $T_0 = 1/k_0 =$
3s, $k_B T$ to be 4.2 pN nm and applying that $F = KV$ where K = 0.24 pN/mV (as obtained
from force measurements done on DNA by Dekker group) , $T = 3\, e^{-0.04\, V}$ where V is
the applied voltage in mV. Thus, if the interaction between reader molecules and
translocating DNA lead to activated slowing down, T would depend exponentially on
applied voltage. (Also, substituting for voltage of 60 mV in the above expression, we
would get T = 0.27 s predicting a translocation time of 0.27 s per base.)

Instead of activated translocations, if the interactions are purely frictional, because drag force is proportional to the applied voltage, the translocation time would be inversely proportional to applied voltage V.

4.5.4 Comparison of predicted models with experimental data

In this section, the data from a functionalized nanopore (10nm SiN + 10nm Pd) that was used to translocate ssDNA of varying lengths (23 nt, 63nt and 180 nt) is used to fit to the predicted models from previous section. **Figure 4.14** shows the graphs of data presenting voltage dependence of translocation time.
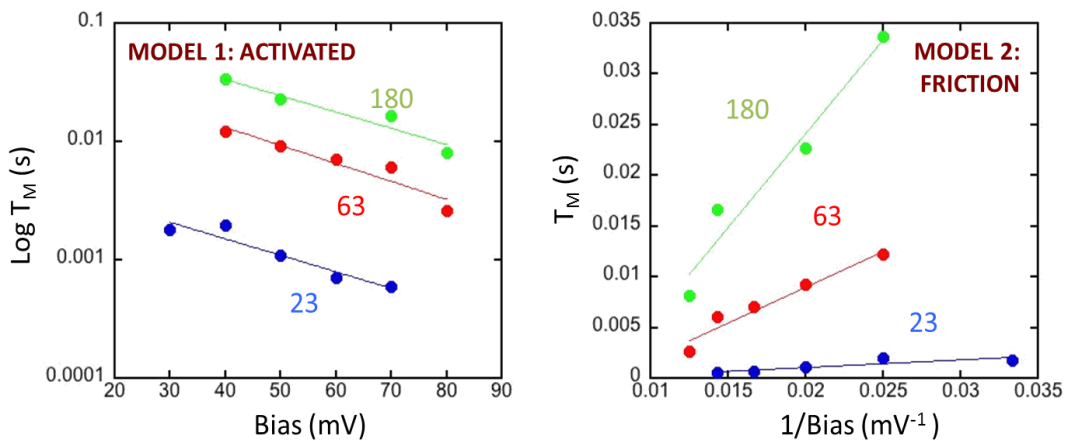
Figure 4.14 *Fits of translocation time as a function of voltage. The graphs include plot of log T vs V on left and T vs 1/V on the right. The former is a fit to the model representing activated translocations while the latter represents frictional slowing model.*

From the plots in Figure 4.14, with the given amount of data, there is a possibility that the data could agree to certain extent with both the models. This may indicate the translocations are a combination of frictional as well as activated interactions. A

comparison of exponents as shown in the table below shows that the exponent matches

closely to the values from DFS data obtained from AFM experiments.

Length	T_0 (ms)	T/base (ms)	kx_{ts}/k_BT (mV^{-1})
23	5.5	0.24	-0.032
63	54	0.86	-0.035
180	120	0.67	-0.032

Table 4.3 *Comparison of exponents. The values of exponents match with those predicted*

by the DFS –AFM data.

The plot in **Figure 4.15** shows the scaling of translocation time with chain length of

translocating DNA. The inset table also indicates the decrease in translocation time with

increase in applied bias.
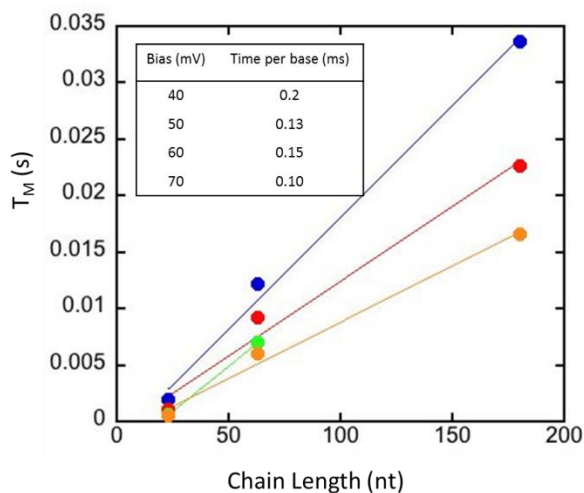
Figure 4.15 *Translocation time as a function of chain length for different voltages.*

102

The scaling of the event duration with molecular length is evident. However the exact dependence of translocation as a function of number of bases is not very clear. This may be due to several reasons such as nonuniform interaction of different regions of ssDNA with the Imidazole reader. While the above results definitely indicate that the current blocakdes are indicative of actual translocation of DNA molecules, further understanding of the mechanism can obtained by perhaps increasing the range of molecular lengths. **Figure 4.16** shows the plot of number of events vs applied bias for 2 different cases. On the left is the case of experiment where the same nanopore was studied under three different surface conditions (functionalized Pd, bare Pd and bare SiN). It is interesting to note that the presence of metal lowers the capture rate of DNA molecules. The plot on right shows the capture rate data for the chip that was used to study molecules of various lengths. The capture rate is found to be independent of the chain length for this range of molecular lengths.
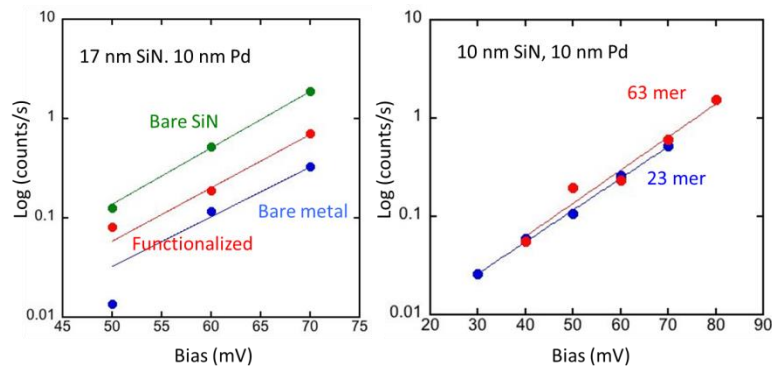
Figure 4.16 *Capture rate change with surface change (left) and molecular length (right).Capture rate is lowered in the presence of metal. For the molecular length range in this study, capture rate is independent of chain length.*

103

4.6 Theoretical Calculations

The motion of DNA or any other charged polymer in the nanopore is complex since the actual force on the DNA has contributions besides the electrophoretic attraction of the DNA to the positively polarized electrode. Specifically, the forces on the DNA can include the drag force, which depends on the size and speed of the molecule; the electrophoretic force, proportional to the DNA charge in the pore, which, to first approximation, depends only on the voltage along the pore and random thermal forces.

All of these contributions have been considered in a finite element analysis of DNA translocation in the floating Palladium electrode device. The calculations have been performed by Dr. Predrag Krstic of Oak Ridge national Laboratory. The simulations are based on the continuum approximation, assuming the micro-nano fluid system in a steady flaw, with small Knudsen and Reynolds numbers, incompressible Newtonian fluid with the usual conservation laws of mass, energy, momentum. This is described by the set of the time-independent partial differential equations which are solved numerically, self consistently, seeking fulfillment of all conservation laws with high accuracy (3-4 significant digits), and full convergence at a fine finite elements numerical mesh, using the multiphysics and modeling software package COMSOL [COMSOL Multiphysics Quick Start and Quick Reference, COMSOL AB. http://www.comsol.com.]. At each iteration, a sparse matrix form is constructed from the finite element discretization of equations (1-4). The algorithm employed (MUltifrontal Massively Parallel sparse direct Solver, MUMPS [http://graal.ens- lyon.fr/MUMPS/]) repeats the damping-factor reduction until the relative error is less than in the previous iteration or until the damping

factor underflows its predefined minimum. The relative tolerance in all present calculations was set to be below 10^{-6}.

To find the steady state fluid flow we numerically solve a set of time-independent coupled, nonlinear partial differential equations, the Poisson-Nernst-Planck-Stokes (PNPS) equations [B.J. Kirby, Micro- and Nanoscale Fluid Mechanics. Cambridge University Press: New York: 2010]. The Poisson equation defines electrostatic scalar potential ϕ as response to the local excess electric charge, $\rho_e = (c_+ - c_-)$ F in the environment of relative dielectric constant ε_r, where $c_\pm$ are the instantaneous volume densities of the positive (+) and negative (-) ions, and F is the Faraday constant.

$$\nabla \cdot \left(\varepsilon_r \nabla \phi \right) = -\frac{\rho_e}{\varepsilon_0}, \quad \rho_e = \left(c_+ - c_- \right) F \qquad (1)$$

This equation in its integral version describes the total electric field flux through a surface enclosing an excess charge. The Nernst-Planck equation, in its integral form, defines the conservation of the flux, $\vec{\Gamma}_\pm$, of charged particles (of charge z($_\pm$e), where e is an elementary charge) through an arbitrary closed surface, i.e. the conservation of the total electric current, and contains electrophoretic (proportional to the ion mobility $\mu_{m,\pm}$), diffusive (diffusion constant $D_\pm$) and electroosmotic terms (proportional to the velocity of the fluid element $\vec{u}$), and its local form is

$$\nabla \cdot \vec{\Gamma}_\pm = \nabla \cdot \left(-D_\pm \nabla c_\pm + z_\pm \mu_{m,\pm} F c_\pm \nabla \phi + c_\pm \vec{u} \right) = 0 \qquad (2)$$

Finally, the Stokes equation is the approximation of Navier-Stokes equations for a laminar flow with a negligible inertial term,

$$-\nabla p + \eta \nabla^2 \vec{u} = -\rho_e \nabla \phi \qquad (3)$$

and yields the fluid velocities, which depend on the electric potentials, charges, external pressure gradients ∇p and the fluid viscosity η through the assumption of the full hydration of charged particles. Thus, the fluid moves with the charged particles. The conservation of the mass flux, i.e. zero total flux of the fluid exiting any closed surface, compatible with the assumption of the fluid non-compressibility, adds the equation

$$\nabla \cdot \vec{u} = 0 \tag{4}$$

When solved with appropriate boundary conditions, the numerical simulations yield the following results. In Silicon Nitride (SiN) as well as Pd coated SiN case, most of the potential drop is seen to occur at the pore. Within the SiN pore, the radial and normal (z) components are comparable in magnitude. The z component of the field is also observed to linearly increase with applied bias. In the case of Pd coated SiN pore however, the presence of floating Pd electrode has a drastic influence due to its surface charging, in particular in the pore part of its surface (the total charge of the Pd layer stays zero!). The floating Pd electrode acquires positive potential, and its upper surface and the pore surface becomes positively charged, inducing negatively volume charge in the Pd part of the electrode. The SiN part of the electrode carries a positive volume charge which due to the negative surface charge of the SiN part of the pore. It is found that the positive volume charge in the Pd part is smaller than the negative one in the SiN pore, unless the bias is bigger than 0.2 V. Also, it is obvious that a longer Pd pore would cause reaching the balance at smaller bias.

As a consequence of the volume charges, opposite in sign in the Pd and SiN parts of the pore, the volume forces acting to the charge distributions in each part of the pore, causing

the electroosmotic component of the flow. Thus, the SiN-pore flow is in the direction of the electric field, while the Pd one is in opposite direction. The bias when reversal happens is shown in **Figure 4.17**, with the change of sign of the total volume force.
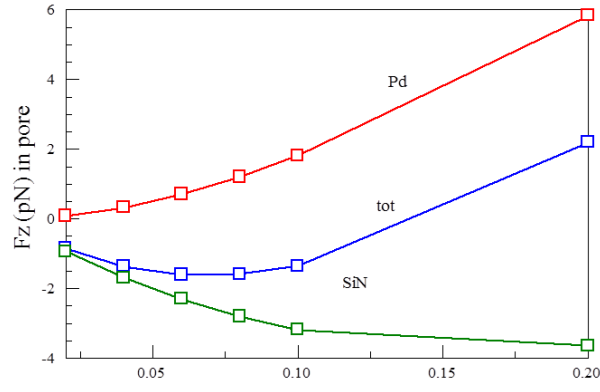
Fig. 4.17 *The volume forces in the combined pore.*

The simulations show that radial forces in the pore are positive, i.e. have tendency to confine the fluid flow to the walls. This force increases with the bias for the Pd part of the pore. The effect of these forces to the fluid flow in the two types of the pore is shown in Fig. 4.18. The magnitude of the fluid velocity in SiN pore increases with bias and is downward, however for the combined pore the fluid velocity is significantly smaller, and changes sign (upward) for bias larger than about 0.2V.
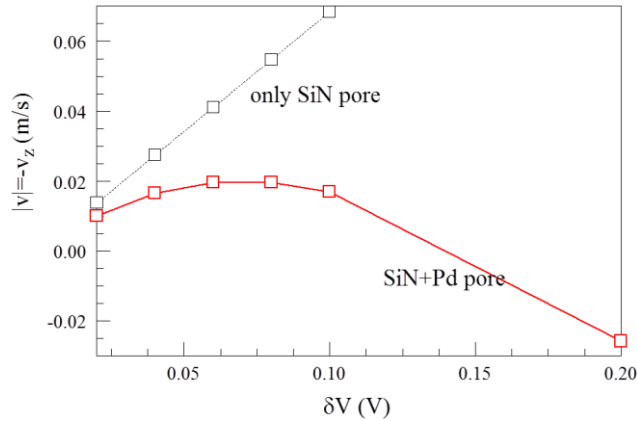
Fig. 4.18 *Fluid velocity in Silicon Nitride and Palladium coated Silicon Nitride pores.*

107

As per theoretical calculations, the total ion current for the cases of SiN electrode (diameter 3 nm, length 30 nm) and SiN+Pd electrode (diameter 3 nm) length 30+10 nm are 3.28 nS and 2.55 nS respectively. I-V measurements on 30 nm long SiN (3 nm diameter) pore yield conductance of 3nS and the conductance measured for the 30 nm SiN+ 10nm Pd (3nm diameter) is 2.92 nS. For both cases, the measured and calculated values are in good agreement within the scope of error arising due to uncertainties in the exact geometrical configuration of the pores that may not be possible to take into account in theoretical models. It must be noted here that thinner pores in 10nm Pd+ 18nm SiN and 10nm Pd + 10nm SiN configuration have been used in experiments. For these configurations, due to the extreme thinness of the membranes, the experimental values of conductance is found to be higher than predicted values of conductance. This could be possibly due to leakage path and migration of charge occurring at such low values of membrane thickness. However such nanopores continue to show linear I-V behavior and are able to capture translocation spikes.

4.7 CONCLUSIONS & DISCUSSIONS

From experiments conducted with fuctionalized nanopores it is evident that, the Hydrogen bonding moieties formed by Imidazole with the ssDNA cause an increase in molecule-pore interactions bringing about slower and more controlled translocations. The slowing down of DNA translocations is advantageous in the nanopore configuration. From the point of view of sequencing and molecular analysis however, functionalization of nanopore can be better utilized by combing electronic measurement of translocating molecules. This can also allow for conducting measurements on thicker membranes with

longer strands of DNA. Longer reads offer better prospects in terms of sequencing device efficiency. Also, as the sensing route for analysis will be primarily via electronic tunneling rather than ionic current measurements, there is better scope of obtaining base recognition and information at the individual nucleotide level.

Also, in order to better investigate the mechanism of slowing down, future experiments may be planned with modified microfluidic set up that allows for collection of larger amount of data per experiment for improving the scope of statistical analysis on the data.

4.8 REFERENCES

1. Livesay, W. R. & Fritz, R. B. Electron image projection systems for microcircuit lithography. *IEEE Transactions on Electron Devices* **19,** 647–651 (1972).

2. *Nanopores: Sensing and Fundamental Biological Interactions.* (Springer, 2011).

3. Lo, C. J., Aref, T. & Bezryadin, A. Fabrication of symmetric sub-5 nm nanopores using focused ion and electron beams. *Nanotechnology* **17,** 3264 (2006).

4. Wu, S., Park, S. R. & Ling, X. S. Lithography-Free Formation of Nanopores in Plastic Membranes Using Laser Heating. *Nano Lett.* **6,** 2571–2576 (2006).

5. Yu, M., Kim, H. & Blick, R. H. Laser drilling of nano-pores in sandwiched thin glass membranes. *Optics Express* **12**, 10044-10049 (2009)

6. Storm, A. J., Chen, J. H., Ling, X. S., Zandbergen, H. W. & Dekker, C. Fabrication of solid-state nanopores with single-nanometre precision. *Nat Mater* **2,** 537–540 (2003).

7. Schenkel, T., Radmilovic, V., Stach, E. A., Park, S. J. & Persaud, A. Formation of a few nanometer wide holes in membranes with a dual beam focused ion beam system. *Journal of Vacuum Science Technology B: Microelectronics and Nanometer Structures* **21,** 2720–2723 (2003).

8. Fitch, J. T., Bjorkman, C. H., Lucovsky, G., Pollak, F. H. & Yin, X. Intrinsic stress and stress gradients at the SiO2/Si interface in structures prepared by thermal oxidation of Si and subjected to rapid thermal annealing. *Journal of Vacuum Science Technology B: Microelectronics and Nanometer Structures* **7,** 775–781 (1989).

9. Li, J. *et al.* Ion-beam sculpting at nanometre length scales. *Nature* **412,** 166–169 (2001).

10. Harrell, C. C., Siwy, Z. S. & Martin, C. R. Conical Nanopore Membranes: Controlling the Nanopore Shape. *Small* **2,** 194–198 (2006).

11. Siwy, Z., Dobrev, D., Neumann, R., Trautmann, C. & Voss, K. Electro-responsive asymmetric nanopores in polyimide with stable ion-current signal. *Appl Phys A* **76,** 781–785 (2003).

12. Siwy, Z., Heins, E., Harrell, C. C., Kohli, P. & Martin, C. R. Conical-Nanotube Ion-Current Rectifiers: The Role of Surface Charge. *J. Am. Chem. Soc.* **126,** 10850–10851 (2004).

13. Kim, M. J., McNally, B., Murata, K. & Meller, A. Characteristics of solid-state nanometre pores fabricated using a transmission electron microscope. *Nanotechnology* **18,** 205302 (2007).

14. Kim, M. J., Wanunu, M., Bell, D. C. & Meller, A. Rapid Fabrication of Uniformly Sized Nanopores and Nanopore Arrays for Parallel DNA Analysis. *Advanced Materials* **18,** 3149–3153 (2006).

15. Heng, J. B. *et al.* Sizing DNA Using a Nanometer-Diameter Pore. *Biophysical Journal* **87,** 2905–2911 (2004).

16. Smeets, R. M. M. *et al.* Salt Dependence of Ion Transport and DNA Translocation through Solid-State Nanopores. *Nano Lett.* **6,** 89–95 (2006).

17. McDonald, C. *et al.* Fabrication of microfluidic systems in poly(dimethylsiloxane). *Electrophoresis* **21,** 27–40 (2000).

18. Lee, J. N., Park, C. & Whitesides, G. M. Solvent compatibility of poly(dimethylsiloxane)-based microfluidic devices. *Anal. Chem.* **75,** 6544–6554 (2003).

19. Wanunu, M. Nanopores: A journey towards DNA sequencing. *Physics of Life Reviews* **9,** 125–158 (2012).

20. Coulter, W.H. Means for Counting Particles suspended in a fluid. US Patent.

21. Song, L. *et al.* Structure of staphylococcal alpha-hemolysin, a heptameric transmembrane pore. *Science* **274,** 1859–1866 (1996).

22. Butler, T. Z., Pavlenok, M., Derrington, I. M., Niederweis, M. & Gundlach, J. H. Single-molecule DNA detection with an engineered MspA protein nanopore. *PNAS* **105,** 20647–20652 (2008).

23. Wendell, D. *et al.* Translocation of double stranded DNA through membrane adapted phi29 motor protein nanopore. *Nat Nanotechnol* **4,** 765–772 (2009).

24. Wanunu, M. *et al.* Rapid electronic detection of probe-specific microRNAs using thin nanopore sensors. *Nat Nano* **5,** 807–814 (2010).

25. Garaj, S. *et al.* Graphene as a subnanometre trans-electrode membrane. *Nature* **467,** 190–193 (2010).

26. Wanunu, M., Morrison, W., Rabin, Y., Grosberg, A. Y. & Meller, A. Electrostatic focusing of unlabelled DNA into nanoscale pores using a salt gradient. *Nat Nano* **5,** 160–165 (2010).

27. Grosberg, A. Y. & Rabin, Y. DNA capture into a nanopore: Interplay of diffusion and electrohydrodynamics. *The Journal of Chemical Physics* **133,** 165102–165102– 15 (2010).

5. SUMMARY

5.1 CONCLUSIONS

An important goal that we face today, from technological and research point of view is the realization of affordable, accurate DNA sequencing platform. Sequencing via nanofluidics offers a label free, relatively in- expensive route to achieve this. Specifically, in this body of work, two branches of nanofluidic devices were explored - Carbon Nanotube based devices and the solid state nanopore based devices. Carbon nanotubes possess novel properties such as large aspect ratio, uniform thickness, frictionless interior and easy wettability that makes them suitable for nanofluidic DNA sequencing (as already established by translocations in single CNT based devices). However, the difficulty in synthesis of single CNT growth devices, lack of control over the helicity and low yield prompted the development of CNT forest membrane project. The CNT forest membranes have been used to study the transport of DNA and nanoparticles. The chemical functionalization of the CNT is used to affect the transport of macromolecules. These properties indicate that such membranes could be used in tunable filtering applications. However, the goal of DNA sequencing is still far from possible within the CNT paradigm. . Hence, in the second part of this thesis we explore solid state nanopores. Nanopores offer a unique and powerful tool for a variety of single molecule studies. Nanopores , both solid state and biological, are known for their single molecule sensitivity and have already been used for DNA translocation studies over the last decade. They hold the potential to sequence DNA faster and cheaper compared to current industrial standard. It is understood that improvements in spatial and temporal resolution can help improve base resolution. Recently, biological pores have pushed the resolution

113

limits by combining with ion channel proteins to demonstrate proof of principle DNA sequencing. To advance similarly within solid state nanopores, we apply recognition molecule chemistry within nanopore framework. Solid state nanopores, when metallized with Palladium and functionalized by Imidazole molecules show that time resolution is enhanced by several orders of magnitude. The implication of this result is two-fold. Firstly, any solid state nanopore analysis can be improved with metallization and functionalization. Secondly, and perhaps more importantly, the recognition chemistry that could achieve base differentiation in the ST M set up, can also be contribute to the entending the duration of translocation events coming from nanopore. A combination of a functionalized nanopore for threading and straightening out DNA and a functionalized tunnel junction for nucleoside differentiability, could ideally merge the best of both worlds and sequence DNA.

5.2 FUTURE WORK

We have established that translocations in solid state nanopores can be slowed down by means of metallization and functionalization with recognition molecule. The next logical step towards DNA sequencing would be the improvement of base-recognition and differentiation. Since it is changes in the ionic flow inside the nanopore channel that are used to sense presence and translocation of biomolecules, reducing the dimensions of the pore to increase base-resolution is one alternative. The configuration would have to be such that when a ssDNA translocates through the nanopore, the ionic current will continue to detect the movement of the analyte molecule through the pore, while the electronic signals coming from tunneling of each base could be used to provide sequence information.

114

Efforts to create such tunnel junctions are already in place.[1] Currently my colleagues are exploring two possible device configurations to this effect – planar and stacked junctions. Planar junctions are created by cutting a tunnel gap in a palladium nanowire using the scanning tunneling electron microscope (STEM) electron beam. When this gap is treated with analyte solution, recognition signals are evident (**figure 5.1**)
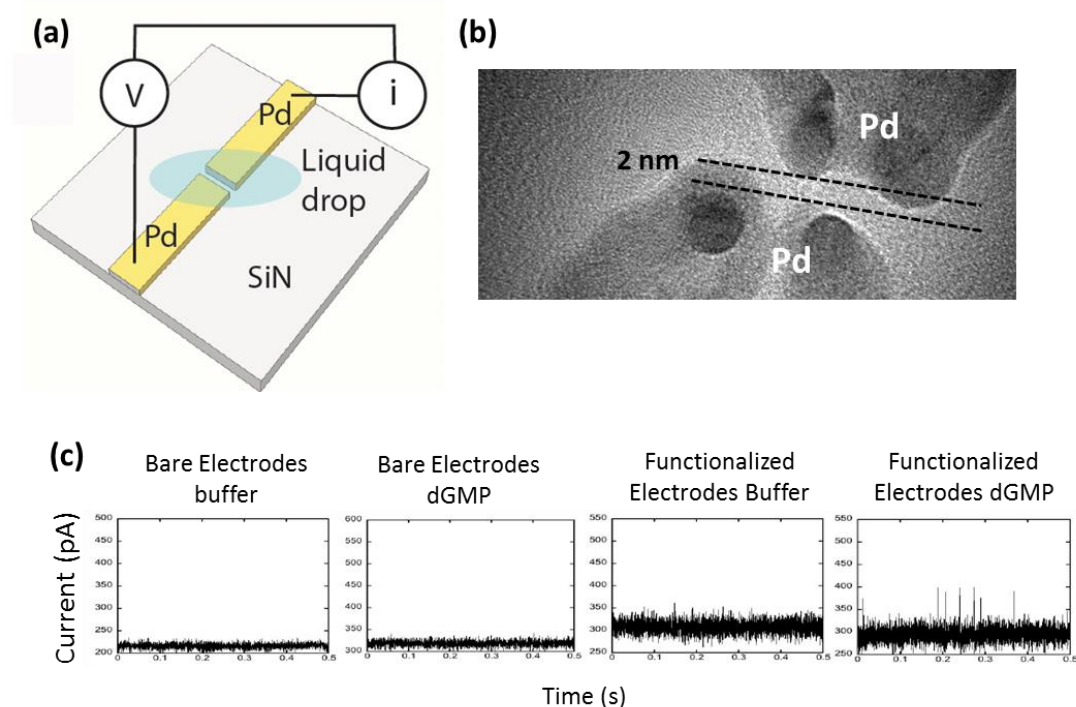
Figure 5.1 *(a) A schematic of a planar junction experiment – tunneling current*

signals are measured while the junction is being exposed to the analyte buffer.

(b) TEM Image of a freshly created 2nm tunnel gap. (c) Current measurements

and controls for various conditions indicating that tunneling signals appear

when dGMP is added to an Imidazole functionalized junction

Stacked junctions are made by fabricating a Pd (10nm)/Al$_2$O$_3$ (3nm) / Pd (10nm) trilayer.

A trench is cut through the trilayer using focused ion beam (FIB) for providing access to

the analyte buffer. Recognition signals are observed when the functionalized junction is

exposed to analyte (**Figure 5.2**)
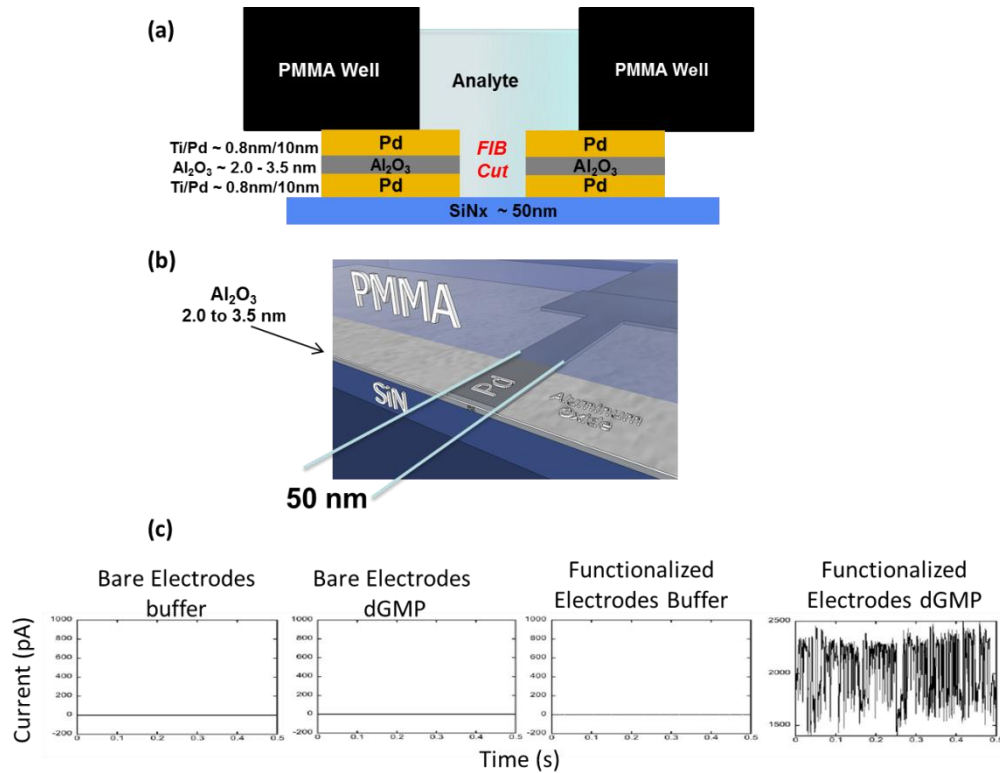
Figure 5.2 *(a) A schematic of the top view of a stacked junction exposed to the analyte*

buffer (b) Schematic of its side view. (c) Current measurements and controls for various

conditions indicating that tunneling signals appear when dGMP is added to an

Imidazole functionalized junction

The promising results from Palladium functionalized nanopores (chapter 4) and tunnel junctions (above) indicate that an integration of the two techniques is definitely a promising path to pursue. Thus tunnel junction incorporated nanopores could be the key to achieving DNA sequencing within the solid state nanopore framework, thus making a leap towards the $1000 genome goal.

5.3 REFERENCES

1. Pang, P., Gyarfas, B., Yang, J., Eller, B. S., Nemanich, R. and Lindsay, S. Solid State Tunnel Junctions for Recognition Tunnelling. Poster presented at the *National Human Genome Research Institute* conference (2013)

APPENDIX A

CO-AUTHOR APPROVAL

I verify that the following co-authors have approved of my use of our publication

"Mass transport through vertically aligned large diameter MWCNTs embedded in parylene"
Nanotechnology volume 23(2012)

in my dissertation

Stuart Lindsay (Arizona State University), Jin He (Florida International University)

Tao Luo (ASU.), Spence Staples (ASU), Purushottam B. Tiwari (FIU)

I also verify that the following co-acuthors have approved of my use of parts of our manuscripts

for publications(in near future)

Stuart Lindsay (ASU), Jin He (FIU), Peiming Zhang(ASU), Brett Gyarfas (ASU)

Predrag Krjstic (Oak Ridge National Laboratory), Sergei Smirnov(NMSU)

Ivan Vlassiouk (Oak ridge National Laboratory), Purushottam B. Tiwari (FIU)

Y. Darici (FIU), Y. P. Shan(FIU), W. Z. Li(FIU), X. W. Wang (FIU)

H. D. Wang (Chinese Academy of Sciences)

APPENDIX B

SUPPLEMENTAL INFORMATION FOR CHAPTER 2
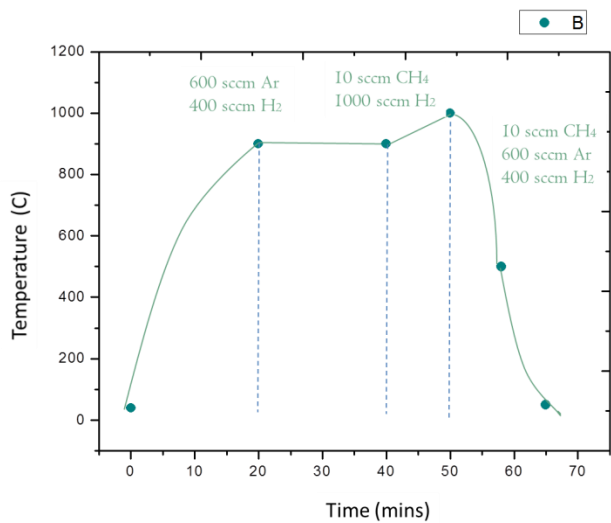
Figure S-1 Protocol for Graphene Growth using Nickel catalyst.
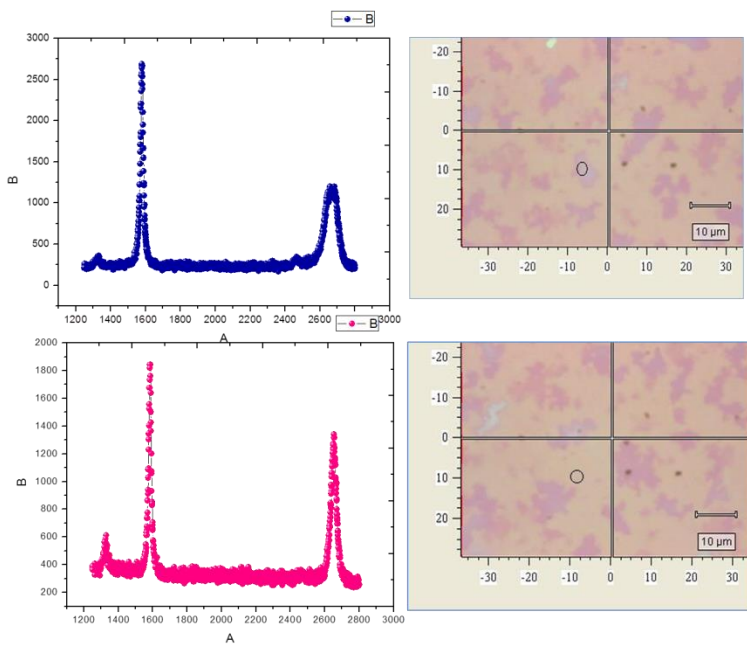
Figure S-2 Raman Spectra indicate the presence of multi-layered graphene

APPENDIX C

SUPPLEMENTAL INFORMATION FOR CHAPTER 4

(a)
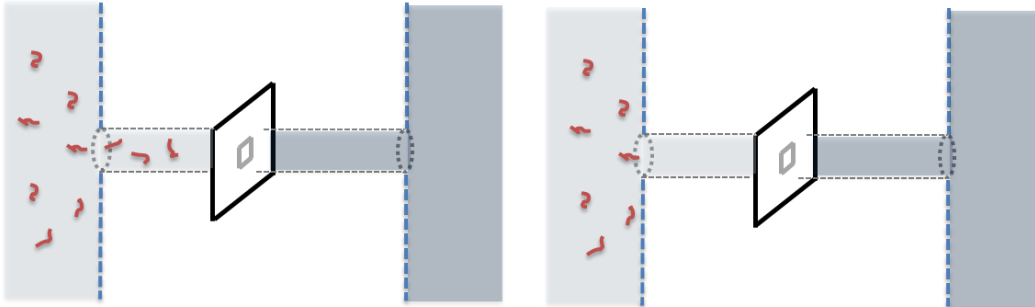
(b)
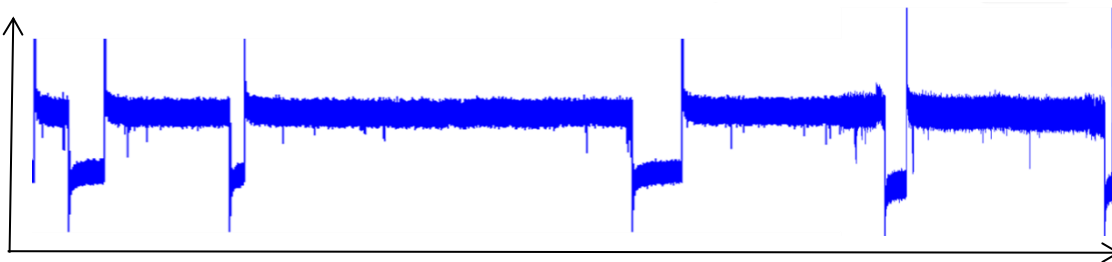
Figure S-3 Methods to control DNA access to the nanopore. One of the issues in the early developmental stage of the nanopore work was the problem of DNA molecules clogging the nanopore. Two steps taken to tackle this issue are described in the figure. (a) The zoom-in on the chip/reservoir area showing DNA being introduced at the vicinity of chip (right), and distance (of 3mm) away from the chip(left). The latter causes the DNA to diffuse towards the region of high electric field leading to more controlled series of events. (b) Time trace of events in a pore, where the voltage is switched off intermittently to prevent accumulation of DNA near the pore entrance

(a)

(b)
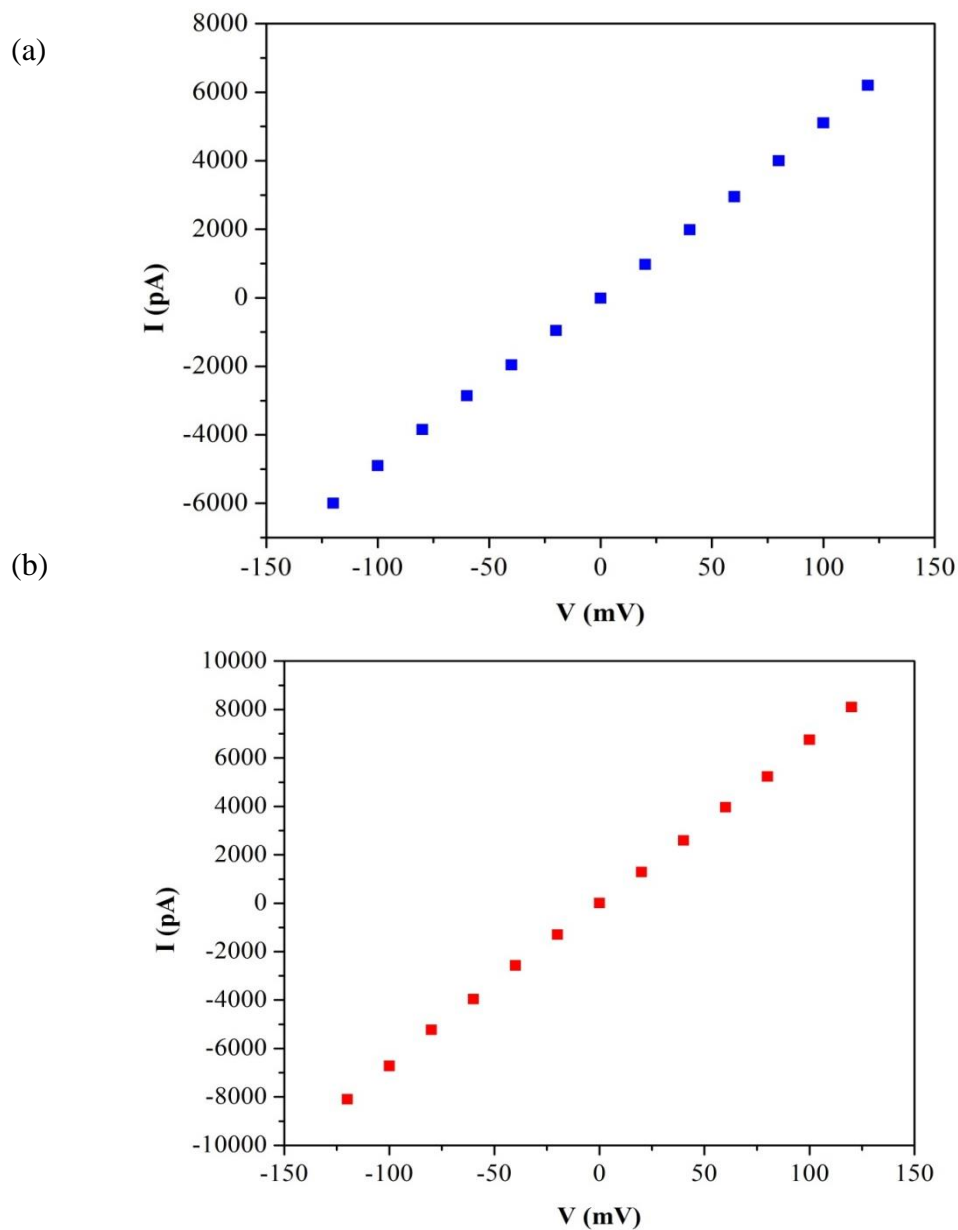
Figure S-4 The Current Voltage curves for a plain Palladium [nanopore (length 20 nm, 10 nm SiN, 10nm Pd/Ti) Diameter =4nm] are shown below. The conductance of the nanopore is observed to increase upon the introduction of DNA in the input reservoir. (a) the conductance before adding DNA is 49.9 nS. (b) After adding DNA it increases to 66.76nS

ANALYSIS CODE

The following MATLAB, developed by Dr. Brett Gyarfas was used for the analysis of data

presented in Chapter 4.

```
gui_Singleton = 1;
gui_State = struct('gui_Name',      mfilename, ...
                   'gui_Singleton',  gui_Singleton, ...
                   'gui_OpeningFcn', @eventDetector_v2_OpeningFcn, ...
                   'gui_OutputFcn',  @eventDetector_v2_OutputFcn, ...
                   'gui_LayoutFcn',  [] , ...
                   'gui_Callback',   []);
if nargin && ischar(varargin{1})
    gui_State.gui_Callback = str2func(varargin{1});
end

if nargout
    [varargout{1:nargout}] = gui_mainfcn(gui_State, varargin{:});
else
    gui_mainfcn(gui_State, varargin{:});
end
function eventDetector_v2_OpeningFcn(hObject, eventdata, handles, varargin)
handles.output = hObject;

guidata(hObject, handles);
initFunc(hObject,eventdata, handles);

function initFunc(hObject,~,handles)
 switch computer
    case 'PCWIN'
        dlldir = fullfile(pwd,'dlls','bin','32-bit','nilibddc.dll');
        headerdir = fullfile(pwd,'dlls','include','32-bit','nilibddc_m.h');
    case 'PCWIN64'
        dlldir = fullfile(pwd,'dlls','bin','64-bit','nilibddc.dll');
        headerdir = fullfile(pwd,'dlls','include','64-bit','nilibddc_m.h');
end

try
    temp = mex.getCompilerConfigurations('C++','Selected');
catch ME
    findError = strcmp(ME.identifier, ...
        'MATLAB:CompilerConfiguration:NoSelectedOptionsFile');

    if ~isempty(findError)
        f = warndlg({'You do not have a compiler selected!',...
            'Please run ''mex -setup'' to select a complier'},...
            'Need to run mex setup!', 'modal');
    else
        f = warndlg({'You do not have a C++ compiler selected!',...
            'Please run ''mex -setup'' to select a complier'},...
            'Need to run mex setup!', 'modal');
    end

    uiwait(f);
    close(hObject)
    return
end

if ~libisloaded('nilibddc')
    try
        loadlibrary(dlldir,headerdir);
    catch %#ok<CTCH>
        warndlg({'Cannot load libraries to read TDMS files!',...
            'You can continue to use the program but it won''t read TDMS files,',...
```

```
                    'you probably need to install a compiler in MATLAB.',...
                    'Google "MATLAB Selecting a Compiler on Windows Platforms"',...
                    'Or Talk to Brett Gyarfas!'},'Error!','modal')
        end
end

parentdirectory=fileparts(which('eventDetector_v2'));
UtilsDirectory=[parentdirectory filesep 'CORE'];
remain = path; temppath = {}; counter = 1;
while true
    [str, remain] = strtok(remain, pathsep);
    if isempty(str)
        break
    elseif ~isempty(strfind(str, 'eventDetector_v2'))
        temppath{counter} = str;
        counter = counter + 1;
    end
end

if ~isempty(temppath), rmpath(temppath{:}); end

addpath(genpath(UtilsDirectory));

[X, ~] = imread(fullfile(UtilsDirectory, 'View', 'Icons', 'xAxisZoomOut.bmp'));
set(handles.btn_xaxis_zoom_out, 'CData', X);

[X, ~] = imread(fullfile(UtilsDirectory, 'View', 'Icons', 'xAxisZoomIn.bmp'));
set(handles.btn_xaxis_zoom_in, 'CData', X);

[X, ~] = imread(fullfile(UtilsDirectory, 'View', 'Icons', 'yAxisZoomOut.bmp'));
set(handles.btn_yaxis_zoom_out, 'CData', X);

[X, ~] = imread(fullfile(UtilsDirectory, 'View', 'Icons', 'yAxisZoomIn.bmp'));
set(handles.btn_yaxis_zoom_in, 'CData', X);

[X, ~] = imread(fullfile(UtilsDirectory, 'View', 'Icons', 'yAxisZoomOut.bmp'));
set(handles.btn_yaxis_overview_zoom_out, 'CData', X);

[X, ~] = imread(fullfile(UtilsDirectory, 'View', 'Icons', 'yAxisZoomIn.bmp'));
set(handles.btn_yaxis_overview_zoom_in, 'CData', X);

disableControls(hObject);

handles.dataHandles = containers.Map();
handles.activeData = [];
handles.prevDir = parentdirectory;

set(handles.axesCurrent,'UserData', containers.Map({'Line1','Line2','ClickPt','Cursor1',
'Cursor2'...
    'Cursor1Text', 'Cursor2Text', 'CursorXDeltaText','CursorYDeltaText'},...
    {[],[],[],[],[],[],[],[],[]}),'Units','pixels','DrawMode', 'Fast');

set(handles.axesOverview, 'UserData',
containers.Map({'Line1','Line2'},{[],[]}),'Units','pixels');

MouseMotionHandler(hObject, {@changePointer, 'arrow'});
MouseMotionHandler.put(hObject, handles.axesCurrent, @zHAxesCurrentMouseMotion);
MouseMotionHandler.put(hObject, handles.axesOverview, @zHAxesOverviewMouseMotion);
MouseMotionHandler.put(hObject, handles.sldr_yAxis_Cur, @HAxesCurrentMouseMotionDefault);
MouseMotionHandler.put(hObject, handles.sldr_xAxis_Cur, @HAxesCurrentMouseMotionDefault);
MouseMotionHandler.put(hObject, handles.sldr_yAxis_Overview, @HAxesOverviewMouseMotionDefault);

set(handles.axesCurrent, 'ButtonDownFcn', @zHAxesCurrentMouseButtonDown);
set(handles.axesOverview, 'ButtonDownFcn', @zHAxesOverviewMouseButtonDown);

set(hObject, 'renderer', 'opengl')
 guidata(hObject,handles);
function varargout = eventDetector_v2_OutputFcn(hObject, eventdata, handles)
```

126

```matlab
if ishandle(hObject)
    varargout{1} = handles.output;
end

function disableControls(hObject)
    children = get(hObject,'Children');
    for i=1:length(children)
        if ~strcmp(get(children(i),'Tag'),'btn_open_file') && ...
                strcmp(get(children(i),'Type'),'uicontrol')
            set(children(i),'Enable', 'off')
        end
    end

function enableControls(hObject)
    children = get(hObject,'Children');
    for i=1:length(children)
        if ~strcmp(get(children(i),'Tag'),'btn_open_file') && ...
                strcmp(get(children(i),'Type'),'uicontrol')
            set(children(i),'Enable', 'on')
        end
    end
    % ----------------------------------------------------------------
function uimenu_File_Callback(hObject, eventdata, handles)
function uimenu_exit_Callback(hObject, eventdata, handles)
% --- Executes on selection change in lstbox_open_files.
function lstbox_open_files_Callback(hObject, eventdata, handles)
tempLstBoxStr = cellstr(get(hObject,'String'));
 if ne(handles.dataHandles(tempLstBoxStr{get(hObject,'Value')}), handles.activeData)

    handles.activeData.Visible('off')

    handles.activeData = handles.dataHandles(tempLstBoxStr{get(hObject,'Value')});
    %Bring the current one forward
    handles.activeData.Visible('on')

    set(handles.godFigure, 'name', ['eventDetector_v2: ' ...
        handles.activeData.pathname '\' handles.activeData.filename]);

end
 guidata(hObject,handles)

function btn_open_file_Callback(hObject, eventdata, handles)
 [filename,pathname] = uigetfile({'*.tdms;*.abf;*.txt;*.evntd','Valid File Types
(*.tdms,*.abf,*.txt,*.evntd)'},...
    'Open File', handles.prevDir);

if ~isequal(filename,0)
    tempLstBoxStr = get(handles.lstbox_open_files, 'String');

    if ~nnz(strcmp(tempLstBoxStr,filename))
        tempLstBoxStr{length(tempLstBoxStr)+1} = filename;
        set(handles.lstbox_open_files,'String', tempLstBoxStr);
        set(handles.lstbox_open_files,'Value', length(tempLstBoxStr));

        if ~isempty(handles.activeData)
            handles.activeData.Visible('off');
        end

        try
            handles.dataHandles(filename) = traceData(filename,pathname,...
                handles.axesCurrent,handles.axesOverview);
            handles.activeData = handles.dataHandles(filename);
            enableControls(ancestor(hObject,'figure'))
        catch ME
            disp(ME)
            disp(ME.message)
            disp(ME.identifier)
            for i=1:numel(ME.stack)
```

127

```
                disp(ME.stack(i).file)
                disp(ME.stack(i))
            end
%           disp(struct2cell(ME.stack))
        end
        handles.prevDir = pathname;
    else
        %Its already loaded, go the value and load the file
        set(handles.lstbox_open_files,'Value', find(strcmp(tempLstBoxStr,filename)))
        guidata(hObject,handles);
        lstbox_open_files_Callback(handles.lstbox_open_files,eventdata,handles);
    end
end

guidata(hObject,handles)

figure(handles.godFigure)
set(hObject,'Enable', 'off')
drawnow;
set(hObject,'Enable', 'on')

% --- Executes on button press in btn_close_file.
function btn_close_file_Callback(hObject, eventdata, handles)
tempLstBoxStr = get(handles.lstbox_open_files, 'String');
tempLstBoxValue = get(handles.lstbox_open_files,'Value');
if ~isempty(handles.dataHandles)
    handles.activeData.Visible('off')

    delete(handles.dataHandles(tempLstBoxStr{tempLstBoxValue}))
    remove(handles.dataHandles, tempLstBoxStr{tempLstBoxValue});

    if tempLstBoxValue == length(tempLstBoxStr)
        set(handles.lstbox_open_files,'Value', tempLstBoxValue-1)
    end

    tempLstBoxStr(tempLstBoxValue) = [];
    set(handles.lstbox_open_files,'String',tempLstBoxStr)

    if isempty(tempLstBoxStr)
        handles.activeData = [];
        disableControls(handles.godFigure);
    else
        tempLstBoxStr = get(handles.lstbox_open_files, 'String');
        tempLstBoxValue = get(handles.lstbox_open_files,'Value');
        disp(get(handles.lstbox_open_files, 'Value'))
        disp(tempLstBoxStr{tempLstBoxValue})

        handles.activeData = handles.dataHandles(tempLstBoxStr{tempLstBoxValue});
        %Bring the current one forward
        handles.activeData.Visible('on')
    end
end

guidata(hObject,handles)

% ------------------------------------------------------------------
function uimenu_open_file_Callback(hObject, eventdata, handles)
.
function lstbox_open_files_CreateFcn(hObject, eventdata, handles)
.
if ispc && isequal(get(hObject,'BackgroundColor'), get(0,'defaultUicontrolBackgroundColor'))
    set(hObject,'BackgroundColor','white');
end

function godFigure_CloseRequestFcn(hObject, eventdata, handles)
delete(hObject);
function godFigure_WindowButtonUpFcn(hObject, eventdata, handles)
% hObject    handle to godFigure (see GCBO)
```

128

```matlab
if ~isempty(handles.activeData)
    notify(handles.activeData,'MouseUpEvent')
end
function godFigure_KeyPressFcn(hObject, eventdata, handles)

persistent test

if isempty(test)
    test = 0;
end

handles.activeData.keyDown = eventdata.Key;
test = test + 1;
% --- Executes on key release with focus on godFigure and none of its controls.
function godFigure_KeyReleaseFcn(hObject, eventdata, handles)
handles.activeData.keyDown = 'None';
function sldr_xAxis_Cur_Callback(hObject, eventdata, handles)
handles.activeData.xSliderVal = get(hObject,'Value');
figure(handles.godFigure)
set(hObject,'Enable', 'off')
drawnow;
set(hObject,'Enable', 'on')

function sldr_xAxis_Cur_CreateFcn(hObject, eventdata, handles)
if isequal(get(hObject,'BackgroundColor'), get(0,'defaultUicontrolBackgroundColor'))
    set(hObject,'BackgroundColor',[.9 .9 .9]);
end
 function btn_xaxis_zoom_out_Callback(hObject, eventdata, handles)
tempLims = handles.activeData.limTime;
deltaLim = abs(tempLims(2)-tempLims(1))/2;
deltaLim = [-1*deltaLim deltaLim];
handles.activeData.limTime = tempLims+deltaLim;
figure(handles.godFigure)
set(hObject,'Enable', 'off')
drawnow;
set(hObject,'Enable', 'on')

% --- Executes on button press in btn_xaxis_zoom_in.
function btn_xaxis_zoom_in_Callback(hObject, eventdata, handles)
deltaLim = abs(tempLims(2)-tempLims(1))/4;
deltaLim = [deltaLim -1*deltaLim];
handles.activeData.limTime = tempLims+deltaLim;
figure(handles.godFigure)
set(hObject,'Enable', 'off')
drawnow;
set(hObject,'Enable', 'on')

% --- Executes on button press in btn_yaxis_zoom_out.
function btn_yaxis_zoom_out_Callback(hObject, eventdata, handles)
deltaLim = abs(tempLims(2)-tempLims(1))/2;
deltaLim = [-1*deltaLim deltaLim];
handles.activeData.limMag = tempLims+deltaLim;
figure(handles.godFigure)
set(hObject,'Enable', 'off')
drawnow;
set(hObject,'Enable', 'on')

% --- Executes on button press in btn_yaxis_zoom_in.
function btn_yaxis_zoom_in_Callback(hObject, eventdata, handles)
tempLims = handles.activeData.limMag;
deltaLim = abs(tempLims(2)-tempLims(1))/4;
deltaLim = [deltaLim -1*deltaLim];
handles.activeData.limMag = tempLims+deltaLim;
figure(handles.godFigure)
set(hObject,'Enable', 'off')
drawnow;
set(hObject,'Enable', 'on')
```

129

```matlab
function sldr_yAxis_Cur_Callback(hObject, eventdata, handles)
handles.activeData.ySliderVal = get(hObject,'Value');
figure(handles.godFigure)
set(hObject,'Enable', 'off')
drawnow;
set(hObject,'Enable', 'on')
function sldr_yAxis_Cur_CreateFcn(hObject, eventdata, handles)
if isequal(get(hObject,'BackgroundColor'), get(0,'defaultUicontrolBackgroundColor'))
    set(hObject,'BackgroundColor',[.9 .9 .9]);
end
 function sldr_yAxis_Overview_Callback(hObject, eventdata, handles)
handles.activeData.HOverview.ySliderVal = get(hObject,'Value');
figure(handles.godFigure)
set(hObject,'Enable', 'off')
drawnow;
set(hObject,'Enable', 'on')
 function sldr_yAxis_Overview_CreateFcn(hObject, eventdata, handles)
if isequal(get(hObject,'BackgroundColor'), get(0,'defaultUicontrolBackgroundColor'))
    set(hObject,'BackgroundColor',[.9 .9 .9]);
end
 function btn_yaxis_overview_zoom_out_Callback(hObject, eventdata, handles)
deltaLim = abs(tempLims(2)-tempLims(1))/2;
deltaLim = [-1*deltaLim deltaLim];
handles.activeData.HOverview.limMag = tempLims+deltaLim;
figure(handles.godFigure)
set(hObject,'Enable', 'off')
drawnow;
set(hObject,'Enable', 'on')


% --- Executes on button press in btn_yaxis_overview_zoom_in.
function btn_yaxis_overview_zoom_in_Callback(
deltaLim = abs(tempLims(2)-tempLims(1))/4;
deltaLim = [deltaLim -1*deltaLim];
handles.activeData.HOverview.limMag = tempLims+deltaLim;
figure(handles.godFigure)
set(hObject,'Enable', 'off')
drawnow;
set(hObject,'Enable', 'on')


% -------------------------------------------------------------------
function uimenu_help_Callback(hObject, eventdata, handles)%#ok<*INUSL,*DEFNU,*INUSD>
parentdirectory=fileparts(which('eventDetector_v2'));
UtilsDirectory=[parentdirectory filesep 'CORE'];

[X, map] = imread(fullfile(UtilsDirectory, 'View', 'Icons', 'brettFace.bmp'));

msgbox({'USAGE NOTES:','-To change the x and y axis on the main plot, you can click and drag just
above the scrollbars on the axis themselves.'...
    '-To change the box representing the currently displayed data, you can click and drag its
borders. To move the box hold shift while clicking the box.',...
    '-You can pan on the main plot by holding shift.',...
    '-To delete an exclusion area, right-click on the area and select ''Delete Exclusion'''},...
    'Tips and Hints','custom',X,map);
function btn_test_Callback(hObject, eventdata, handles)
figure

set(gca, 'FontSize', 26)
% %=================GET RAW DISPLAYED DATA=================%
startPt = round(handles.activeData.displayedTime(1)/handles.activeData.sampleInt)+1;
endPt = round(handles.activeData.displayedTime(end)/handles.activeData.sampleInt);

tY =
(double(handles.activeData.binaryPtr.data.current(startPt:endPt))*handles.activeData.alphaCurrent
)/1000;
plot(0:handles.activeData.sampleInt:(length(tY)-1)*handles.activeData.sampleInt, tY, '-k');

%=========================================================%
```

130

```
xlabel('Seconds')
ylabel('Ionic Current, nA')
traceDataProps = handles.activeData.saveObjStruct();

save('traceDataProps', 'traceDataProps')

zip([handles.activeData.filename '.evntd'], {'traceDataProps.mat', ...
    ['~$' handles.activeData.filename]})

delete('traceDataProps.mat')

movefile([handles.activeData.filename '.evntd.zip'], [handles.activeData.filename '.evntd'])

tEventTiming = handles.activeData.eventTiming;

tInd = regexp(handles.activeData.filename, '.tdms','start');

tFilename = [handles.activeData.filename(1:tInd-1) '_spikeinfo.csv'];

fid = fopen(tFilename, 'w+');

fprintf(fid, '%s\n','Duration,Peak Amplitude,Time Index');

for i=1:size(tEventTiming, 1)
    fprintf(fid,'%.4f,%d,%d\n', (tEventTiming(i,2)-
tEventTiming(i,1))*handles.activeData.sampleInt, ...
        tEventTiming(i,4), tEventTiming(i,1));
end

fclose(fid);




[FileName,PathName,FilterIndex] = uigetfile('*.mat','MultiSelect','on');

eventTimings_all = [];

if iscell(FileName)
    for i=1:numel(FileName)
        load(FileName{i})
        eventTimings_all = [eventTimings_all; [tTraceData.eventTiming(:,1:2).*tTraceData.sampleInt
...
            tTraceData.eventTiming(:,3:4).*tTraceData.alpha]];
    end
else
    eventTimings_all = [tTraceData.eventTiming(:,1:2).*tTraceData.sampleInt ...
            tTraceData.eventTiming(:,3:4).*tTraceData.alpha];
end
```